DIGITAL HOLOGRAPHY FOR EXPLORING INSTABILITIES AND BREAKUP OF LIQUID JETS IN SUPERSONIC CROSSFLOWS

A Dissertation
Presented to
The Academic Faculty

By

Joshua Antonio Johnson

In Partial Fulfillment
of the Requirements for the Degree
Master of Science in the
George W. Woodruff School of Mechanical Engineering
Department of Mechanical Engineering

Georgia Institute of Technology

May 2023

DIGITAL HOLOGRAPHY FOR EXPLORING INSTABILITIES AND BREAKUP OF LIQUID JETS IN SUPERSONIC CROSSFLOWS

Thesis committee:

Dr. Ellen Yi Chen Mazumdar (Chair)
Department of Mechanical Engineering
Georgia Institute of Technology

Dr. Adam Steinberg
Department of Aerospace Engineering
Georgia Institute of Technology

Dr. Suresh Menon
Department of Aerospace Engineering
Georgia Institute of Technology

Dr. Wenting Sun
Department of Aerospace Engineering
Georgia Institute of Technology

Date approved: 4/28/2023

ACKNOWLEDGMENTS

I would like to express prodigious gratitude to my exceptionally patient advisor, Dr. Ellen Mazumdar, who has taught me many theoretical concepts and design techniques and has given direction in my coding efforts. She has also given me valuable personal advice. At times, it may have been a wild goose chase searching for a way to capture and analyze the data, but breaking it down with Dr. Mazumdar helped point me in the right direction. I would also like to thank the research and building engineers of the Ben T. Zinn laboratory – Chris Ballance, David "Seth" Hutchins, David Wu, and Kristopher Manion. They taught me the ropes in how to successfully run the supersonic rig and how to operate the machinery while keeping safety first. Oleksandr "Sasha" Bibik has helped me navigate how to properly use several lasers and light sources while stepping through troubleshooting steps. I would also like to thank the members of my thesis committee – Dr. Suresh Menon, Dr. Adam Steinberg, and Dr. Wenting Sun, for guiding me through this research project and never faltering when I asked questions. I would like to extend my appreciation to both the ME and AE shops. Scott Elliot and Seth Reed have taught me more about manufacturing than I could have ever learned on my own - from how to correctly tolerance parts on CAD to techniques to make complex parts. Even when we ran into issues, we worked together to find solutions and create new designs. In the AE shop, I worked extensively with Greg Rogerson and Henry "Red" Russell near the beginning of my experimental journey. In fact, I went back and forth carrying new designs of the injector to them until a perfect injector design was sculpted. They both showed me how to use different machines, such as the water jet cutter, in order to create the parts I needed. I greatly appreciate the time and dedication both shops showed to accelerate my project forward.

The realm of research was completely new to me when I began graduate school, so I would like to further extend my thanks to everyone who has helped me acclimate to the culture and laboratory environment. Andrew Marsh, Gwendolyn Wang, and Andy

Zheng filtered all of their optical knowledge to me while guiding me through some of the new technical aspects of research. Andrew Marsh has been an essential colleague as he took time to visit the Air Force Research Labratory (AFRL) to conduct experiments with me. His knowledge in the field of holography is incredibly vast and I am humbled to have learned from him and his publications. A special thanks to Steven Budzinski, Russell McGarath, Manya Subbaramaiah, Camden Carlson, and Rashi Yadav for helping run the experiments with me, sometimes having to stay until 2AM. The grind persists! The unfaltering collaboration between all my colleagues has left an extremely positive mark on my research.

Last but certainly not least, I could not thank my parents, Sean and Jacqueline Johnson, grandparents, Dorrett and Lister Thompson, Norman Johnson, and ”Nana”, and siblings, Daniel Johnson, Elijah Johnson, Elizabeth Johnson, and Rebecca Johnson enough for the immense emotional and mental guidance throughout my life. They taught me to take risks and weather the storm with resilience. They helped foster my aptitude to learn, which inherently grew my curiosity in the field of engineering. They taught me to become the best person I could be both in and outside of academics. My cousin, Nasir Thompson, has offered me help and has been a figure for me to look up to ever since day one. Also, shoutout to Merle Ambrose as he has held it down since 2009. My girlfriend, Jodie Chen, is a very determined and successful engineer. She has been by my side since undergrad, and her unwavering support for my goals has not deviated since. Much of the time, I run to her with my research ideas. She either nods her head in approval or scrunches up her face (I can't remember which she did more...). She also agrees to run off on adventures with me when I need a little break from school! I am grateful for all who have made a remarkable difference in my life. In this thesis, I present the result of my hard work, dedication, collaboration, and late-night coffee runs.

TABLE OF CONTENTS

LIST OF TABLES

LIST OF FIGURES

SUMMARY

Direct injection studies of liquid jets in supersonic crossflows (JICFs) are critical for understanding combustion in scramjet engines. Exploring these fluid dynamic interactions is not only an important step towards characterizing fundamental liquid breakup properties but also key for improving engine design and increasing efficiency. Current engine designs lack precise injector optimization and, therefore deliver inefficient fuel sprays. To remedy this, previous studies in the literature have examined how supersonic crossflows affect gaseous and liquid jet breakup characteristics using backlit imaging or schlieren techniques. In this work, we aim to study jet instabilities and droplet breakup characteristics in JICFs for the first time using digital in-line holography techniques. Experiments are conducted in a heated Mach 1.71 crossflow with a transitional regime liquid jet (slenderness ratio L/D of 19) with a diameter of 0.5 mm. High-speed and high-resolution digital in-line holography techniques are utilized to spatially resolve the jet breakup characteristics near the injection point. Results show that the front-edge instability wavelength spacing ranges from 68.3 to 104.5 microns, decreasing as the injected liquid pressure increases from 100 to 500 psi. These results show an inverse relationship between these instabilities and the injected pressure. Both windward and leeward droplet velocities and sizes are also measured using digital holography and analyzed to determine trends. Findings show a clear relationship between the liquid jet injection pressure and the velocity profile of the droplets on the windward side of the jet in the streamwise direction. Droplet size distributions showed small droplet diameters ranging from 3.8 to 25 microns. The unique experimental results acquired in this work can be used to understand entrainment effects, improve mathematical multiphase flow breakup models, optimize injector geometry, and refine future scramjet engine designs.

CHAPTER 1

INTRODUCTION AND BACKGROUND

The evolution of supersonic flight technologies has led to the need for a deeper understanding of the physics of fuel injection in combustion chambers at high Mach number conditions. Jet in crossflow (JICF) configurations are commonly used in gas-turbine combustors, supersonic/hypersonic vehicles, and many other military systems. Understanding the unsteady nature of droplet breakup in this regime is important for developing more reliable and efficient engines with concepts that extend into several engineering disciplines [1]. Typically, large-diameter droplets are undesirable for high-efficiency combustion due to slow vaporization rates. The fuel residence time within the combustion chamber, which tends to be short on the order of milliseconds, is also an important factor for achieving stable combustion [2].

Based on these criteria, liquid jets in crossflows are an efficient way to break up fuel streams into small droplets that quickly mix with the high-speed crossflow air. Because of complex interactions between fluid breakup phenomena, boundary layer separation, and shocks, the injected liquid atomizes to a broad distribution of droplet sizes that can drive combustion efficiency [3]. When the upstream supersonic air interacts with the jet, a high shear layer, which occurs at the interface of the fluids, forms recirculation zones on the windward and leeward sides of the jet near the combustion chamber floor [2]. The mixing creates several vortices, namely counter-rotating pairs, horseshoe vortices, and other vortices in the steady wake, which are all three-dimensional flow features that can be observed using traditional optical techniques, highlighted in Figure 1.1. To better understand the flow phenomena, this chapter will discuss the physics that govern the supersonic jet in crossflow regime. This includes a review of existing literature and a discussion of the motivation behind this research. The goal of this work is primarily focused on characterizing the effect of the penetration depth on instability propagation, droplet velocity characterization, and droplet size distributions generated during the JICF process. The overarching goals of this work are to:

1. Develop a facility capable of delivering variable water jet injection pressures and cross-stream conditions, which can be accurately measured.

2. Measure jet penetration depth trends for various injection pressures and compare measurements with existing curve fits from the literature.

3. Implement schlieren, Digital Inline Holography (DIH), and coherent imaging (CI) optical techniques to visualize flow features.

4. Show that DIH can be successfully used within the supersonic JICF regime to fulfill the roles of multiple techniques. Specifically, show that DIH can be used to visualize flow structures, estimate density gradients due to shock waves, characterize instability wavelengths, quantify droplet velocities, and determine droplet diameters at several locations in the flow.

5. Observe and characterize front-edge droplet pinch-off characteristics on the windward side of the jet for the first time in flows from larger diameter injectors.

1.1 Scramjet Applications

Supersonic ramjet engines, or scramjets, utilize the simple jet in crossflow injection method to generate thrust and propulsion for supersonic and hypersonic vehicles. Unlike rocket engines and other air-breathing jet engine designs, scramjets and ramjets lack mechanical rotating parts, making them an efficient and cost-effective way to power vehicles. One conventional design is a converging-diverging nozzle that accelerates the incoming supersonic crossflow air to a fixed design Mach number. When combined with fuel, the mixture combusts, generating the necessary thrust [4]. To visualize the overall design, Figure 1.2

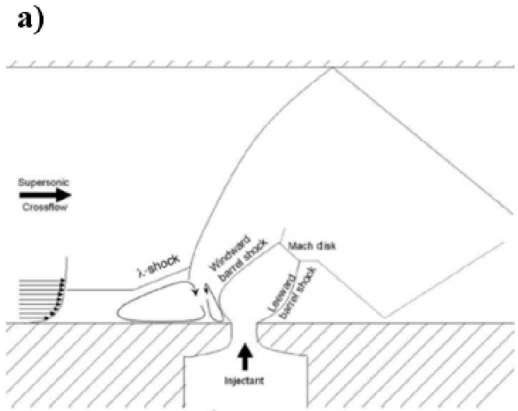

Figure 1.1: Two views of a gas jet in supersonic crossflow (JICF) is illustrated. (a) shows a two-dimensional view of several flow features. (b) portrays a three-dimensional view, showing the vortices and structures of the jet. [2].

shows the geometry of a one-sided divergent scramjet combustor. This particular design was created to induce higher mixing rates and positive flow characteristics [5].

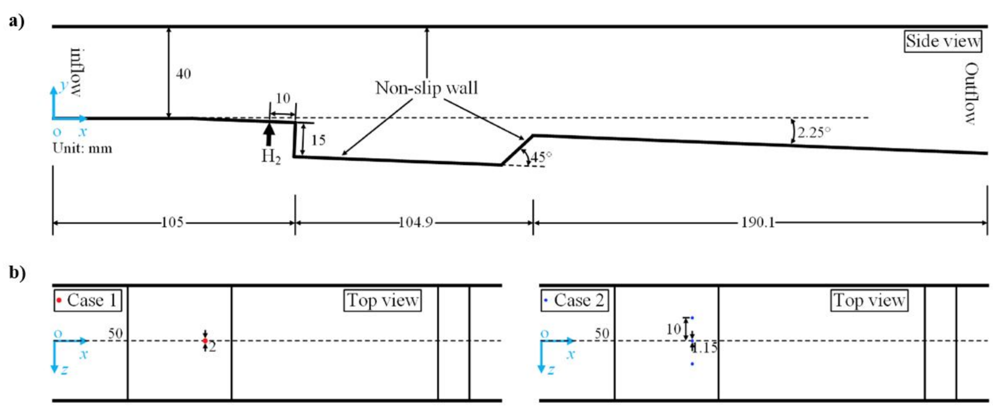

Figure 1.2: Schematic of one-sided divergent scramjet engine is illustrated, showing the different features including a typical wall-normal injector. (a) A side view of the design used for the simulations is presented, showing the divergent angle. (b) Top views of two different cases are shown with different jet injection arrays [5].

Downstream of the nozzle, an injector at a chosen slenderness ratio, L/D, is utilized to inject either gas or liquid into the stream. The flame propagation from this interaction determines the power output of the scramjet engine. However, one of the major challenges that plague this design is the inherent unsteadiness of the jet oscillations due to instabilities, boundary layer effects, and the limited mixing between the fuel and air [6, 7]. Thus, researchers in this field have devised numerous variations of the transverse jet system in an attempt to increase the mixing effect. Design concepts such as the swept ramp injector, cavity-based injectors, and wall-normal injectors have been devised. Aerodynamic ramp injectors, for example, are an array of injectors that tilt at differing degrees, distributed in rows along the streamwise air path. These reduced the mixing effect compared to a traditional baseline 15-degree flush-wall injector and led to a less uniform fuel-air distribution before combustion [8]. Flameholding is, thus, not optimal using swept ramp injectors.

The open cavity flameholder design, on the other hand, increases the mixing effect and reduces drag in the scramjet engine because the majority of the shear layer clings onto the rear edge of the cavity. Cavities can be classified as open (cavity length to diameter ratio $<$ 7 to 10) or closed (cavity length to diameter ratio $<$ 10 to 13). Here, the closed cavity tends to have a higher drag coefficient as the separated shear layer flows into the aft wall [9, 10]. Flame stabilization is enhanced in the open cavity due to lower drag, so it is usually chosen as the preferred method. Moreover, the scramjet net power output is also greatly improved in cavity injectors as compared to other methods [9]. The two cavity methods are illustrated in Figure 1.3.

Finally, wall-normal injection is also commonly used in scramjet designs, as illustrated in Figure 1.1, where the injector is perpendicular to the flow of the crossflow gas. This injector design is well-known for its high mixing rate. Especially in hypersonic applications, the autoignition of the fuel-air mixture from this configuration is particularly attractive. However, it is difficult to sustain combustion and flame holding in this design in steady-state, as illustrated in the OH-PLIF data taken by Ben-Yakar and Hanson [12]. Here, the instabilities formed from the bow and separation shocks interact with the shear layer and greatly enhance the mixing rate in the supersonic regime. These instabilities also have rotational inertia, much like vortex structures.

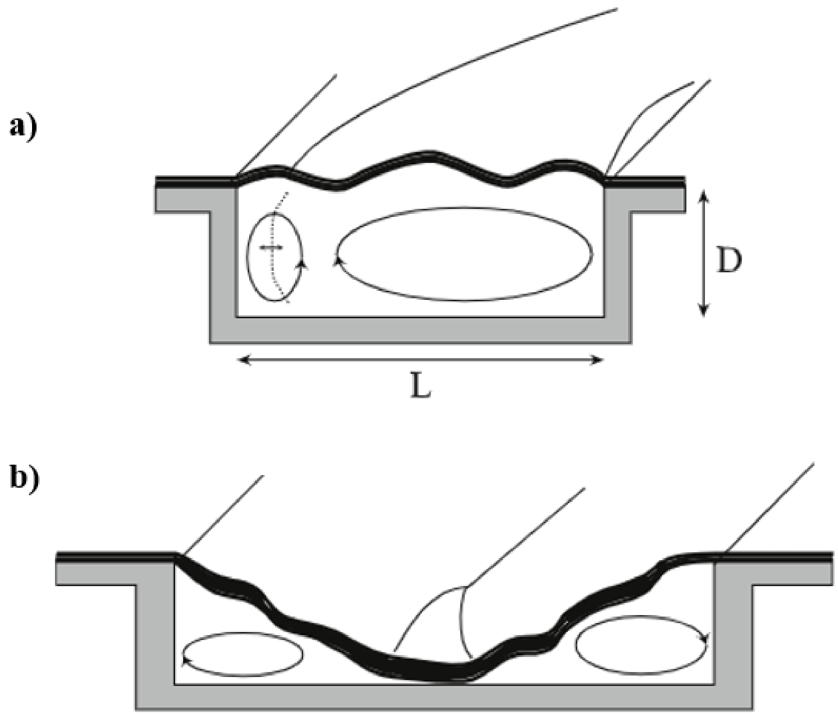

Figure 1.3: (a) Open and (b) closed cavity flow designs for scramjet combustion are shown. Closed cavities have a higher drag coefficient and thus are not often used for practical designs [11].

1.2 Flow Structures in Supersonic JICF

Both fuel atomization and fuel-air mixing are factors that govern the efficiency of an injection spray. The flow structures, such as shocks, instabilities, and ligaments, all contribute to the mixing behavior. Thus, the trajectory of the jet and the subsequent penetration into the crossflow has been extensively studied in experimental and computational domains to develop correlations between these variables. In traditional supersonic JICF, Equation 1.1 has been developed to measure the liquid jet momentum ratio with respect to the gas crossflow [13, 14]. The momentum ratio can be described as,

$$J = \frac{\rho_{liquid} v_{liquid}^2}{\rho_{gas} v_{gas}^2}. \tag{1.1}$$

As the free-steam gas is typically uniform, gas velocity and density will only be a function of the local pressure and temperature. Thus, the momentum value can be readily changed as the liquid injection velocity varies. Consequently, as the jet momentum ratio increases, the penetration depth tends to increase.

Scramjet flame holding, anchoring, and stabilization are closely related to other spray features such as fuel jet penetration depth, which can be readily characterized in non-reacting experiments. Several detailed empirical correlations for jet penetration depth have been made in the literature related to air-breathing engine applications. Depending on the gas temperature and composition, fuel injection conditions, and flow characteristics, different functions have been created to describe the jet penetration including,

1. Logarithmic: $\frac{h}{d} = Aq^{\alpha}(1 + \beta\frac{x}{d})$,
2. Power Law: $\frac{h}{d} = Aq^{\alpha}(\frac{x}{d})^{b}$,
3. Exponential: $\frac{h}{d} = Aq^{\alpha}[1 - exp(\beta\frac{x}{d})][1 + Bexp(\gamma\frac{x}{d})][1 + Cexp(\delta\frac{x}{d})]$.

Different fitting constants have been generated for these functions by Iyogun [15], McDonnel [16], No [17], Ragucci [18], and Stenzler [19] and many others. Note that some literature defines momentum flux ratio as J and some as q. Likewise, some publications refer to penetration depth as h and some as y. In this thesis, h will always refer to the penetration depth, as seen in these correlations above, and y will denote a vertical spatial coordinate in the flow.

In this present study, two main empirical fits were tested to fit the data: one power law fit and one logarithmic fit. Kim [20] has produced a single orifice injector (SOI) curve fit with a heated gas crossflow that builds on the power law. This is described as,

$$\frac{h}{d} = 2.241q^{0.417}(\frac{x}{d})^{0.410}. \tag{1.2}$$

Inamura [21] produced a logarithmic correlation with similar experimental conditions to this current study, which is described as,

$$\frac{h}{d} = (1.18 + 0.24d) * q^{0.36} * ln[1 + (1.56 + 0.48d)\frac{x}{d}]. \tag{1.3}$$

Several instabilities and competing forces also contribute to leading-edge breakup. Kelvin-Helmholtz (K-H, "shear-driven") and Rayleigh-Taylor (R-T, "density-driven") instabilities are present inside the crossflow and contribute to breakup features. K-H instabilities are known to form in environments where fluids of differing velocities shear past each other. R-T instabilities occur when fluids of two densities intermix. Because this work demonstrates a crossflow of air and water, at different velocities and densities, both phenomena are expected to contribute to flow features. A visual representation of how K-H vortex rings tilt and stretch in a typical gas-gas JICF setup is shown in Figure 1.4. In gas-gas flows, the effect of front-edge instability propagation to contra-rotating pairs (CRVP) is a major component leading to an increased mixing rate between the two gases.

In liquid JICF environments, however, this horseshoe structure does not appear to be present. Despite this effect, the three-dimensional waves from the front-edge instabilities are likely to help with liquid mixing and entrainment in the leeward side of the flow. Furthermore, unlike gas-gas jets, surface tension and inertial breakup effects (as described by the Weber number) can contribute to K-H and R-T instabilities, creating shearing ligaments and droplet pinch-off. The capillary Rayleigh-plateau can also contribute to the number of propagated waves on the front-edge [23]. Because water has considerable surface tension, the intensity of the R-T instability will likely decrease as compared to gas-gas injections for small wavelengths [24]. Since multiple instabilities occur simultaneously, it is difficult to attribute flow features to a single source. Nevertheless, unsteady vorticial structures form in these flows, and eventually, the jet expands as droplets break up [25].

For the liquid supersonic JICF environment, previous work has shown some evidence that R-T instabilities are more persistent than K-H instabilities and are responsible for the

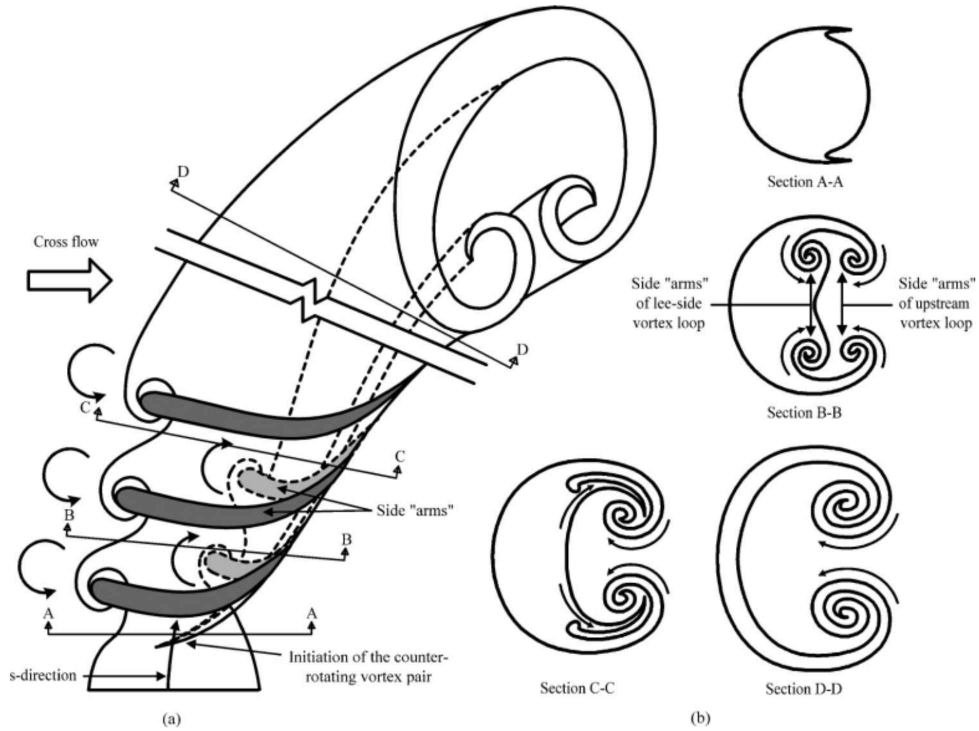

Figure 1.4: This gas jet in a supersonic crossflow diagram shows the contra-rotating vortex pairs (CRVP) formed in part from the front-edge instabilities which wrap around into the vortex. This increases the mixing rate between the crossflow and injector [22].

liquid breakup as the density ratio between the two fluids increases [26]. In fact, a study by Beale shows that when the K-H and R-T instabilities are introduced into a model, both were responsible for turbulent mixing and could successfully predict several flow parameters, like jet penetration, Sauter Mean Diameter (SMD), and jet shape [24] However, high-resolution liquid breakup near the front of the jet has not been previously examined using time-resolved diagnostics. Therefore, the R-T and K-H instabilities as they relate to liquid jet breakup need to be examined in more detail.

Taking a look at Figure 1.1 again, notice some other flow features, such as the separation (lambda) shock, windward bow shock, and recirculation zones, which have implications on breakup in the windward side of the jet. Due to the high-density difference between gas and liquid, the water acts as a physical flow barrier. Therefore, it interrupts the incoming air boundary layer, which leads to it separating and creating a separation shock. Underneath this, a windward recirculation zone forms due to the pressure difference. In a reacting flow, this zone traps products and anchors the flame, so engineers typically attempt to utilize this effect for flame stabilization. Moreover, a three-dimensional bow shock connects to the separation shock and follows the curvature of the jet trajectory. This shock thickens the boundary layer and causes it to separate. It has also been found within literature that this flow feature slightly deviates from a mean spatial location [27]. The shocks and boundary layer separation add to the oscillations and instabilities on the front-edge of the jet. The complex interaction between these features has not been studied extensively in the literature, which motivates new experiments in this area.

1.3 Dynamic Liquid Breakup in Supersonic JICF

As discussed in the previous sections, the boundary layer separation and complex shock systems contribute to the dynamic instabilities on the shear interface between the two fluids. They also contribute to ligament and droplet formation on the front-edge of the liquid plume and within the downstream liquid breakup area. Figure 1.5 shows a schematic of the liquid jet in supersonic crossflow with liquid jet instability growth at the front of the jet and droplet breakup on the leeward side. An important distinction from gas-gas experiments is that there is no droplet formation in a gas jet because there is no surface tension, only a mixture of the two fluids occurs in those environments.

Important parameters that describe droplet formation include the non-dimensional Reynolds number of the jet, Weber number, Ohnesorge number, momentum-flux ratio (J), and penetration depth. In this work, the liquid Reynolds number of the jet as it passes through the injector is defined as,

$$Re_l = \frac{\rho_l V_l D}{\mu_l}, \tag{1.4}$$

where ρ_l is the water density, V_l is the water injection velocity, D is the water jet diameter, and μ_l is the liquid dynamic viscosity. This non-dimensional number helps determine the

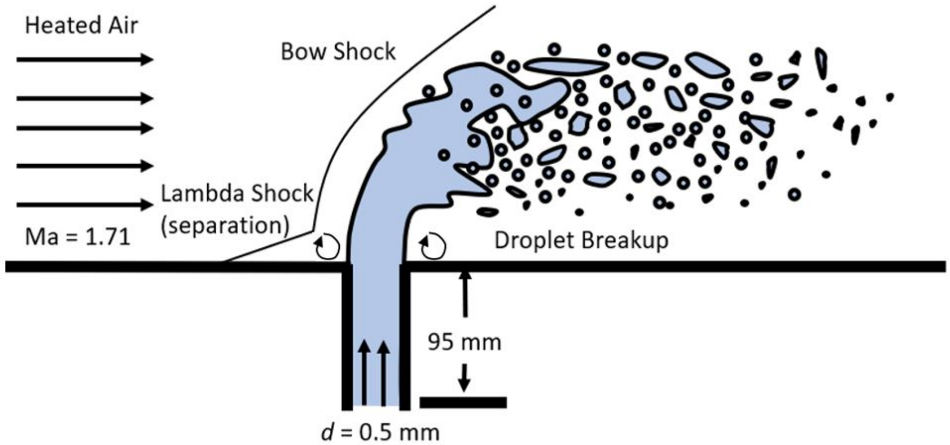

Figure 1.5: A liquid jet in supersonic crossflow is illustrated with flow features. The rotating arrows correspond to recirculation zones that can generate ligaments and droplets and lead to improved flame anchoring closer to the ground of the combustion chamber.

penetration depth and momentum-flux ratio [14]. For example, a laminar jet will penetrate the crossflow less and bend earlier than a transitional or turbulent jet. The Weber number is typically found in multiphase flows and compares the inertial to surface tension effects to determine the droplet breakup morphology. It is calculated using,

$$We = \frac{\rho_g V_g^2 D}{\sigma}, \tag{1.5}$$

where ρ_g is the gas density, V_g is the gas velocity, and σ is the surface tension [28]. Another important related parameter is the Ohnesorge number, defined as,

$$Oh = \frac{\mu_l}{\sqrt{\rho_l \sigma D}}, \tag{1.6}$$

which determines the effect of viscosity on droplet breakup [29, 30]. Another important non-dimensional number that helps determine the influence of R-T instabilities is the density ratio,

$$\rho_l/\rho_g = \frac{\rho_l}{\rho_{g,\infty}}. \tag{1.7}$$

Table 1.1: Water injection testing conditions and calculated parameters for a 0.5 mm jet.

$P_l\,[psi]$	$V_l\,[m/s]$	Re_l	J	ρ_l/ρ_g
100	37.2	182,350	7.3	2152
200	52.6	257,980	14.5	2152
300	64.4	316,070	21.8	2152
400	74.3	365,098	29.0	2152
500	83.1	408,339	36.3	2152

The momentum-flux ratio, as defined earlier, determines the relationship between the water jet injection and air crossflow momentum. If the value is very small, the air crossflow moves with more momentum than the injected liquid [14], which will influence the penetration depth and jet trajectory during break up. Finally, the penetration depth is simply the vertical distance the liquid jet travels relative to the diameter of the jet. This parameter partially determines the amount of liquid-gas interface mixing, as a higher penetration depth enables more gas to interact with the liquid. This can lead to lower droplet densities and higher droplet velocities. These non-dimensional numbers are critical for characterizing the flow as well as comparing results with the literature [31].

In this work, water jet injection pressures between 100 and 500 psi were tested using a 0.5 mm jet. This enabled the visualization of flow behavior for different momentum flux ratios, J. In Table 1.1, the non-dimensional numbers used to describe the fluid motion have been calculated for each of the liquid injection pressures. The Reynolds number for the airflow is $Re_g = 8.42 \times 10^6$, computed at the injection point. The Ohnesorge number for these experiments is $Oh = 5.25 \times 10^{-3}$ (<<0.1), indicating little to no influence from viscosity. The gas Weber number is $We = 1307$, indicating that the inertial forces are high and that the liquid surface tension plays a large role in breakup. It is expected that the edges of the column will shed droplets on the leeward side of the jet.

Values in the table were computed using an Engineering Equation Solver (EES) and water pressure changes were used as an independent variable. To calculate the values, the thermophysical properties of water and air were pulled from the EES library, which is derived from a NASA gas properties library.

These non-dimensional numbers form the foundations for the analysis of liquid breakup in supersonic JICF. Particularly, the water jet velocity, and therefore the Reynolds number, greatly influences the momentum flux ratio. Since the momentum flux ratio is a key factor in penetration depth, this quantity is especially important for quantifying the mixing efficiency and comparing breakup behaviors at different conditions.

1.4 Thesis Overview

In order to study liquid breakup in supersonic JICF in more detail, this thesis aims to provide a novel framework for applying digital inline holography (DIH) to a liquid jet in supersonic crossflow. Outside of a few experiments on aerated jets [32, 33, 34, 35] there has been no application of holography in these supersonic JICF environments. Thus, this work is the first to utilize holography to examine dense liquid jets in JICF. Two regions of the jet are observed using this optical technique: the windward side of the penetrating liquid and the downstream droplets breakup on the leeward side of the jet. While there has been some previous work analyzing jet penetration, droplet velocities, and droplet sizes using schlieren techniques [27], there are currently no experimental observations in the literature of liquid breakup in the recirculation zone at the windward side of the jet. Thus, this work also shows unique flow phenomena that occur in large-diameter jets. Because holography can also be used to measure changes in density gradients, bow shocks can also be observed using this technique, which has not been previously described using DIH in these environments. Thus, schlieren is presented in this work as a confirmation of intermixing, a visual marker for flow dynamics, and a comparison tool to DIH. By quantitatively analyzing the different breakup and flow features in a liquid jet in supersonic JICF, numerical models [36] can be validated. Additionally, using DIH characterization tools, new scramjet injection methods can also be evaluated for future vehicle applications.

In Chapter 2, the design modifications needed to use a supersonic wind tunnel facility [37] for liquid breakup experiments are presented. First, a liquid injection system was designed in order to (a) support pressurized water up to 500 psi with limited pressure drop and (b) ensure a relatively low droplet breakup flow field density. For these reasons, a 0.5 mm diameter injector was designed and modeled on Solidworks. The L/D slenderness ratio of the injection system is 19 and the liquid Reynolds number is turbulent, putting the output profile of the water jet in the transitional regime. A 2.0 mm diameter injector was previously manufactured for this rig and is presented in comparison to the 0.5 mm jet. To deliver pressurized water to these injectors, a piping and instrumentation diagram (P&ID) was developed. In this diagram, several hand valves, safety disks, and regulators are drawn to control the flow of water. Coupled with an updated LabVIEW program, the rig operator can control the water flow remotely from 0 to 500 psi. To physically capture the data at the front-edge and liquid plume, a 532 nm continuous wave laser and pulsed PIV laser are spatially filtered and expanded. The beams pass into the wind tunnel through fused silica glass windows that can withstand the temperatures and pressures of the rig operating at Mach 1.71.

Chapter 3 discusses the optical techniques used to visualize the morphology of the supersonic JICF. With the naked eye, intermixing between fluids cannot be seen, so high-magnification optics are utilized. High magnification schlieren methods are first implemented for capturing bow shock features and jet penetration data. This data is then compared with images captured using high-magnification digital inline holography (DIH) methods. This technique uses two-dimensional imaging sensors to capture three-dimensional flow features. Thus, this method allows the user to adjust the focal plane in post-processing using numerical refocusing MATLAB codes, enabling users to analyze three-dimensional features. Additionally, DIH can be used to analyze density gradients in the flow, which includes the motion of the bow shock. Lastly, coherent imaging is used to capture in-focus images of the jet. This technique uses the same optics as DIH but places the focal point at the centerline of the jet. This produces clear images that do not need to be refocused in post-processing but flattens the line of sight data into a single two-dimensional image. All these techniques are used to examine the flow dynamics at different testing conditions while highlighting how the novel capabilities of DIH can be used for supersonic JICF analysis.

Chapter 4 uses optical techniques to analyze the windward side of the jet. The most important parameters to study in this region are the jet penetration depth and instabilities that form on the liquid jet as the injection pressure changes. Holding the crossflow air pressure and temperature constant, jet penetration depths were measured and compared with correlations developed in the literature. Both schlieren and DIH were used to capture the data at the front-edge and a custom edge-tracing MATLAB was used. To quantify the instability propagation along the jet edge, different tracking codes are used to analyze the wavelength spacing. The growth and spacing between these instabilities are analyzed as a function of the momentum flux ratio (J) and the penetration depth (h).

Chapter 5 examines droplet breakup behaviors on the leeward side of the jet. When the jet is injected against the crossflow, breakup occurs and droplets with varying diameters are formed. The type of breakup depends on non-dimensional parameters, such as the Weber number and Ohsenege number. Since the Ohneserge number is much lower than one, the Weber number dominates the droplet breakup morphology [29, 30]. The goal of this chapter is to track the droplet velocities as a function of physical height and length along the jet. To achieve this, a continuous wave laser is utilized in a coherent imaging setup. Because the droplets are (a) in a single frame for hundreds of nanoseconds and (b) move in and out of the chosen focal plane, the diffraction rings produced by the droplets can be tracked using an ultra-high-speed camera (up to 5 MHz) and multi-frame correlation techniques. Using an instantaneous pulsed laser and high-resolution camera, the diameters of droplets at different spatial locations are also captured. Knowing both the droplet velocities and diameters allows precise characterization of droplet breakup phenomena that have not been previously captured in the literature.

Finally, Chapter 6 ties all the findings of this work together and discusses their application to air-breathing vehicles. The contributions of the work are summarized and future work is identified. The new DIH tools described in this work can potentially be used to expand the analysis capabilities for new injector designs in future vehicles. Additionally, the quantitative flow trends found in this research can be used for model validation and for improving our understanding of liquid breakup phenomena in supersonic JICF.

CHAPTER 2

FACILITY DESIGN AND MODIFICATIONS

In this chapter, the designs and modifications of the JICF facility components are outlined and discussed. The original supersonic windtunnel facility [37] was used to study gas-gas supersonic JICF. Since liquid is being injected in this work, a pressurized water pipeline was designed and built to provide a range of injecting pressures into the crossflow, thereby allowing various momentum flux ratios to be tested. The a new liquid injector was also designed to reduce the density of the liquid breakup droplets. A transitional L/D was adopted for this injector that captures benefits from both turbulent and laminar jets. Next, this chapter describes several test section designs with optical glass for applying imaging diagnostics. The safety factors for selecting window materials and thicknesses are also outlined. Afterward, the flow condition instruments, which measure temperature and pressure measurements in both fluids, are discussed. Then, the LabVIEW VI that was built to remotely control and monitor these instruments is presented. Finally, the thermal expansion of the rig up to 550 K is quantified in order to enable accurate measurements of phenomena that occur in different locations inside the facility.

2.1 Experimental Facility Operation

This research was conducted in one of the four high-pressure labs the Ben T. Zinn (BTZ) combustion laboratory at the Georgia Institute of Technology. The lab houses a high temperature, high pressure compressor system, which can be used to generate a supersonic crossflow. The custom facility used in this work went through several design iterations to convert from a gas jet to a liquid jet system. This section is devoted to outlining the water pipeline, injector, test section, and instrument designs. The parts were designed to be accessible and easy to dismantle and/or replace. The metal components for the facility were manufactured at the Aerospace or Mechanical Engineering machine shops. An overview of the rig with the computer-aided design (CAD) and final facility image are shown in Figure 2.1.

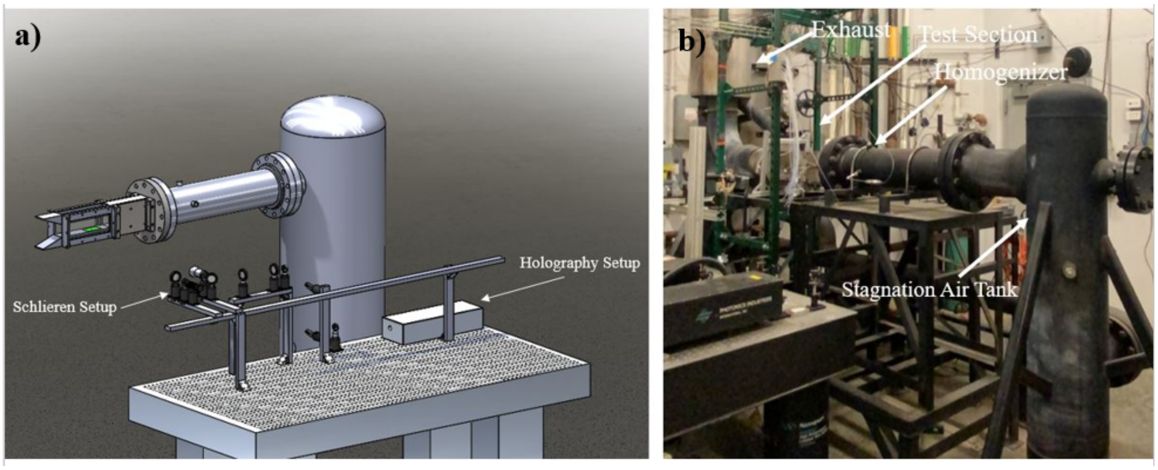

Figure 2.1: (a) A CAD model of the rig and optics as well as (b) an in-lab image are presented.

2.1.1 Air Compressor System

In order to get high-velocity air into the converging-diverging nozzle of the test section, a 3000 psig Norwalk air compressor system compresses the air and diverts it to the rig for operation. The compressor has a 105,000 scf storage capacity and pumps compressed air to a series of storage tanks, as shown in Figure 2.2. The storage tanks have an automatic relief valve that releases any excess moisture. The maximum delivered pressure to each of the high-pressure rooms is 720 psig but the maximum used in these experiments is 200 psig. This corresponds to a stagnation pressure of approximately 34 psi.

There are several systems that allow the compressor to operate efficiently, including the air inlet section, chiller/cooling tower, lubrication oil system, dryer system, exhausts, and electrical network. Figure 2.3 showcases these systems. First, the compressor control unit is used to start the system operation. When started, the compressor inlet pulls in humid ambient air and compresses it through five stages. The lubrication oil system lubricates

Figure 2.2: The 3000 psig Norwalk compressor and accompanying array of air tank reservoirs are displayed. The air from the tanks is distributed into four high-pressure labs in BTZ.

all the moving parts to prevent overheating and wear on the moving parts. In tandem with this, a chiller/cooling tower works as a heat exchanger and passes relatively cool water into the compressor to reduce gas temperatures between stages. The air dryer then removes the humidity from the compressed air and the air is directed to the storage reservoirs. After the air is compressed and humidity reduced, a block valve is opened, allowing pressurized air into the test cell and supersonic JICF rig. An instrument air system controls the exhaust (backdraft) damper, which allows the expulsion of the water/air mixture.

Finally, a Stahl air heater, which operates at a maximum of 995 °F and a mass flow rate of 300 lbm/minute, is utilized to heat the crossflow air to target stagnation temperatures of 550 to 600 K. The target temperature range is chosen to avoid freezing after isentropic expansion and the calculated critical stagnation temperature was determined to be 433 °F. The heater is controlled by the furnace, which provides heat flux to the crossflow air, as shown in Figure 2.4. This is further controlled by a heater control panel in the rig control room. Here, the core burner temperature is constantly regulated to ensure that the process air temperature does not reach more than 1300 °F. It is important to note that there are often

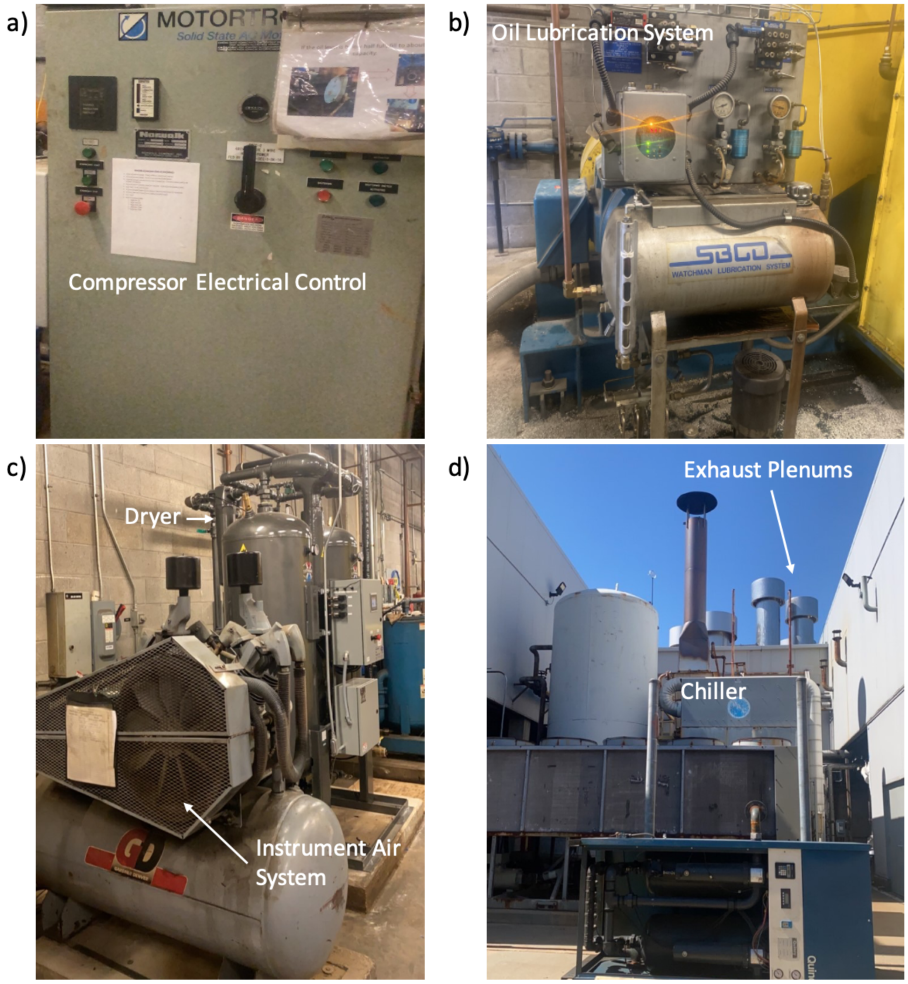

Figure 2.3: The components of the compressor system are shown indicating (a) the compressor electrical control panel, (b) the oil lubrication system, (c) the dryer and instrument air systems, and (d) the chiller and exhaust plenums.

fluctuations in the temperatures and pressures between testing days, as the outside ambient air conditions (temperature and humidity) affect the compressed air storage tanks. The positive displacement of the exhaust system also slightly influences the wind tunnel operating pressure on a day-to-day basis, which can cause variations in test conditions. Overall, however, these variations tend to have only a small effect on measurement repeatability.

Once the heated compressed air enters the high-pressure cell, it enters the supersonic JICF rig, which was originally built by Dan Fries [37]. The high-pressure gas first enters an inlet pipe which is controlled by a hand valve. Then, the flow enters a stagnation tank.

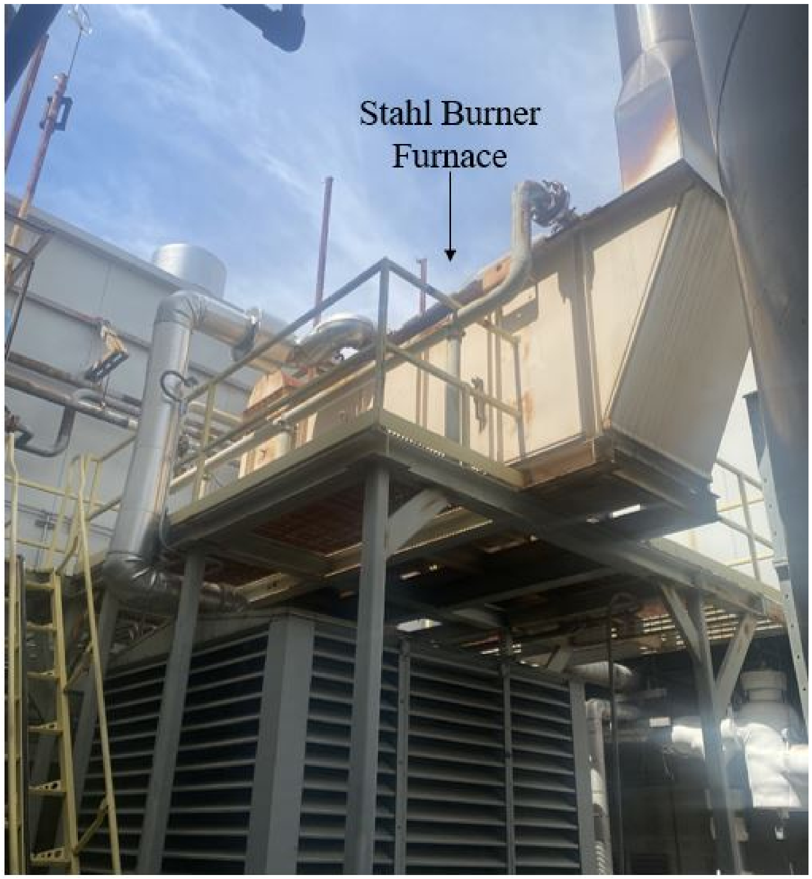

Figure 2.4: The Stahl heater furnace, located in the open outdoor bay is illustrated.

Following this section is a homogenizer section with several stages of wire screens and a flow-straightening honeycomb. There are two types of wire screens used in this rig: fine and coarse. Both filters have the purpose of filtering out particulates of varying diameters. The two coarse meshes have square grids with a 66% open area and an opening size of 6.9 mm whereas the two fine meshes have a 57% open area and an opening size of 3.2 mm. The honeycomb patterned flow straightener insert has a wall thickness of 0.5 mm and an opening diameter of 5 mm. Prior to collecting substantial data, the piping had to be opened to extract these meshes. As the screens were saturated with seed particles used for particle image velocimetry (PIV), they needed to be thoroughly cleaned and reassembled. Downstream of the screens and honeycomb is a converging-diverging nozzle, which accelerates the air to Mach 1.71 while reducing temperature and pressure. This leads into the wind tunnel test section where the water jet is injected and visualized. A side view of all of this, including the modified wind tunnel design, is shown in Figure 2.5.

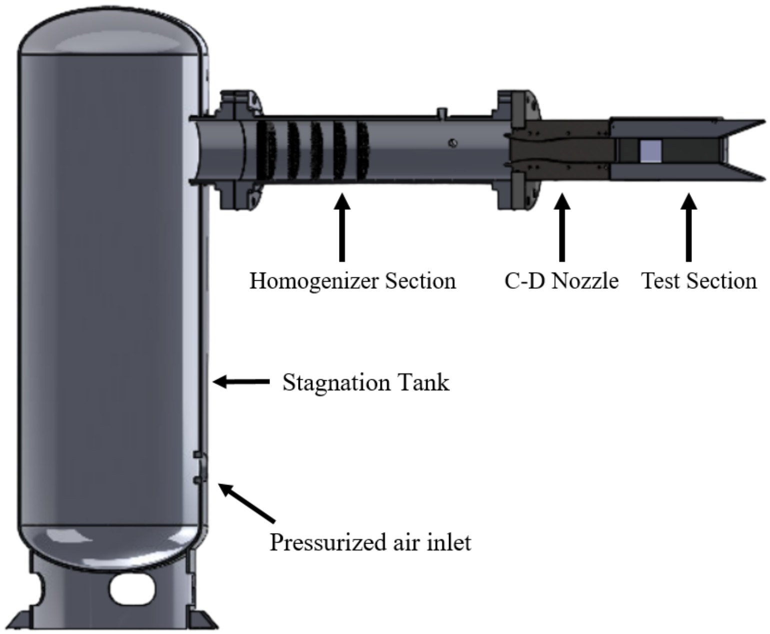

Figure 2.5: A side view of the CAD model for the rig is illustrated. The stagnation tank, homogenizer section, which includes the meshes and honeycomb flow straightener, converging-diverging nozzle with a design Mach number of 1.71, and the test section are shown.

2.1.2 Water Pressurization Pipeline Design

The liquid pressurization pipeline was developed in order to deliver high-pressure water into the supersonic JICF facility. Before purchasing piping, instruments, and fittings, a piping and instrumentation diagram (P&ID) schematic was designed to ensure that safety constraints and peak operating pressure conditions were met. Figure 2.6 and Figure 2.7 show the P&IDs for the system, with the first page showing the liquid water flow section before the injector and the second page detailing injection into the wind tunnel.

These diagrams outline the instrumentation used to direct water from the domestic water supply to the wind tunnel. Here, nitrogen from two tanks flows through a hand regulator with a maximum outlet pressure of 500 psi into a cylindrical water storage tank. The water used in the supersonic liquid JICF system is first filtered through a Pentek low-pressure

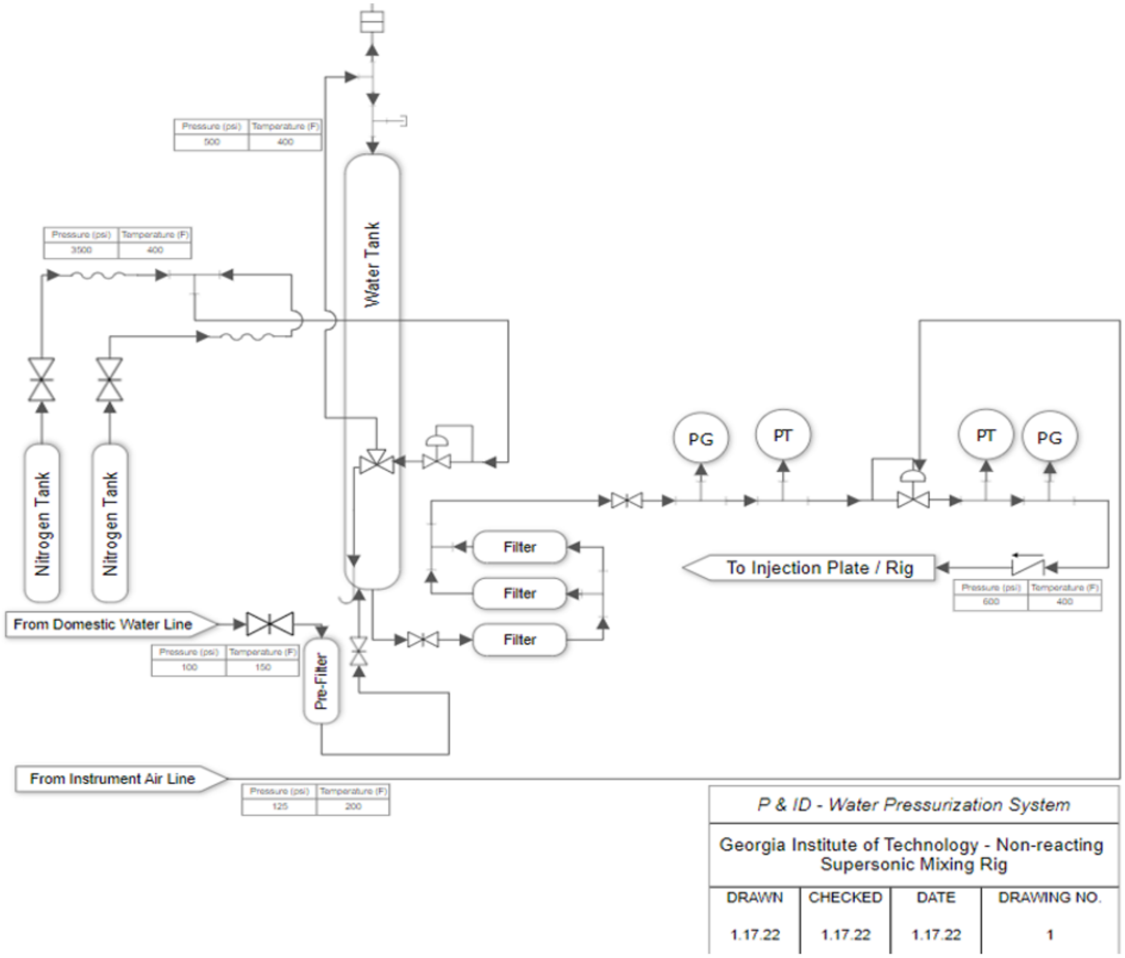

Figure 2.6: First page of the water piping and instrumentation diagram shows how nitrogen is used to pressurize and control water flow. The critical temperatures and pressures are shown in bounding boxes (PG = Pressure Gauge, PT = Pressure Transducer). The outgoing arrow to the injection plate continues on the second page.

pre-filter (model number: 158005), capable of removing solid particulates down to 10 microns in diameter. Then, water flows into the 68-liter storage tank and through a hand gate valve and solenoid valve. The solenoid is controlled via LabVIEW, remotely. Afterward, the now pressurized water flows through three 9052-10 Arrow Pnuematics in-line high-pressure filters to further filter out particles that are 10 microns or larger in case any solids were picked up in the tank or pipes. The liquid then passes into an air-actuated regulator, allowing a range of pressures to be remotely chosen. Finally, the liquid is directed through an injector plate and into the crossflow air stream. Positive displacement exhaust expels

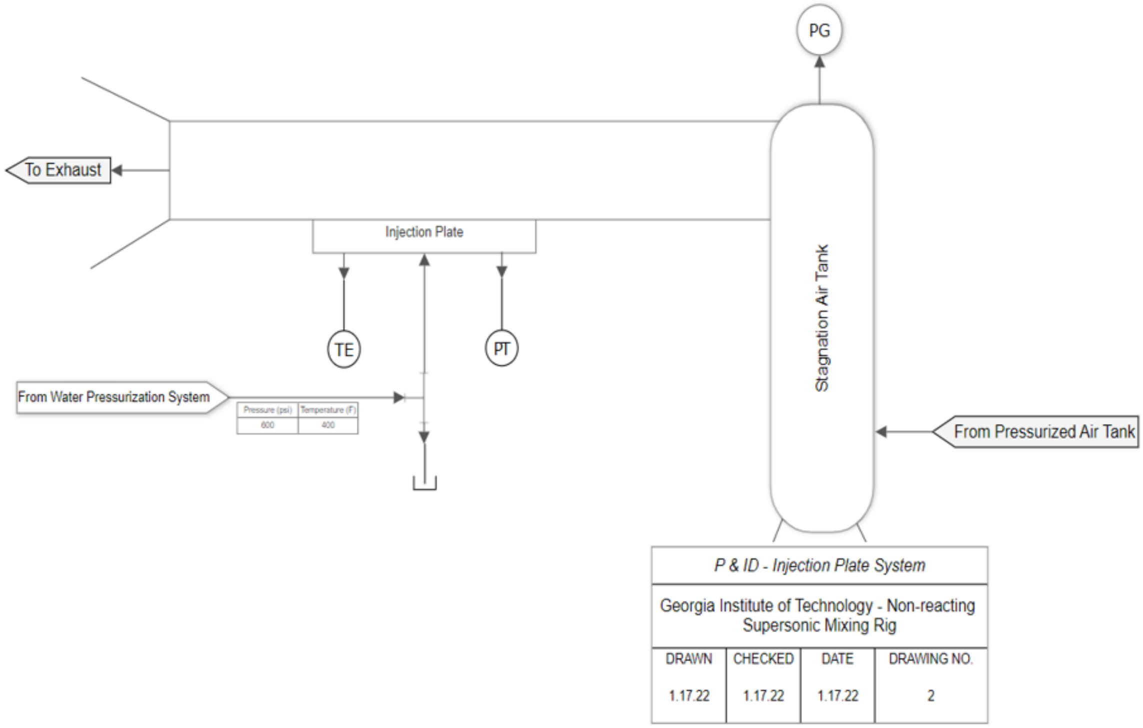

Figure 2.7: Second page of the water piping and instrumentation diagram shows the inlet air from the Norwalk air compressor into the stagnation tank. The inlet water from the first page is shown on a flag on the left. The mixed fluids are evacuated through the exhaust.

this air/water mixture out to the atmosphere. The total length of the pipe, throttling action in the regulators, and bends in the system all contribute to a pressure drop, which is quantified and discussed in subsection 2.1.6.

Safety is critical when working with relatively high water pressures. All Swagelok pipes used in this system had a maximum allowable pressure of 3500 psi, which gives this system a factor of safety of 7 to support the maximum tested injection pressure of 500 psi. The connectors, such as T-splitters, 90-degree bend connectors, and end caps, were further rated for 4500 psi. If the nitrogen pressure exceeds 700 psi in the case of regulator failure, the burst disk situated at the top of the water tank activates and vents both nitrogen gas tanks to the room exhaust. This avoids over-pressurization of the water tank, which would cause it to burst leading to more significant damage. Additional safety features and design considerations are outlined in a Standard Operating Procedures (SOP) document listed in the Appendix.

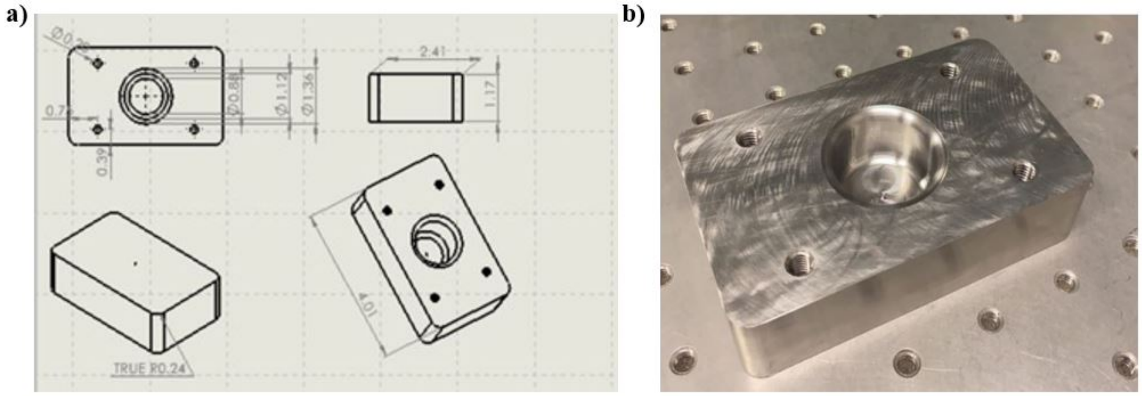

Figure 2.8: (a) CAD drawing and (b) image of the 0.5 mm diameter injector. The Aerospace Engineering machine shop handled the manufacturing of this component.

2.1.3 Injector Design

Creating a low-density droplet field is critical for applying optical diagnostics. A dense droplet field would (a) reduce the amount of laser light that the camera receives, and (b) make it immensely difficult to measure the droplet diameters when several droplets are overlapping with each other. Here, a 0.5 mm jet diameter is selected to minimize droplet densities behind the jet, which improves DIH data acquisition close to the jet [38] and further downstream for droplet sizing [39]. Another advantage of using a smaller jet diameter is that the slenderness ratio (L/D = 19) places the injected liquid in the transitional fluid flow regime, which is between laminar flow (L/D $<=$ 10) and turbulent flow (L/D $>=$ 100) regimes [40]. A turbulent L/D produces a more unpredictable and unsteady breakup, which enhances the atomization of individual particles, producing finer droplets. Smaller atomized particles also facilitate more complete combustion downstream [40].

2.1.4 Test Section Design

The 80 $\times$ 80 $\times$ 508 mm test section underwent several design iterations to (a) allow for easier window replacement if windows are soiled/broken, (b) provide enough optical access for imaging of the front-edge and downstream droplets, and (c) maintain a high safety factor to prevent window breakage. The original window design from Dan Fries provided optical access throughout the entire test section, as the windows spanned the entire width and height of the wind tunnel. This design is illustrated in Figure 2.9.

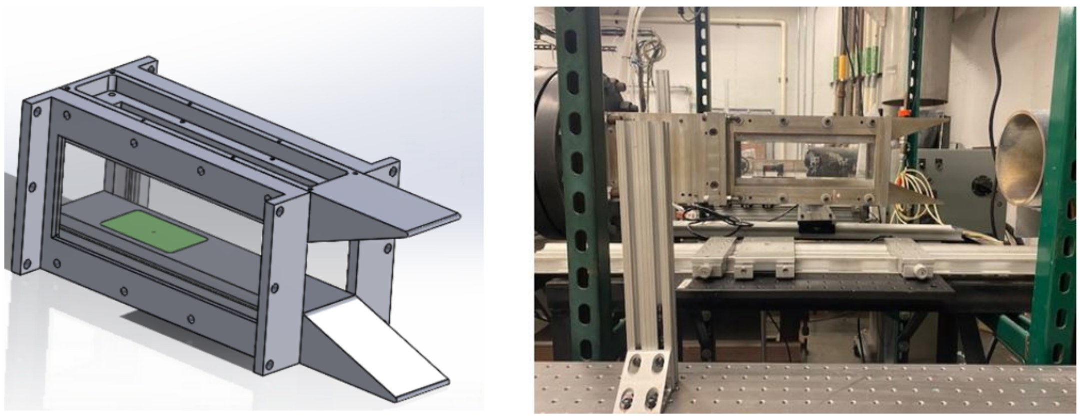

Figure 2.9: (a) CAD model and (b) image of the original test section design fitted with large quartz glass windows is illustrated.

One major downside of this design is that it utilized two large quartz glass windows that are 343 × 140 × 19 mm, making them expensive to replace. On top of this, the windows filled the entire test section, meaning that the entire wind tunnel had to be deconstructed to replace or clean the windows. After extensive use in prior work, the windows had permanent aberrations and laser burns engraved in the glass, causing issues with image quality. Additionally, PIV seed particles that were used in prior campaigns were also lodged in the homogenizer and stagnation tank. These particles would occasionally come loose and collide with the test section windows, permanently discoloring the interior of the windows, as shown in Figure 2.10. This necessitated either a glass replacement or a redesign of the wind tunnel test section with a more cost-effective window selection. To prevent seed particles from affixing to the windows in the future, the entire rig was dismantled and thoroughly cleaned.

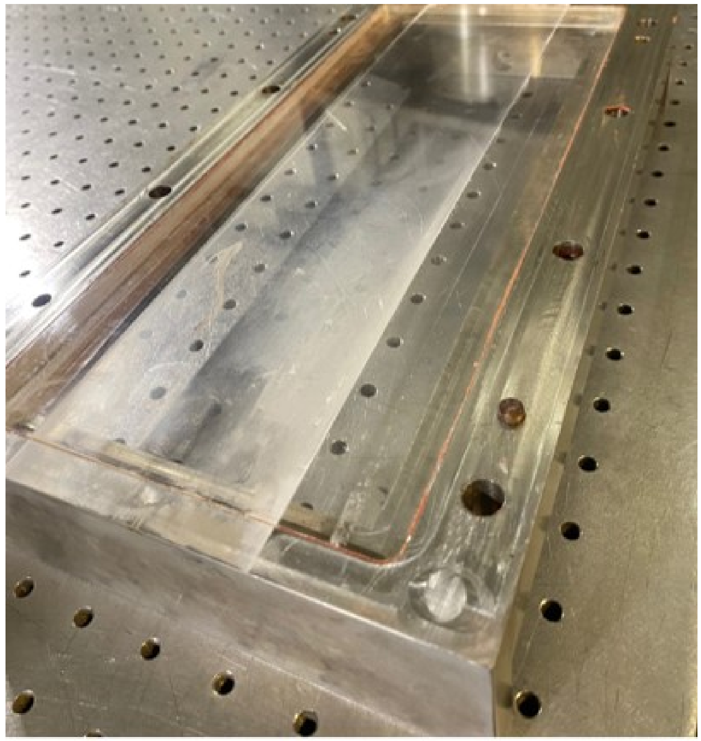

Figure 2.10: The scratched windows caused by PIV seed prompted a new design for the test section windows. Multiple attempts were made to remove the defect, including using isopropyl alcohol and a window lens cleaner.

In order to improve the optical quality of the windows, a second design of the wind tunnel test section was manufactured using 304 stainless steel. This design contained four high-precision anti-reflection coated BK7 windows that were 76.2 $\times$ 76.2 $\times$ 3 mm. As shown in Figure 2.11, this window design was unclamped and were were only held to the inside lip of the test section wall by a high-temperature gasket made of RTV silicone (600 °F max). Instead of using a single machined component, each side of the tunnel has 3 parts: (1) the brace where the windows are held, (2) the first set of flanges that bolt to the brace and the inlet piping, and (3) the second flange that bolts to the brace facing the exhaust. Because of this design, manufacturing time and material costs are reduced as it was not necessary to source a large block of 304 stainless steel and machine it down to the desired size.

This second design also had some drawbacks. First, because the windows were affixed

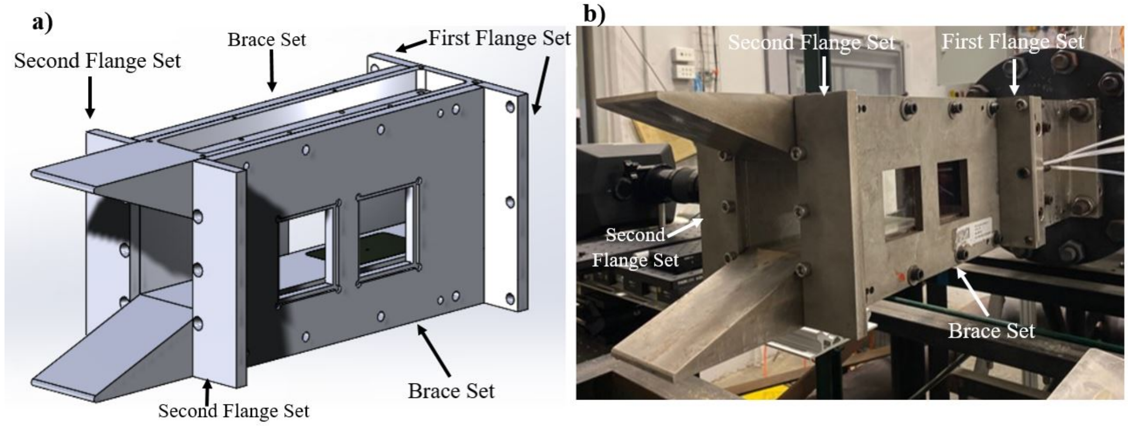

Figure 2.11: (a) CAD model and (b) image of the second window design for the wind tunnel test section is shown with 4 square windows. The three different parts that comprise the wind tunnel test section are denoted as the brace set, the first flange set, and the second flange set. The right-most pair of windows is used to collect data near the jet injection point and the left-most pair of windows is used for collecting droplet data far downstream.

to the lip via RTV, the only way to replace them would be to remove the entire test section like in the original design (although it weighed much less). The second issue was the choice of BK7 glass dimensions. Prior to committing to the design, safety factor calculations were conducted using Equation 2.1,

$$t = lw\sqrt{\frac{PKS_F}{2M(l^2 + w^2)}}. \tag{2.1}$$

Here, t is the thickness of the glass, L and W are the length and width, P is the maximum pressure on the inner window, $K = 1.125$ for unclamped designs, S_F is the safety factor, and M is the modulus of rupture for a particular material type. This equation was used to calculate the safety factor, which was found to be 3.45, assuming a crossflow pressure of 200 psi. It should be noted that this maximum estimated pressure after the isentropic expansion is unrealistic and the actual pressure is much lower. When compared to the elastic limit of the BK7 glass, plastic deformation should not occur either. However, some of the glass still shattered during experimentation and was sucked into the tunnel and expelled through the exhaust. This could potentially be due to thermal expansion effects that are not included in the safety factor calculations.

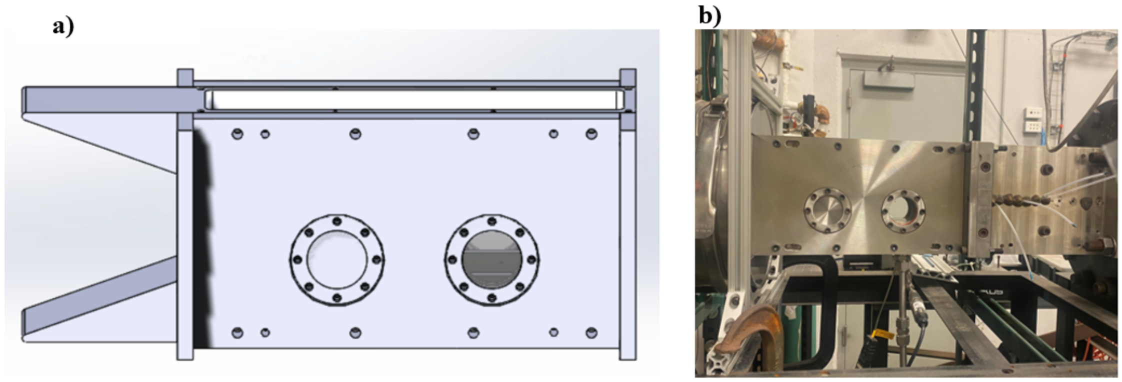

Figure 2.12: (a) CAD model and (b) image of the third window design shows circular window slots, one with a fused silica window in place and one with a metal window blank. If far downstream locations are desired, the blanks can be easily replaced with circular fused silica windows.

To further improve window performance, a third design was devised. An important aspect of window choice here was the ability to source windows quickly in case replacements were needed. Hence, off-the-shelf fused silica windows from Thorlabs with a low thermal expansion coefficient were selected. Figure 2.12 shows the third design of the wind tunnel test section and its implementation in the lab.

The three pieces of the new brace system for the wind tunnel test section are largely the same as the second design and still use 304 stainless steel. As the thermal expansion coefficient of BK7 was high, fused silica was chosen to remedy this issue as it has a significantly lower thermal expansion coefficient. Moreover, the new windows have no corners with a 50 mm diameter and thickness of 12.7 mm, raising the safety factor to 146 at atmospheric pressure conditions. Equation 2.2 shows the safety factor calculation for a double-clamped window design. The thickness, maximum stress, and safety factor can be found using,

$$t = D\sqrt{KD^2}, \tag{2.2}$$

$$S_{max} = \frac{KD^2P}{4T^2}, \tag{2.3}$$

$$S_{max} = \frac{F_a}{SF}. \tag{2.4}$$

Here, F_a corresponds to the elastic limit of the glass. Equation 2.3 and Equation 2.4 are utilized in conjunction with Equation 2.2 to find the maximum stress on the windows after the safety was determined. Based on these equations, it was found that the original quartz glass used in the first design had a safety factor of 35.6. Therefore, the third design has approximately a 4 $\times$ increase in safety factor over the first design. Thus, the maximum pressure on the glass would not cause the window to break, which was successfully tested in the experimental setup. Also, for this double-clamped method, the maximum pressure is actually on the edges where the glass touches the metal instead of in the center of the window. Thus, high-temperature RTV silicone was used to pad and affix the front and back edges of the window onto the frame of the brace and into the clamping plate, which uses eight screws to hold the window in place. Finally, this third design achieves enables quick and easy removal of the windows. Removing the clamping plate allows access to the windows, which can be pulled right out and replaced if the windows become damaged or dirty. The wind tunnel does not need to be disassembled in this design, which greatly improves maintenance and usability.

2.1.5 Exhaust Reducer Section

Previously, the supersonic JICF rig flowed inert gasses and no additional hardware was needed to connect the wind tunnel to the exhaust. However, with a liquid JICF system, significant quantities of liquid can leak out of the test section and flood the room if the crossflow velocity is not sufficiently high. Therefore, an exhaust reducer section, which joins the gap of the larger cross-section wind tunnel to the smaller diameter exhaust opening, was produced. Figure 2.13 shows the CAD model of the reducer and the implementation of the design in the test section.

A 80/20 aluminum frame was built to support the reducer and clamp it securely to the frame of the rig. It has been observed that during experimental runs at the steady state crossflow velocities, no water leaks past the exhaust reducer.

a) b)

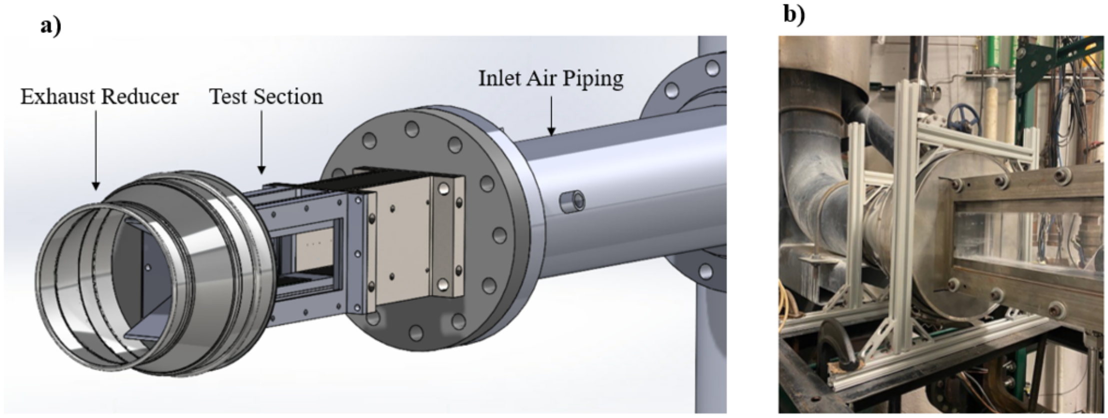

Figure 2.13: (a) CAD model and (b) image of the exhaust reducer is shown attached to the test section of the wind tunnel.

2.1.6 Flow Condition Measurements

Pressure transducers and thermocouples are added to the liquid as well as the gas flow paths to measure the pressure and temperature. All of the thermocouples used in these experiments are type J with a temperature range of 273 to 704 K (32 $^\circ F$ to 970 $^\circ F$). Since the maximum stagnation temperature is approximately 600 K, sensors with a higher temperature range, like type K, were not necessary. Two known temperatures, the freezing point (273 K or 32 $^\circ F$) and the boiling point (373 K or 212 $^\circ F$) of water, were used to calibrate and determine the accuracy of the thermocouple measurements. These type J devices have a reported reading accuracy of $\pm$ 0.75% and a response time of 0.6 seconds. Experimentally, the accuracy of the thermocouples was typically found to be within $\pm$1 K, which contributes to a small amount of uncertainty in the measurements.

For gas pressure measurements, two Omega PX309-500GI pressure transducers are used. One is tapped into the stagnation tank while the other is added to the conditioning section of the homogenizer. For water pressure measurements, a single Omega PX309-500A5V pressure transducer situated on the injector plate was used. In Figure 2.14, the target water injection pressure and the actual measured pressure are shown in relation to time. The dashed line shows the mean pressure over the data collection period of 6.30 sec-

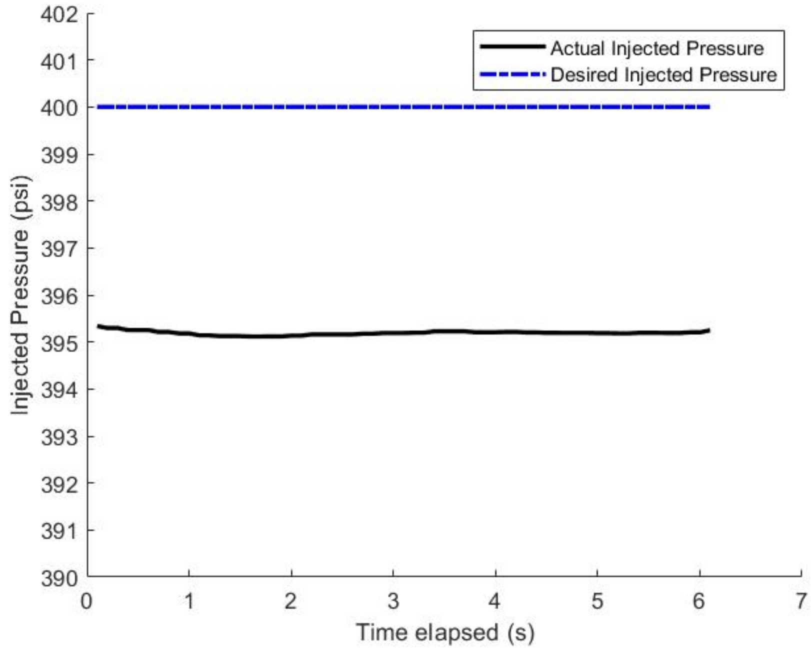

Figure 2.14: The difference between the desired and measured water injection pressures is shown as a function of time. The desired water injection pressure was 400 psi. The data taken during the first 6.30 seconds of injection shows that the deviation from the desired pressure is not very significant.

onds. For a commanded water injection pressure of 400 psi, the average injection pressure was measured to be 395.19 psi, which is a deviation of 4.81 psi from the target pressure. Pressure drop within the bends of piping and through the filters and instruments are likely the main causes of the deviation. These pressure drops represent a $\sim$1% deviation from the commanded values, which introduces a small amount of uncertainty into the measurements.

These small pressure drops are repeatable for all pressures tested from 0 to 500 psi. Here, the data were averaged from 5 sets of data taken on different days, spanning up to 400 data points per experiment. Indeed, for all pressures, the deviation from the desired pressure fell in the range of only 4.81 to 5.53 psi. The deviation over the entire data collection time for all pressures was also within 1 psi. Furthermore, results also show that as the pressure increased, the difference between the measured and desired injection pressures decreased, signifying that the transducer control system is more responsive at higher pressures. Potential sources of this effect could be a calibration offset or a steady state error between the commanded and measured pressures. In future work, an integrator term could be added to the pressure feedback controller in order to remove this effect.

2.1.7 LabVIEW Controls

In prior work, two sets of LabVIEW programs were used as the instruments needed to run the water injection system and the airflow system were split between two control boxes. In this work, all of the instruments were moved onto the supersonic JICF rig and combined onto a single control device (cRIOs). In order to accomplish this, input and output wires from existing instruments were rewired into the JICF rig. This included the solenoid valve, the control relay for the solenoid valve, the air-actuated valve, the feedback loop pressure transducers for the air-actuated valve, and several pressure transducers. After the instruments were re-routed to the JICF cRIO, new inputs and control algorithms were added to LabVIEW VI, and the combined VI is shown in Figure 2.15.

Because the water pipeline was new to this facility, a critical step was wiring the cRIO to the air-actuated pressure regulator and passing the correct control current to the instrument. Thus, the following conversion in Equation 2.5 between the desired injecting pressure and the current supplied to this regulator is computed within the LabVIEW environment and the current is passed from the acquisition device to the regulator. The conversion equation with pressure in units of psi is,

$$I = (P_{desired} + 14.7)\frac{0.016}{1000}. \tag{2.5}$$

This current value is then converted to a fixed point data type to be read by cRIO in order to control the regulator.

2.2 Rig Thermal Expansion

When the rig is run at its maximum stagnation temperatures of about 550 to 600 K, the sustained heat flux from the air causes the metal to thermally expand. Thus, the test section moves in both the lateral and longitudinal directions. When high magnification optics are used, it is difficult to accurately track the location of the field-of-view with respect to the water injection location. In order to improve the positioning of optical diagnostics, reference measurements were taken near the bottom of the test section. Figure 2.16 depicts the relative longitudinal motion, measured by the pixel displacement of the ground (the black box) over time. The lateral movement was determined by injecting at low pressure

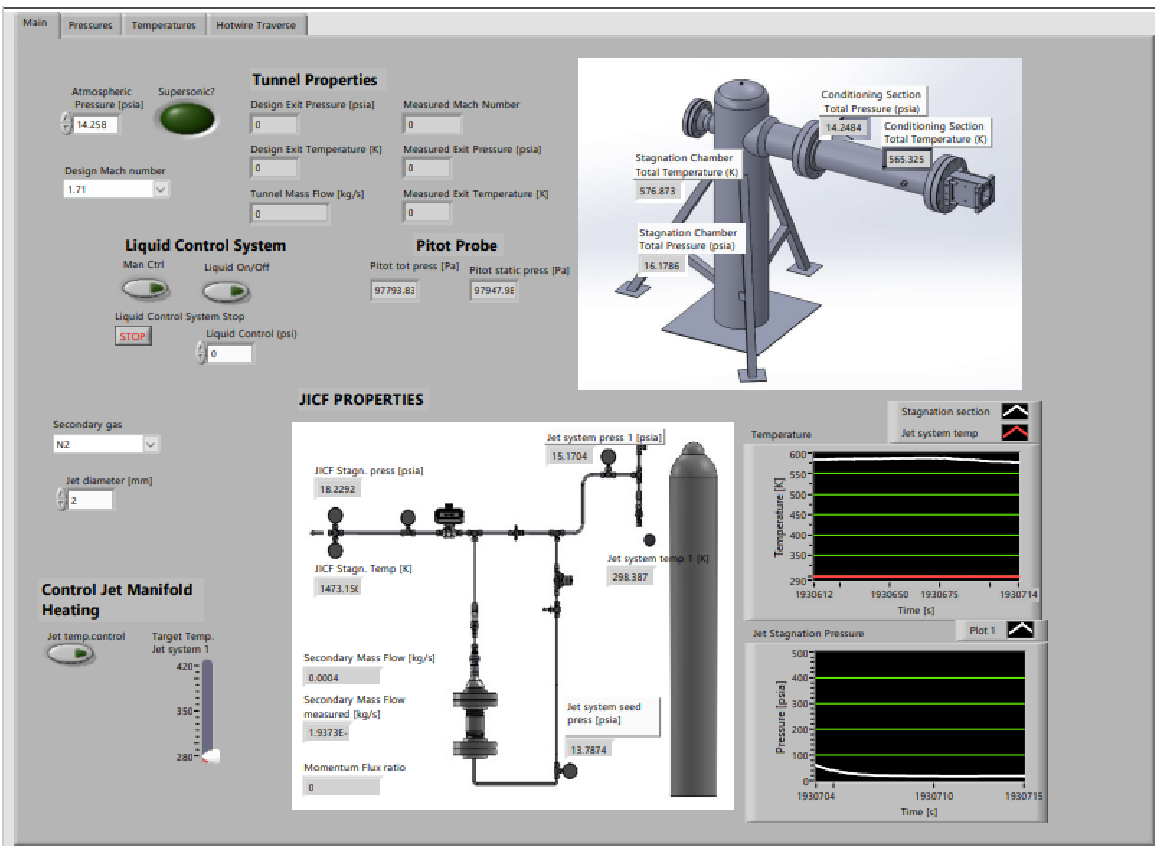

Figure 2.15: The combined LabVIEW VI is illustrated during an experimental run. Values for the stagnation and conditioning pressure and temperature are shown on the CAD model of the rig in the top right corner. Other important metrics including the liquid control system and temperature/pressure graphs are also shown.

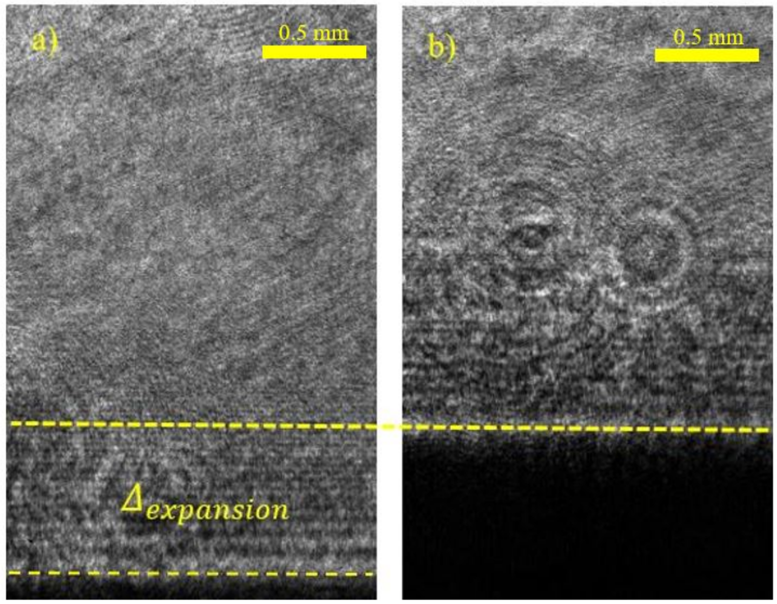

Figure 2.16: An example of the rig motion in the longitudinal direction is shown. (a) A DIH image taken at a stagnation temperature of 292 K and (b) a DIH image taken at 550 K are compared. The expansion is denoted in between the two yellow dotted lines in (a).

and watching the column move as the temperature of the rig was increased. It is determined that the rig moved in the streamwise direction and upwards over time due to thermal expansion.

After the pixel displacements were found in this study, Figure 2.17 was constructed to show the test section movement as a function of temperature. Here, each temperature was held for at least five minutes before the image was taken to ensure that the tunnel temperatures are close to steady-state. Because the flow rate of air is high for the desired stagnation crossflow pressure condition (around 33 to 34 psi) this drains the compressed air tank very quickly. Thus, longer test times were not used for these experiments.

In this figure, the horizontal error bars represent the measured standard deviation in temperature of approximately 10 K that was captured during the experiment. Assuming that thermal expansion is linear, an expected expansion line is calculated by using,

$$\Delta L = L_o \alpha (T_1 - T_0). \tag{2.6}$$

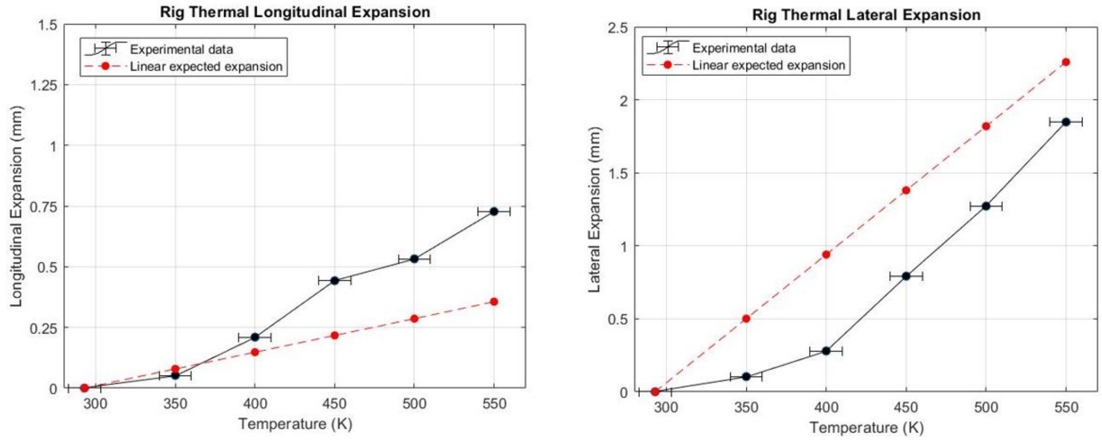

Figure 2.17: The longitudinal and lateral thermal expansion graphs are shown as a function of temperature. This rig tends to move more than the predicted amount in the longitudinal direction and less than the predicted amount in the lateral direction. The error bars correspond to the measured temperature standard deviation.

Here, α is the linear expansion coefficient for 304 stainless steel and is estimated to be $17.3 \times 10^{-6} \frac{m}{m^{\circ}C}$. The test section dimensions L_o of 508 mm in length and 80 m in height are then used to estimate the amount of thermal expansion. Overall, this rig tends to move more than the predicted amount in the longitudinal direction and less than the predicted amount in the lateral direction. While the expansion is small, on the order of 1 to 2 mm, this is a significant amount for high magnification experiments. Thus, prediction and external reference techniques were used in this work to improve positioning accuracy.

CHAPTER 3

OPTICAL MEASUREMENT TECHNIQUES

Mixing between the liquid and air in a wall-normal supersonic JICF configuration is dependent on the flow characteristics that are generated by the liquid jet injection process. This chapter discusses the optical setups, theoretical foundations, and processing codes that are implemented in order to investigate flow features in the windward and leeward sides of the water jet.

3.1 Windward Side of Jet - Schlieren Technique

The first technique that is utilized to observe the front-edge of the jet is schlieren. This variation of shadowgraph imaging relies on the density differences inside the flow, which causes light refraction disturbances and light intensity fluctuations. There are several different types of schlieren systems, but in this work, the Toepler lens setup is used in order to achieve high magnification measurements. Figure 3.1 shows some of the optical setups for schlieren methods that can be used to visualize density gradients in a transparent (or semi-transparent) flow field.

The main components needed for the Toepler configuration are a broadband light source, a collimating lens, a knife-edge, a receiving lens, and a camera. In this non-intrusive measurement method, density gradients or refractive index gradients, $\partial n/\partial y$, cause light propagating through the flow field to bend. This angle of refraction in the y-direction is then given by,

$$\epsilon_y = \frac{1}{n}\int \frac{\partial n}{\partial y} dz. \tag{3.1}$$

If a knife edge is placed at a focal point in the flow, the knife edge can be used to block some of the refracted light, thereby enhancing images of the density or refractive index gradient

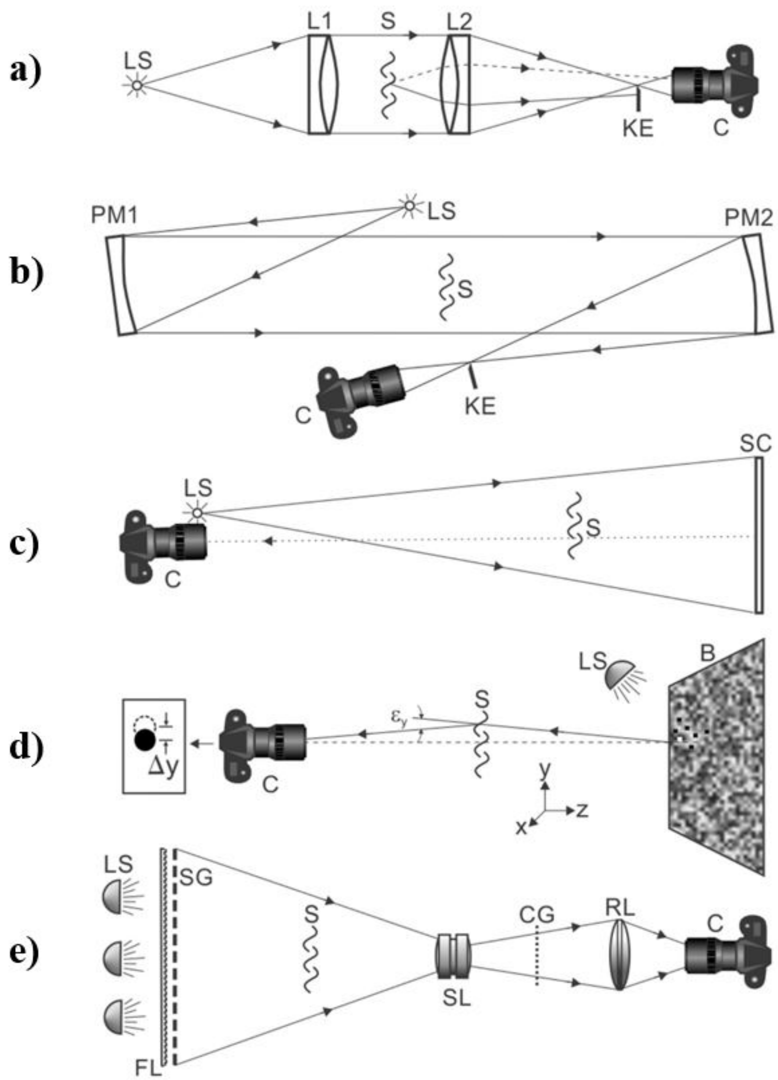

Figure 3.1: Five schematics showing typical schlieren experimental configurations are illustrated. (a) A Toepler lens setup, (b) Z-type schlieren system (which has been used in this rig before) (c) direct shadowgraphy, (d) background-oriented schlieren (BOS), and (e) focusing schlieren configurations are shown [41].

features. Note that because schlieren systems have an inherent minimum threshold value for $\partial n/\partial y$, there is a minimum angle that can be visualized. This angle can be calculated if the second lens (the lens placed in the light path after the medium) has a known focal length (F_{L2}) such that,

$$\epsilon_y = \frac{a}{F_{L2}}. \tag{3.2}$$

Equation 3.2 displays this new equation, with a representing the vertical distance between the refracted ray and the knife-edge plane. If quantitative schlieren techniques (which include calibrated schlieren, rainbow schlieren, and BOS [42]) are used, this distance can be calculated from measured data. With the distance analyzed, the refractive index n can be found from solving Equation 3.1. In this discussion, it is important to mention Gladstone and Dale, who discovered that the relationship between the refractive index n and the gas density ρ can be represented with a constant k for different mixtures such that,

$$k = (n - 1)/\rho. \tag{3.3}$$

This relation forms the basis for using schlieren and similar shadowgraph techniques for to study gaseous flows. In cases where the refractive index is known, these relationships can also be used to find the line-of-sight gas density [43]. Despite the clear relationships between density, refractive index, and light deviation, quantitative schlieren methods are extremely difficult to calibrate accurately. Thus, most schlieren techniques are used to provide a qualitative measurement of shock wave locations. In this work, grayscale schlieren is used to help image the bow shock and simple jet penetration features.

3.1.1 Experimental Schlieren Setup

Utilizing this information, a schlieren system was constructed for the supersonic JICF experiments. Figure 3.2 shows the Toepler configuration implemented in these experiments, which uses 100 mm focal length (FL) plano-convex collimation and receiving lenses. This lens combination allows for a high magnification field-of-view of flow features in the test section.

A pulsed single-element white LED light (DRAGON Series HPLS-36D7500) is used to provide illumination for the experiment. Here, the LED emission is synchronized with the exposure timing of different cameras used for high-speed and high-resolution measurements. On the receiving side of the wind tunnel, a vertical knife edge is placed at the

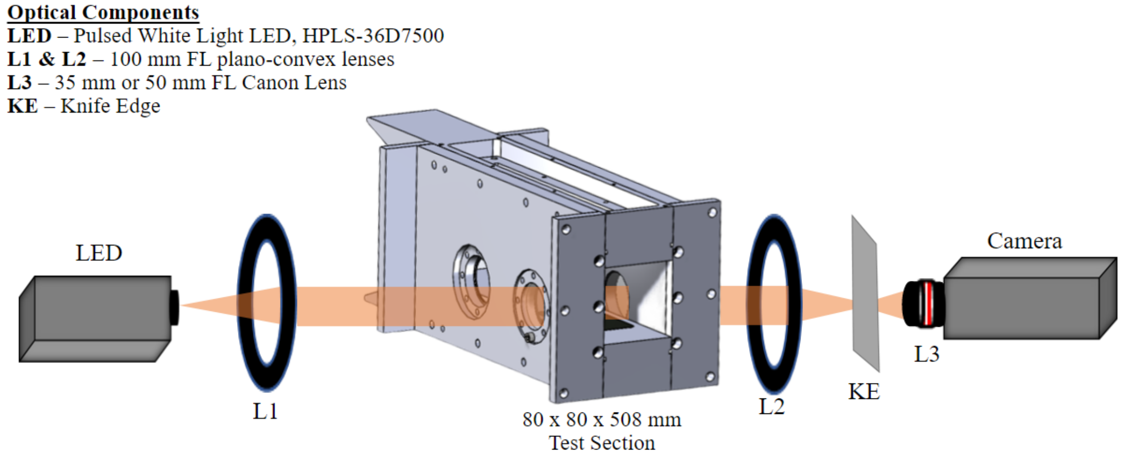

Figure 3.2: The Toepler configuration schlieren setup is used to characterize supersonic JICF flow features. All optics in this setup are placed on rails so that the system can be easily moved to image different locations in the flow.

focal point of the second lens to block approximately 60 to 70% of the rays and create the schlieren image. Here, 35 mm and 50 mm FL lenses are placed in front of the camera detector and are adjusted to focus on features in the water jet plane. For low-speed camera applications, the LED light driver voltage is maximized and the pulse duration was minimized to approximately 100 ns to effectively freeze motions in the flow. High-resolution, low-speed images are captured using a Blackfly camera (BFS-U3-32S4M, 2048 $\times$ 1536 pixels, 126 Hz sampling frequency, 3.45 μm pixel size, 5 μs minimum exposure time, 10-bit depth).

For high-speed camera applications, the LED is left on and timing is controlled using the camera exposure time. Here, a high-speed Shimadzu HPV-X2 camera (400 $\times$ 250 pixels, 5 MHz maximum sampling frequency at full frame, 200 ns exposure, 10-bit depth) is used to capture flow dynamics at higher imaging rates but at lower spatial resolutions. After testing both of these camera configurations, it was determined that the higher spatial resolution camera provided clearer images due to the higher pixel count and shorter pulse duration, which reduced blurring effects.

3.2 Windward Side of Jet - Digital Inline Holography Technique

The majority of JICF experiments conducted in subsonic and supersonic wind tunnels and expansion tubes focus on measuring front-edge deformation, droplet breakup, and injector design variations [44, 45, 46]. Typically, imaging diagnostics, such as low-speed schlieren imaging, OH* chemiluminescence, and OH planar laser-induced fluorescence (PLIF), are used to investigate the shock wave structure and combustion phenomena [44, 45, 47, 48, 49, 50]. These techniques use either LED or laser light sources and can be adjusted to interrogate different portions of the liquid jet breakup. While the aforementioned imaging diagnostics excel in producing high spatial and temporal resolution data, multiple diagnostics are typically needed to study density gradients, jet instabilities, and droplet breakup features.

Digital inline holography (DIH), on the other hand, has not been previously explored for use in supersonic JICF experiments to study injection point jet instabilities [51]. Outside of a few experiments on aerated jets [32, 33, 34, 35], DIH has not been previously used to study liquid jet in supersonic crossflow problems in general. DIH differs from other techniques because it uses numerical refocusing to allow the camera focal depth to be altered in post-processing [52, 38]. Even when the camera is focused to a plane outside of the liquid jet injection plane, the focal plane can be shifted into the center of the flow in post-processing to accurately determine the size, morphology, and three-dimensional location of droplets as small as a few microns. By utilizing image segmentation of multiple frames and a high-speed camera, droplet velocities can also be deduced [52]. DIH has been successfully implemented for studying the impulsive breakup of liquid jets, droplet formation in aerated jets, and particle generation in propulsion applications [53, 54, 55, 56, 57, 58, 59, 35, 34, 33, 32]. By using DIH to study droplet breakup in liquid jet in supersonic crossflow applications, more droplets from multiple focal depths can be accurately determined. Additionally, jet, droplet, and bow shock morphologies can be studied using a single, high depth-of-field three-dimensional imaging technique.

In digital inline holography, three-dimensional information is essentially stored in the interference fringes that are generated when the laser is passed through the object field, creating a hologram. This raw hologram data is then collected on a two-dimensional sensor, which can be numerically refocused in post-processing. This method is attractive because it is simple to set up, can use all of its pixels for high-resolution imaging, and has a larger phase sensitivity compared to other holography techniques, like off-axis holography. The downside to this technique is that there is no reference beam for directly calculating phase delays, not only making it more difficult to use for phase measurements but also creating a twin-image effect during numerical refocusing [59]. However, because of its simplicity, it can be used to study flow fields that have a moderate number of particles. In Figure 3.3, a raw hologram of a droplet spray field is presented showing a nozzle spraying pressurized water into the field of view. Interference diffraction patterns are clearly visible in this raw hologram. As the droplets are reconstructed to the correct focal plane, the edges of the droplets become sharper and the interference patterns are reduced. The work presented in this thesis aims to reconstruct the droplet field like in this example but in a supersonic JICF scenario rather than in a free-stream droplet plume experiment.

In DIH, when the laser beam is introduced to the object field, some light diffracts off the particles while some pass through to the other side. The beam that diffracts off the objects is called the object beam while the beam that passes through is used as the reference beam. Those two beams combine and are superpositioned onto the camera sensor array, or the charged coupled device (CCD), which causes interference diffraction rings. This diffraction pattern can be described by the Kirchoff-Fresnel integral [60],

$$\Gamma(\xi^{'},\eta^{'}) = \frac{i}{\lambda}\int_{-\infty}^{\infty}\int_{-\infty}^{\infty} h(x,y)E_R(x,y)\frac{\exp(-i\frac{2\pi}{\lambda}\rho^{'})}{\rho^{'}}dxdy, \tag{3.4}$$

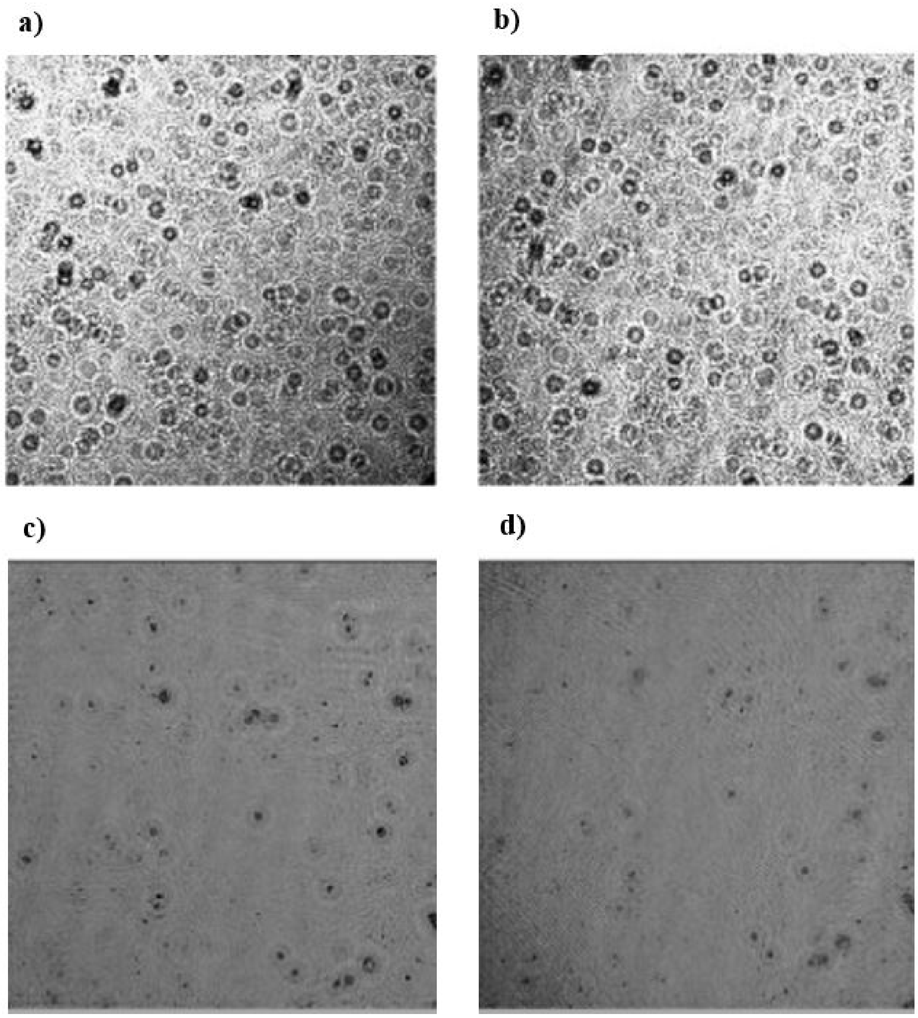

Figure 3.3: (a), (b) Two frames of raw out-of-focus holograms of a free-stream water spray are shown. (c), (d) These images can then be numerically reconstructed or refocused to the focal plane do the droplets showing clear droplet edges [38].

where,

$$\rho' = \sqrt{(x-\xi')^2 + (y-\eta')^2 + d}. \tag{3.5}$$

Once the raw hologram is captured, it can be reconstructed into a virtual image via a process called numerical refocusing. This allows the raw image to be moved from an out-of-focus plane to the focal plane where droplets occur, as shown previously in Figure 3.3. The raw electric field of the hologram Γ relies on the convolution of the particle field function $h(x, y)$ and reference electric field $E_R(x, y)$. By estimating the pixel sizes Δx and Δy, it is possible to successfully refocus the image to the desired focal plane. These distances are easily computed with a physical calibration grid (such as a dot grid) to map the spatial measurement to pixel space on the camera CCD.

Once the raw intensity of the flow field I_n is captured on the camera, forward and inverse Fourier transforms can be used to compute the reconstruction of the raw hologram intensity Õ to different focal planes using,

$$\tilde{O}(x, y, z) = \mathcal{F}^{-1}[\mathcal{F}(I_n(x, y) \cdot R^*(x, y)) \cdot G^*(f_x, f_y, z)], \tag{3.6}$$

where x and y are the spatial coordinates, z is the reverse propagation distance, E_R^* is defined as the conjugate reference wave (typically set to unity for collimated DIH) and G^* is the conjugate of the Kirchhoff-Fresnel diffraction kernel [38]. Here, λ is the laser wavelength. The terms f_x and f_y are the x and y frequency coordinates. By using the numerical refocusing equations to back-propagate the DIH images, the reconstruction enables visualization and refocusing of the objects in the flow field for accurate droplet sizing. There are other viable techniques to compute the reconstruction of the raw hologram, like the convolution method, but the fast Fourier transform method via MATLAB is used to refocus the images in this work due to its speed and efficiency.

In some extreme environments, thermal gradients and shock waves can cause optical distortions that obscure particle diffraction patterns. In those cases, phase conjugate mirror [61, 62], a polarized reference beam [59], or a tilted reference beam [59, 63] can be introduced so that the hologram is not self-referenced. The tilted reference beam method is also called off-axis holography, and it can significantly reduce noise and distortions when phase objects are present, making object edges more clear, discernible, and sharp. Using this method, it is possible to remove the aberrations using post-processing numerical methods. While there are shock waves present in these experiments, it has been determined that there are no phase distortions since the shock waves are far from the jet and droplet regions

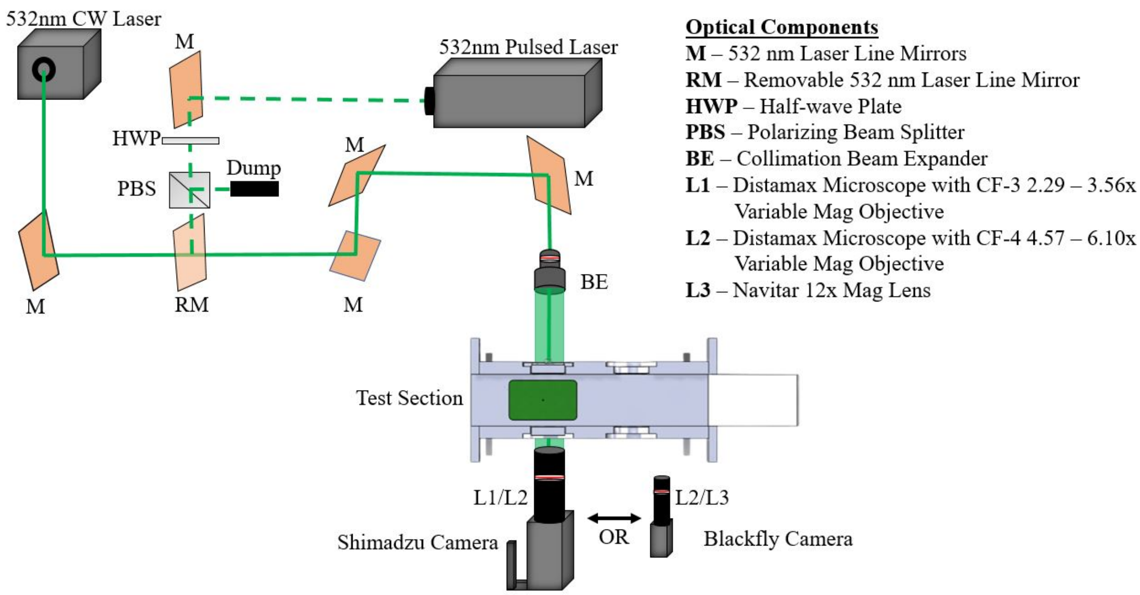

Figure 3.4: The 532 nm digital inline holography setups using continuous wave and pulsed lasers are illustrated using the same optical path into the test section, with the exception of a removable mirror. The laser beams are spatially collimated and expanded to ensure a uniform light distribution. Two different cameras can be used.

of the flow. Therefore, off-axis holography was not needed for these experiments.

3.2.1 Experimental DIH Setup

For the digital inline holography experiments, two lasers are utilized - a continuous wave (CW) laser and a pulsed nanosecond laser. To quantify the jet penetration, front-edge breakup, and droplet velocities, the continuous laser is used. Here, a continuous 532 nm Photonics Industries (DS20-527 532 nm, 700 mW) laser beam is expanded, collimated, and passed through the 80 mm $\times$ 80 mm square test section. Collimation and spatial calibrations are executed using a shear plate and dot grid (1 mm spacing). The light that is diffracted off of the flow field is magnified using either a CF-3 objective (3.56 to 2.29$\times$ magnification) or a CF-4 objective (6.1 to 4.57$\times$ magnification) and K2 Distamax long-distance microscope, as displayed in Figure 3.4.

In this system, the RM (removable mirror) is displaced when the pulsed laser is non-operational so that the CW laser light can freely pass through the test section. The laser is redirected several times until it reaches the BE (beam expander). The BE is essential for proper hologram capture because it not only expands the beam, but it allows the user to control how convergent or divergent the beam is. The divergence is calibrated using a shear plate to ensure that the magnification of objects in the test section does not change with depth. For data acquisition with the CW laser, the sampling rate and exposure on the high-speed Shimadzu HPV-X2 is set to 5 MHz and 110 ns in order to minimize motion blur and acquire a series of time-resolved frames. The CW laser power is approximately 800 mW, measured with a PM100D Thorlabs power meter. This meter is capable of measuring laser energy from 100 pW to 200 W.

While holography is useful for numerical refocusing, it is also possible to put the focal plane of the camera directly in the plane of interest to capture a coherent image of the flow field. While these images cannot be accurately refocused due to twin-image effects, this method enables the capture of high resolution jet edges. Examples of coherent images at the centerline of the water jet are shown in Figure 3.5. The first image is a 100 psi, or J = 7.3, jet in a supersonic crossflow. Alongside it is an image at subsonic crossflow speed with a 30 psi water injection pressure. Here, caustics can be seen inside the water jet from the refraction of the laser light. Because of the low velocity of the crossflow air, the water column stays relatively straight and its penetration depth greatly increases.

3.3 Leeward Side of Jet - Pulsed Digital Inline Holography Technique

While high-speed DIH is great for time-resolved information, the low resolution of the Shimadzu HPV-X camera severely limits the size of droplets that can be captured inside the flow. Thus, a pulsed nanosecond Litron laser (model: L 135-15 PIV)synchronized with a Blackfly camera (BFS-U3-32S4M) and Navitar 12× magnification lens are used to drastically increase the resolution and capture instantaneous shots of droplets at several downstream locations. The experimental setup of this is also shown in Figure 3.4. Here, the laser beam uses the same optics as the windward DIH setup by adding the removable

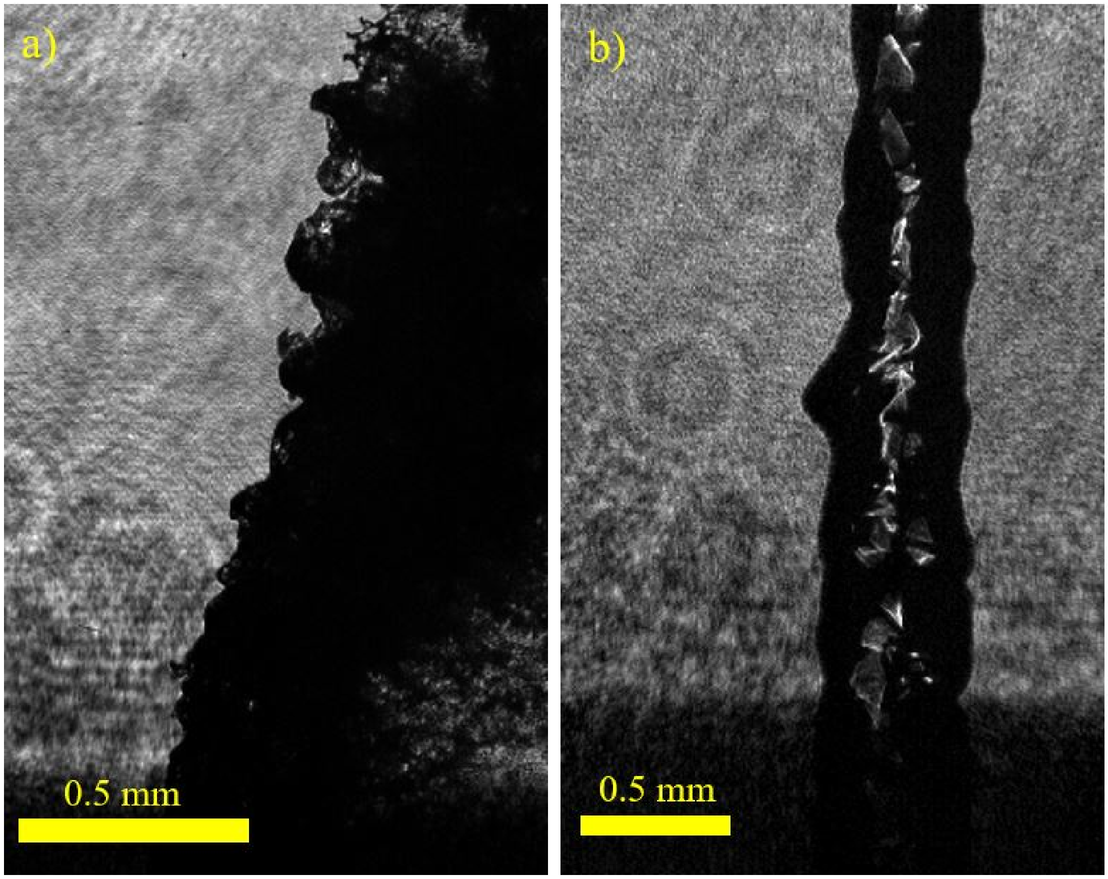

Figure 3.5: (a) Coherent image of a 100 psi water jet injected in a supersonic crossflow is shown. Here, front-edge instabilities on the shear interface layer are visible, along with the bend of the jet. (b) A coherent image of a 30 psi water jet injected into a subsonic crossflow is shown. Here, there is a lack of strong surface waves from instabilities leading to a relatively straight water column. Caustics from light refraction are also visible.

mirror. To test different horizontal positions in the flow, the beam expander path and the camera are both put on translational stages. To access different vertical positions in the flow, mirrors are used to move the beam upward and a vertical jack is used to adjust the camera location.

To accurately time the Litron laser pulses (10 Hz in these experiments) with the camera exposure, the signals that control the laser flashlamp and Q-switch were sent to an oscilloscope and timing box. Here, the timing box was used to set the flashlamp signal 14 ms before the Q-switch signal to maximize the laser output intensity. Then, the camera trigger time was set so that the camera exposure overlaped with the Q-switch signal. All these signals are visualized in Figure 3.6.

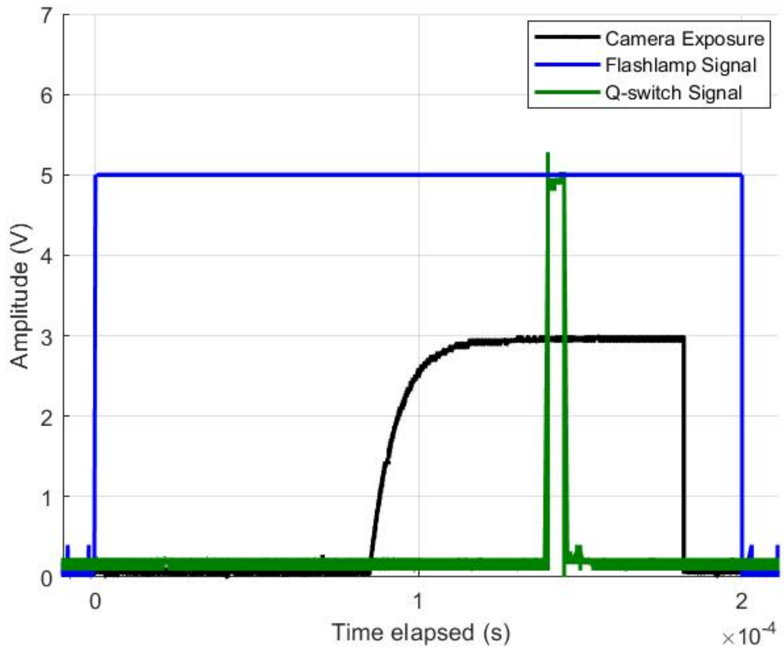

Figure 3.6: The camera exposure, flashlamp signal, and Q-switch signal are observed for the pulsed DIH setup. The optimal delay between the flashlamp signal and Q-switch signal was found to be 14 ms.

3.4 Leeward Side of Jet - Phase Doppler Particle Analyzer

Particle Doppler Phase Analyzers (PDPA) are commonly used in JICF experiments to retrieve droplet velocities and diameters, as well as deduce constants for penetration depth fits. To capture the information, this technique uses two Phase Doppler Interferometer (PDI) lasers. The probes, a transmitter and a receiver, are typically oriented at off-axis angles. Then, the two laser beams are crossed to form an intereference pattern inside the flowfield filled with droplets or particles. When the droplets and particles interact with the interference pattern, particle sizes can be inferred from the resulting signal. As its name suggests, a Doppler effect occurs at the intersection of the laser beams because the particles are moving. Thus, the droplet velocities can also be characterized as it is proportional to

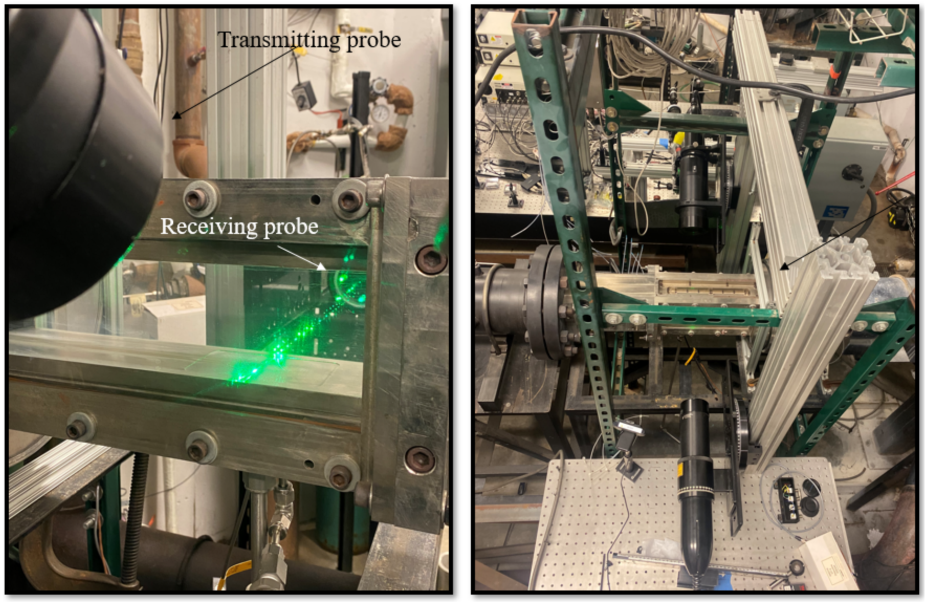

Figure 3.7: The PDPA phase doppler interferometer is shown here with the transmitting probe and receiving probe. Two 532 nm laser beams cross in the particle field so that droplet velocities and diameters can be characterized.

the Doppler difference frequency measured at the receiver [64]. In this technique, particle diameters are inversely proportional to the frequency, so both velocity and size are deduced using this method. As this technique is dependent on the wavelength of the laser and not the intensity, there are no beam attenuation errors that occur in denser areas of a spray. In this work, a quick PDPA campaign was done at several locations downstream of the 0.5 mm injector. Figure 3.7 shows the experimental setup that was utilized to simultaneously extract droplet diameters and velocities.

Light refraction and scattering and its accompanying Doppler effect are the governing mechanisms for PDPA. The amplitude functions for light scattering for the two beams that cross can signify the variation of scattering of different particles. Both beams have a separate function, given as,

$$S_{11}(m, \theta, d) = \sqrt{i_1} exp(j\sigma_1), \tag{3.7}$$

$$S_{12}(m, \theta, d) = \sqrt{i_2} exp(j\sigma_2), \tag{3.8}$$

where the beams are assumed to be linearly polarized, reflection and focal line phase shifts of π and $\frac{\pi}{2}$, respectively, are neglected, and double subscript indices (S_{11}) signify that only polarization of the first beam is taken into consideration. The θ constant refers to the angle of the incident ray and the divergent ray, d is the diameter of the particle, and m is its corresponding refractive index. Because the two beams can be considered independent when a particle flows into the cross-path region, separate scattered light waves can be described as,

$$E_1(m,\theta,d) = S_{11}(m,\theta,d)\frac{exp(-jkr + j\omega_1 t)}{jkr}, \tag{3.9}$$

$$E_2(m,\theta,d) = S_{12}(m,\theta,d)\frac{exp(-jkr + j\omega_2 t)}{jkr}, \tag{3.10}$$

where the wave number is given as $k = \frac{2\pi}{\lambda}$ and the angular frequency is ω. With these pieces of information, combining the complex amplitudes from the beams results in the total intensity. The general equation for the relationship of the phase difference of the scattered light, σ, follows the van de Hulst approach [65] and is given as,

$$\sigma = \omega_D t + \eta_{1n} - \eta_{2n}, \tag{3.11}$$

where η, the trajectory factor, is the proportion of the spatial coordinate in the z direction to the incident beam radius. If the phase difference in the scattered wave fields, σ, is known, then the following equation, Equation 3.12, can be computed such that,

$$I(m,\theta,d) = (|E_1|^2 + |E_2|^2 + 2|E_1||E_2|cos\sigma). \tag{3.12}$$

This equation describes the sinusoidal intensity variation seen in the interference pattern as $2|E_1||E_2|cos\sigma$. One last defining feature of the PDPA technique is the ability to compute the phase shift in particle movement. The phase shift forms the Doppler difference frequency, which can be calculated by examining the time delay collected at the two detectors τ_{1-2}. This is then divided by the Doppler period τ_D. The phase shift is calculated using,

$$\phi_{1-2} = \frac{\tau_{1-2}}{\tau_D} \times 360^{\circ}. \tag{3.13}$$

The particle velocity and diameter can finally be analyzed by the computer system attached to the probes. PDPA uses two beams to create diffraction fringes within a transparent or semi-transparent flow medium and then uses the Doppler effect to compute the phase shift. Therefore, it is a viable technique that can be applied to the leeward side of the jet to determine the droplet size and velocity at the same time. However, it should be noted that, in practice, PDPA data can be difficult to interpret. In many cases, PDPA data can often be thrown out by the system, making it difficult to ascertain if the measured data is biased. Additionally, it is also difficult to determine if shock wave distortions or dense particle fields are skewing the data. Because the sampling regions for this work are small and close to the tunnel floor, it is also difficult to determine if reflections from the tunnel are contributing to the measurement. Therefore, alternative direct imaging methods like DIH are recommended for confirming PDPA results.

CHAPTER 4

WINDWARD SIDE OF JET - RESULTS AND DISCUSSION

There are numerous features at the front edge of the jet that can be used to determine jet penetration, droplet breakup, and liquid entrainment. These values are useful for estimating the overall efficiency of the combustor. This chapter delves into the optical techniques used to visualize flow features, penetration depth, K-H and R-T instabilities, and windward droplet breakup. As windward droplet breakup near the tunnel floow has not been discussed before in the literature, the findings in this work form the basis for improving our understanding of new flow features observed at the shear interface between the liquid and gas flows. Because these features occur only for higher-diameter injectors, injector diameter effects can also be inferred.

4.1 Schlieren Imaging

The Toepler schlieren technique was used in these experiments to obtain two-dimensional images of the jet as it penetrated into the crossflow. In this setup, a pulsed white LED is connected to an oscilloscope and timing box in order to synchronize the light output with the camera exposure. To control the Blackfly camera, a custom control box was designed to split the camera control signals. The "optical out" line is connected to the oscilloscope where the exposure time wave can be visualized. The timing box sends a trigger signal to the "optical in" line. Because the camera has its own internal delay, the rising edge of the camera waveform is set a few milliseconds before that of the LED. For this setup, two 100 mm FL lenses are placed in the light path, one before the test section to expand the beam and one after to refocus the beam. A knife edge was placed at the focal plane of the receiving lens in order to block the deflected light rays. The camera captured the image with a 35 mm or 50 mm FL imaging lens. Right before rig testing, the focus at the injection

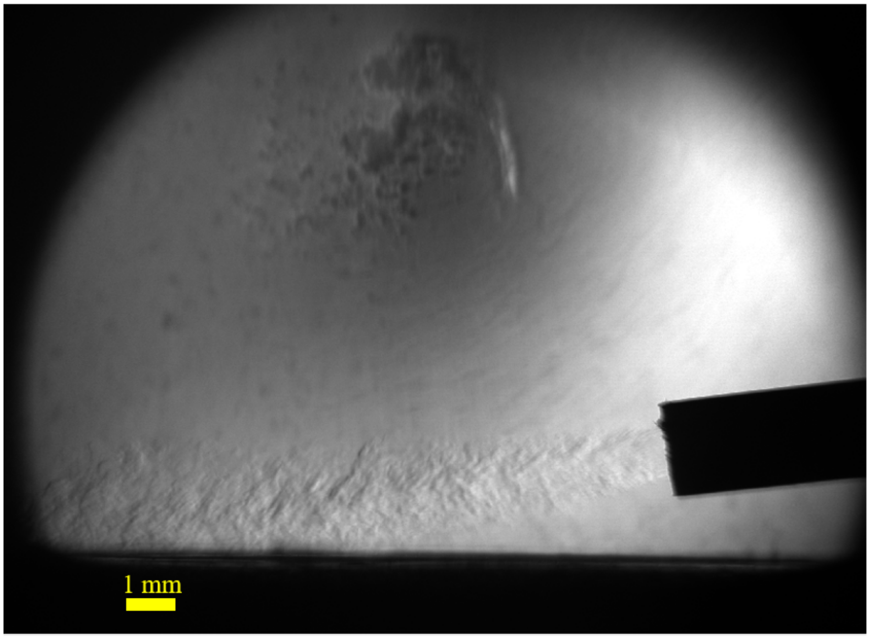

Figure 4.1: Example schlieren image of a compressed gas nozzle placed at the jet injection imaging plane. The density difference is visualized on the Blackfly camera.

point was tested by spraying compressed gas into the test section. This confirmed the focal point was in the correct spot and that a schlieren image was correctly displayed. One such test is shown in Figure 4.1.

After completing the experimental setup and capturing calibration images, the rig is preheated to 550 to 600 K and the gas flow velocity is increased, hitting the Mach 1.71 condition. At this condition, it is expected that a bow shock would form due to the liquid jet forming a physical barrier as well as a high-shear interface inside the flow. When the liquid jet interacts with the crossflow, the shear interface and surface tension of water cause the formation of sinusoidal waves on the windward and leeward portions of the water column. Each period of the sinusoidal effect is caused by these instabilities and can be described by the wavelength spacing. As the sinusoidal waves propagate through the water column, ligaments form and water peels off from the edges, atomizing as it progresses downstream. This enables mixing with air, which leads to combustion further downstream in reactive flows. Figure 4.2 shows these flow characteristics, specifically the bow shock, liquid column edges, and droplet breakup. This image was captured with the Blackfly

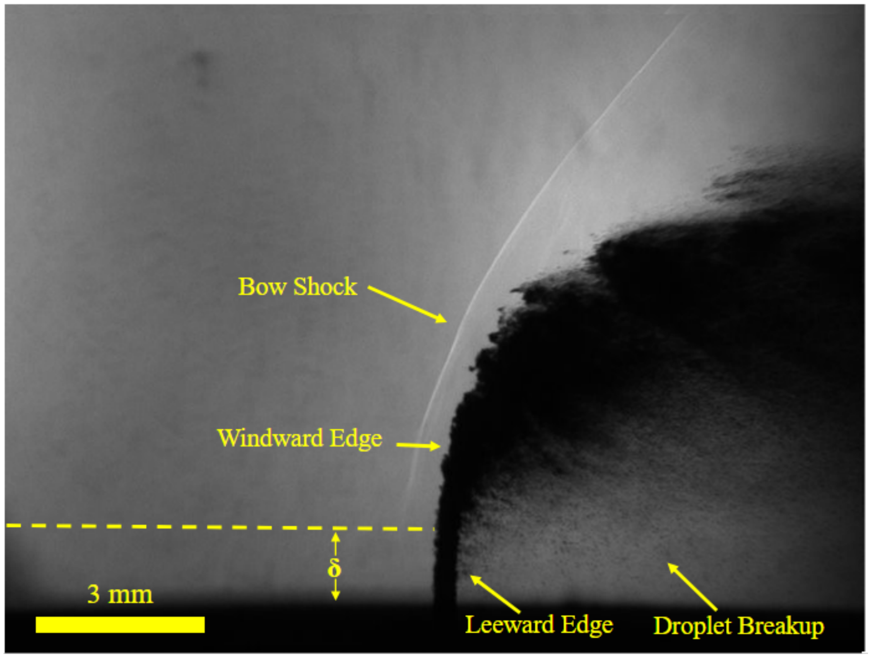

Figure 4.2: Several flow characteristics of a liquid jet in supersonic crossflow are found in an instantaneous schlieren image at J = 21.8 (300 psi) for a 0.5 mm jet. The bow shock, water column edges, and droplet breakup can clearly be seen. The particle density is the lowest near the bottom of the test section and steadily increases as y/D is increased in the vertical direction.

camera (2048 $\times$ 1536 pixels) that is gated with a pulsed white LED.

For the schlieren study, experiments were carried out with momentum flux ratios ranging from J = 7.3 to 36.3 (100 to 500 psi) for the 0.5 mm jet to observe the effect of the increase in penetration depth and the decrease in droplet field density. Additionally, a 2 mm diameter injector was also measured in order to examine the relative difference in droplet density. Figure 4.3 depicts the penetration of a 200 psi jet with an injector diameter of 2 mm. This image clearly shows that no light can penetrate the dense droplet field, depicted by the large black area behind the jet. Thus, the 2 mm diameter injector was replaced with a 0.5 mm jet for droplet breakup analysis.

Figure 4.4 shows a series of four schlieren images at the same crossflow conditions, illustrating the difference between momentum flux ratios for a 0.5 mm jet. Notice how the jet bends earlier in the J = 7.3 case than in the subsequent images. Because of this, it is determined that the droplet field is much denser near the floor of the combustor for

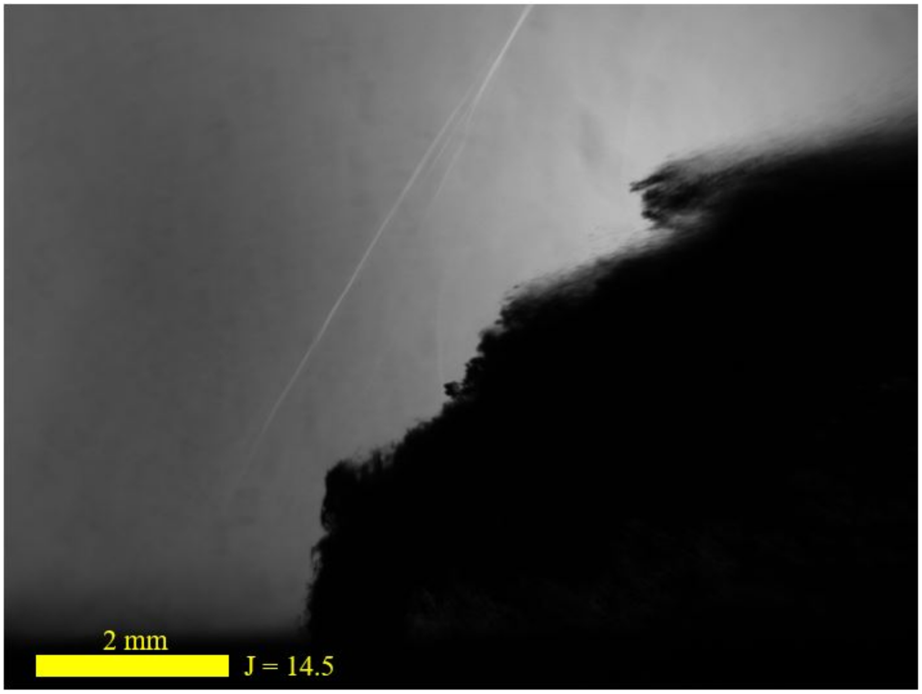

Figure 4.3: A schlieren image of water injection at J = 14.5 (200 psi) is shown for a 2 mm jet. The entire area behind the jet is dark, meaning no light is able to penetrate through the dense flow field. No droplet statistics could be analyzed in this case, so the 0.5 mm diameter injector is used in DIH droplet experiments.

the J = 7.3 case than for cases with higher momentum flux ratios. In this work, schlieren enabled the identification of typical supersonic JICF features while spatially characterizing additional features particular to liquid injection. It also proved to be useful for picking locations of low particle density in the flow field for further DIH measurements.

4.2 Digital Inline Holography

In this section, DIH is used to observe the windward side of the jet. A 532 nm continuous wave Photonics Industries laser was chosen to provide coherent light for analyzing the semi-transparent flow field. The laser beam is directed to the wind tunnel through several directional mirrors and spatially expanded through a beam expander. The beam expander has a dial that controls the divergence/convergence of the laser beam, which is calibrated using a shear plate. A high-speed Shimadzu HPV-X2 camera running at a frequency of

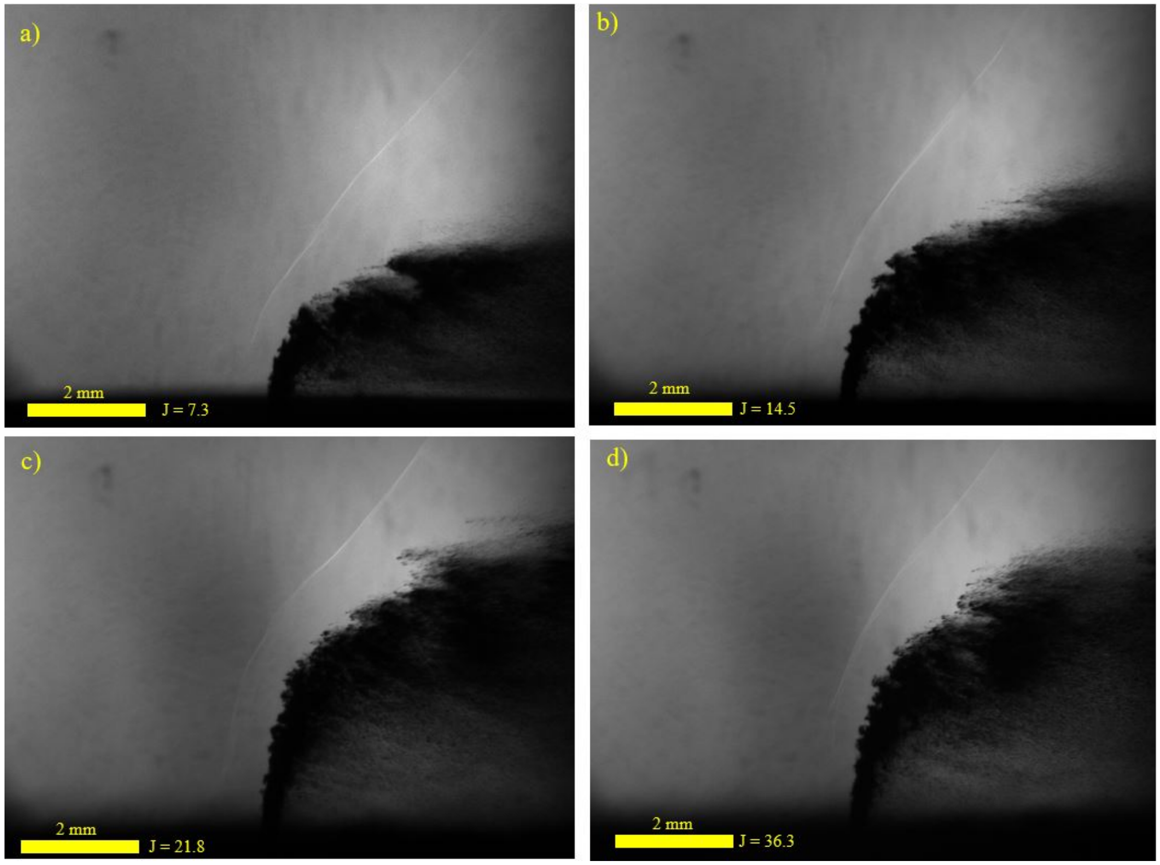

Figure 4.4: Four momentum flux ratios for a 0.5 mm diameter jet are displayed here. It is clear that moving from (a) to (d), the momentum flux ratio increases and the local penetration depth for each x/D increases with it. The jet column bends later and the droplet field density decreases near the bottom of the test section as the momentum flux ratio increases.

5 MHz (400×250 pixels, 110 ns exposure) is attached to a K2 long-distance microscope with a CF-3 ($3.56\times$ to $2.29\times$) or CF-4 ($6.1\times$ to $4.57\times$) objective. Before running an experiment, the desired magnification is selected and two dot grids of 1 mm or 125 μm spacing between dots are placed in front of the lens. The laser light is unshuttered and passes through the dot grid into the CCD of the camera. Initially, the dots are unfocused, but because the camera system is on a rail, the camera position can be adjusted until the focus is reached. Coherent images of the grids are displayed in Figure 4.5 for a CF-4 objective.

Because the physical spacing is known for the dot grid, a scale bar can be developed and the total vertical distance of the image is found to be approximately 2.875 mm for

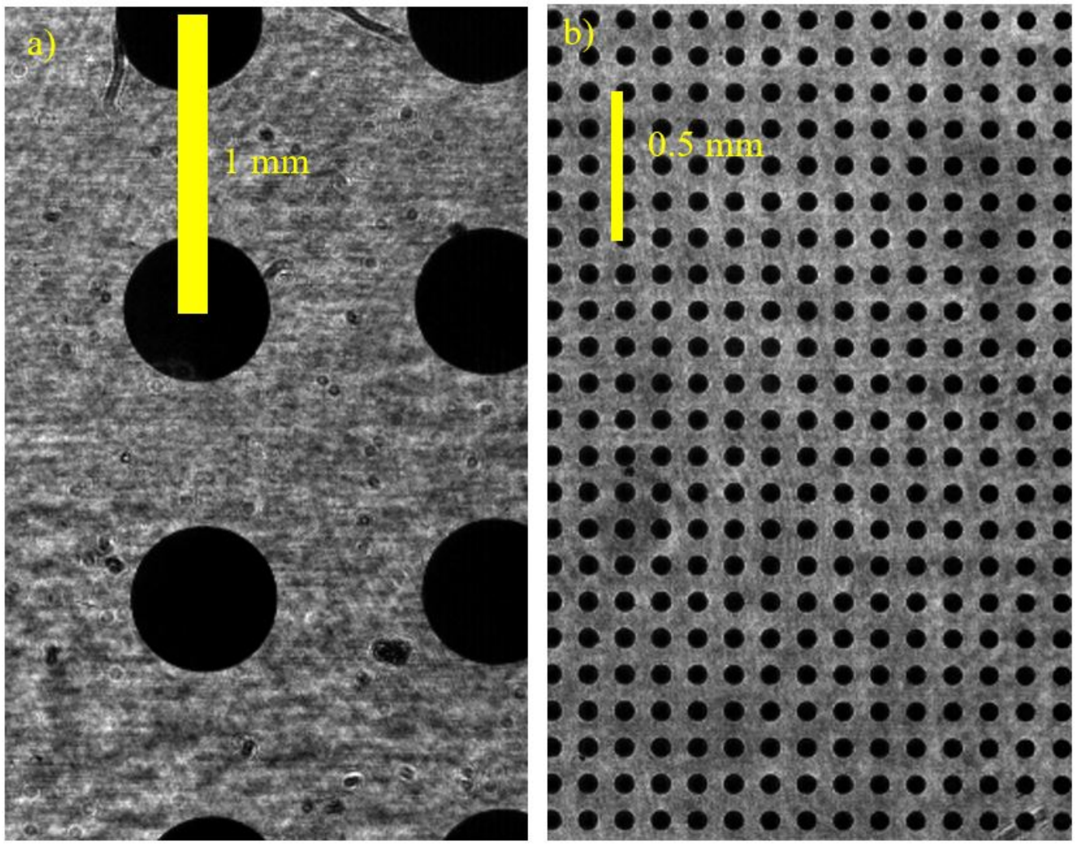

Figure 4.5: Two dot grids are used to calibrate the spatial distance on the CCD prior to running DIH experiments. (a) An image with 1 mm spacing between the center of the dots and (b) an image with 125 μm spacing between successive dot centers are shown. The calibration accuracy is increased when using the smaller spacing dot grid.

this configuration. The horizontal distance of this particular configuration is calculated to be approximately 1.80 mm. The pixel resolution, in this case, is 7.14×10^{-6} m/pixel. In the numerical refocusing code, this resolution is used as the Δx and Δy step sizes. With a collimated laser beam, the imaging resolution does not change when the image is numerically refocused. After calibrating the images, the camera is slid back into position with the image plane placed either in the jet plane (for coherent imagining) or just outside the jet plane (for DIH). Data is then collected to visualize flow characteristics such as the penetration depth (h/d), instability spacing, and front-edge droplet breakup.

A series of coherent images for momentum flux ratios of J = 7.3 to 36.3 are shown in

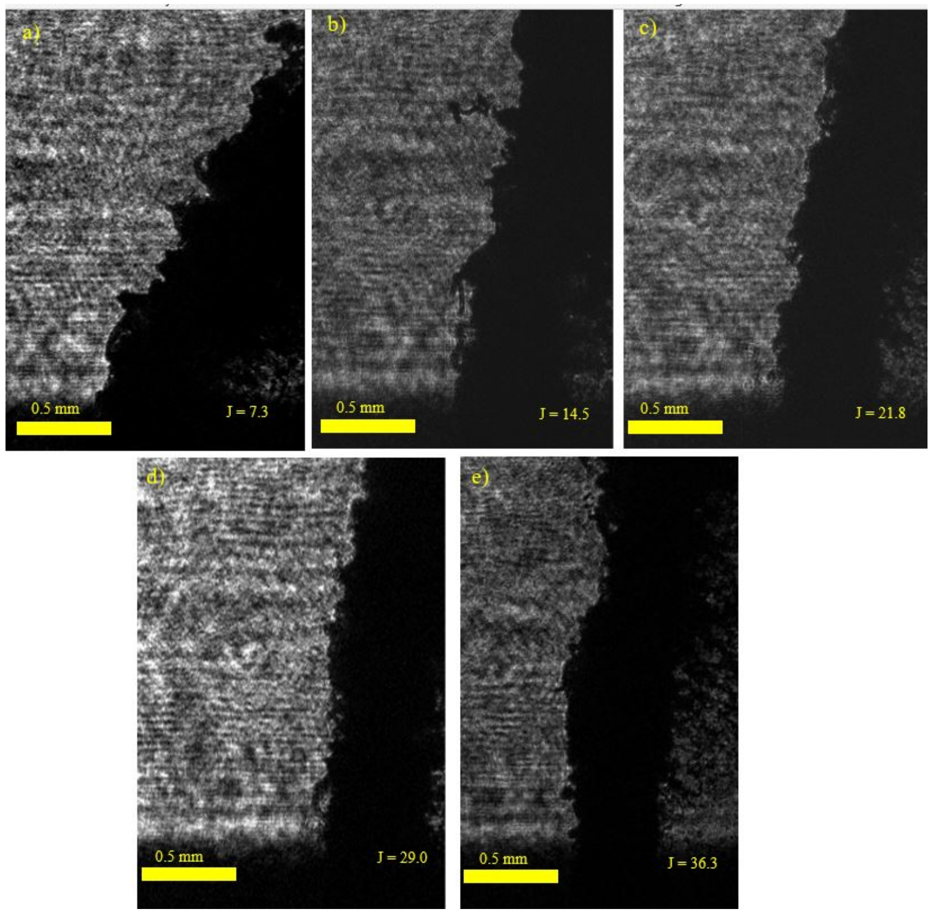

Figure 4.6: Coherent images at the focal plane are displayed for all five momentum flux ratios from (a) to (e) corresponding to J = 7.3 to 36.3 (100 to 500 psi). As the momentum flux ratio is increased, the jet becomes more straight.

Figure 4.6, captured with the CF-4 objective. Visually, it is clear that increasing the momentum flux ratio directly affects flow characteristics, especially how the water jet bends. When the crossflow air mass flow rate is held near constant for these experiments, the increase in liquid flow rate for the jet will coincide with an increase in penetration depth. When the jet bends heavily at low momentum flux ratios, the amount of instability mixing is decreased. For engine applications, it is therefore advantageous to increase the momentum flux ratio. However, if the momentum flux ratio is increased, this would also result in more fuel being used for combustion inside the vehicle. Thus, understanding jet penetration can help engineers optimize mixing and fuel use.

4.2.1 Penetration Depth

In this section, DIH and coherent imaging with a Shimadzu HPV-X2 (5 MHz, 110 ns exposure) and CF-4 objective are used to quantify the penetration depth for different momentum flux ratios. Figure 4.7 shows a custom edge tracing code designed for extracting penetration depth data applied to a J = 7.3 jet. The binarization process and contrast filtering allow the precise edge to be recorded while matrix operations are used to extract edge information.

In this example, an instantaneous shot is obtained in the flow field. However, for a series of frames, some variation in edge oscillation is expected as the jet is unstable and instabilities tend to propagate downstream. In this case with J = 7.3 and x/D = 0.35, all 128 frames of the 0.5 mm diameter jet were analyzed and the mean penetration depth was estimated at h/D = 0.83 or 1.66 D. However, the instantaneous vertical spray penetration depth is found to vary slightly from 1.00 D to 2.90 D. For comparison, a similar study with the same momentum flux ratio at x/D = 1.78 was done to analyze downstream penetration depth effects. This investigation yielded an oscillation of 3.50 D to 4.72 D, centered around a mean of 3.88 D.

After the penetration depths for every pressure are tabulated, a comparison to existing depth correlations in the literature can be made. Many researchers in the supersonic JICF use different optical techniques like PIV and shadowgraphy to develop constants for curve fits. Curve fitting software can extract the constants for different functional forms, but these constants tend to be very specific to the experimental apparatus and setup. The constants can vary with the length of the test section, crossflow temperature, and Mach numbers of the fluids. A table of several curve fits from the literature are delineated in Table 4.1, corresponding to the functions outlined in section 1.2.

Of the seven listed curve fits, only four are chosen to examine in more detail. These four curve fits have experimental conditions similar to those tested supersonic JICF rig, including similar momentum flux ratios, diameters, and L/D ratios. The fit that seems to best approximate the experimental data from this work is the one defined by Inamura et al.

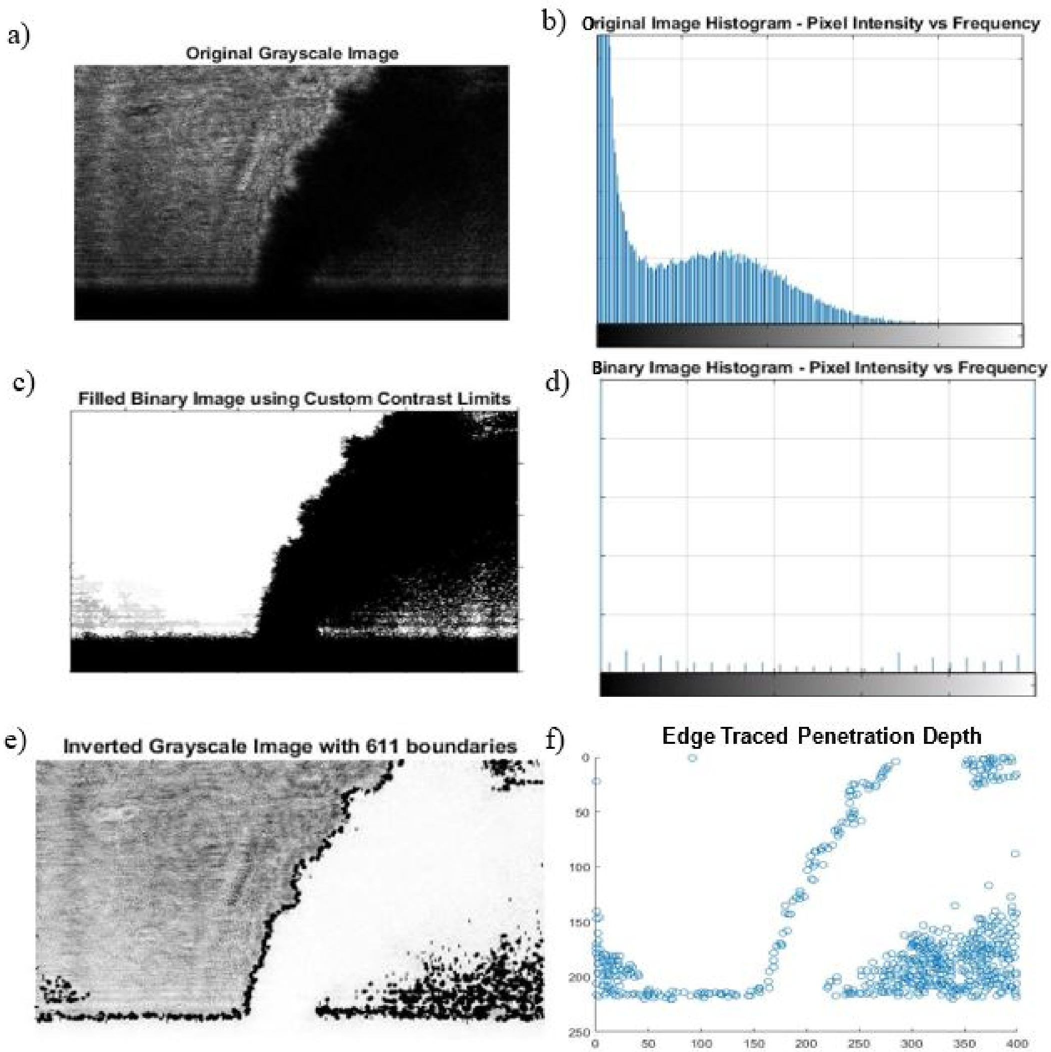

Figure 4.7: The process for tracing the edge of a DIH image and extracting the penetration depth is shown. (a) The original out-of-focus DIH image and (b) map of the pixel intensities are first obtained. (c) Contrast limits are then applied to define the edge. (d) The pixel intensity map is then extracted after the contrast limits are changed. (e) The edge is traced after an region of interest (ROI) is applied and then (f) the points are extracted. Droplets are clearly being traced, as well as the floor boundary, so these are removed, leaving only information on the front edge instabilities.

(1991), as all the flow parameters coincide closely with the conditions in this work. Other tested fits tested include Kim et al. (2012), Wu et al. (1997), and Rothesein & Wartuck (1992) [21]. Figure 4.8 through Figure 4.12 show the expected penetration depth from using each of these curves to the mean of the measured data.

Table 4.1: List of experimental supersonic curve fits for penetration depth.

Penetration Depth Data	Exp. / Sim.	Parameters	Empirical Constants
Ghenai et al. (2009)	Experimental	Ma = 1.5 , J = 0.35 - 1.44 , x/D < 28	A = 3.88, α = 0.4, b = 0.2
Lin et al. (2004)	Experimental	Ma = 1.94, d = 0.5 & 1.0 mm, T = 477 - 533K, J = 2-15	A = 4.73, α = 0.30, b = 0.30
Kim et al. (2012)	Experimental	d = 1.0, 1.8 &, 2.1 mm, T = 500K, J = 2.0 - 29.1 , We ~ 5.3 - 47.9, L/d > 10	A = 2.241, α = 0.402, b = 0.410
Inamura et al. (1991)	Experimental	Velocity Ratio ~ 2 - 20, d = 0.5, 1.0, & 2.0 mm, x /D < 15	A = (1.18 + 0.24d), α = 0.36, β = (1.56 + 0.48d)
Wu et al. (1997)	Experimental	d = 0.5 - 1.5 mm, J = 0.5 - 12, x/D = 0 - 200, We ~ 55 - 647	A = 3.17, α = 0.33, b = 0.4
Rothstein & Wantuck (1992)	Experimental	Ma = 1.5, J = 5.9 - 38.6	A = 2.173, α = 0.276, b = 0.281
Sun and Hu (2018)	Simulation	Ma = 2.7, J = 1.85 & 5.5	A = 2.933, α = 0.161, b = 0.256

As seen in these figures, the predicted h/D from the curve fits and the experimental h/D are plotted against each other for all five momentum flux ratios corresponding to injection pressures of 100, 200, 300, 400, and 500 psi. If the points fall on the 45-degree line, then the predicted h/D from the correlations fit perfectly with the experimental data. These results show that the Inamura fit consistently fits the experimental data better for all pressures and contained a mean absolute error (MAE) of h/D of only 0.308 for J = 7.3, 0.229 for J = 14.5, 0.236 for J = 21.8, 0.308 for J = 29.0, and 1.19 for J = 36.3. MAE is a measure of the weighted average penetration depth distance needed to close the gap between the 45-degree line and the plotted points, given by the equation,

$$MAE = \frac{\sum_{i=1}^{n} |y_{predicted} - y_{actual}|}{n}. \tag{4.1}$$

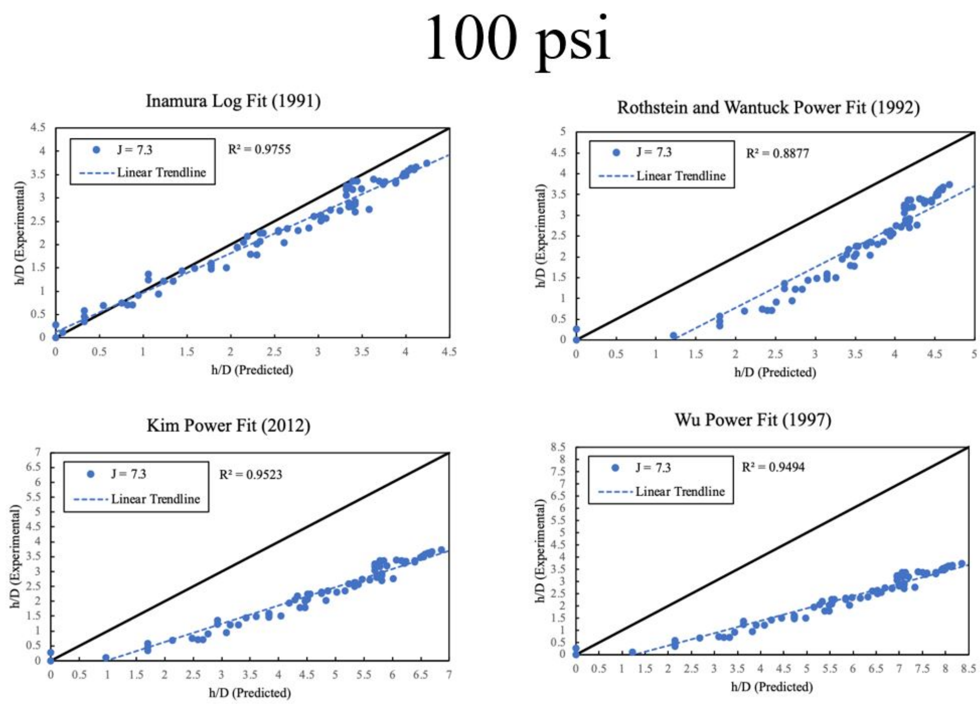

Figure 4.8: All four tested fits for the penetration depth of J = 7.3 (100 psi) are shown in this figure. The best fit for the experimental conditions is the Inamura fit for x/D < 9.

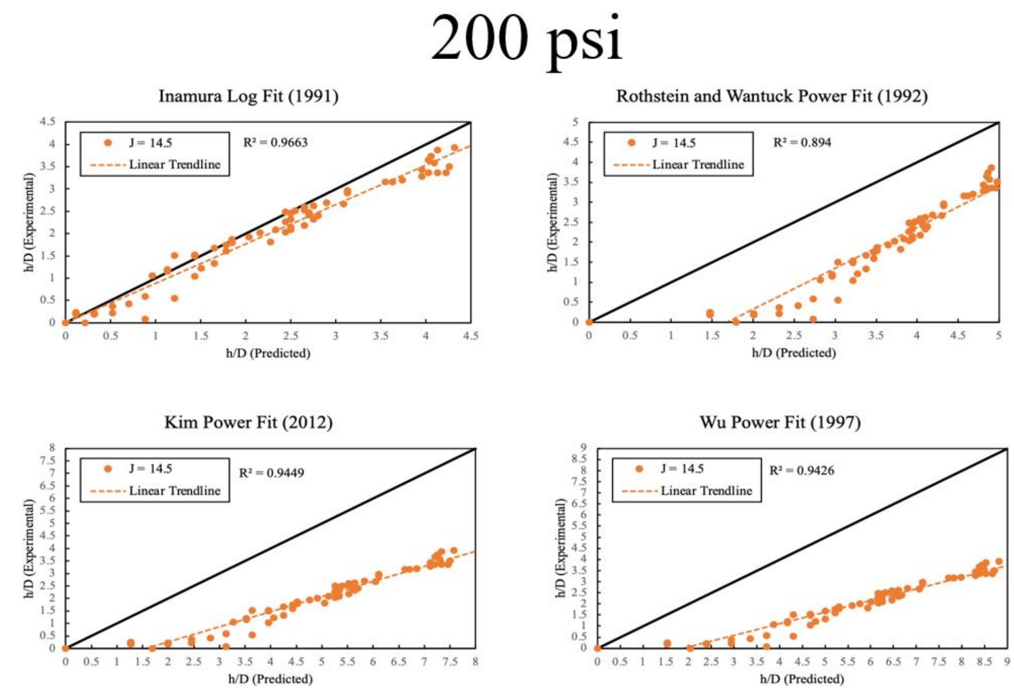

Figure 4.9: All four tested fits for the penetration depth of J = 14.5 (200 psi) are shown in this figure. The best fit for the experimental conditions is the Inamura fit for x/D < 9.

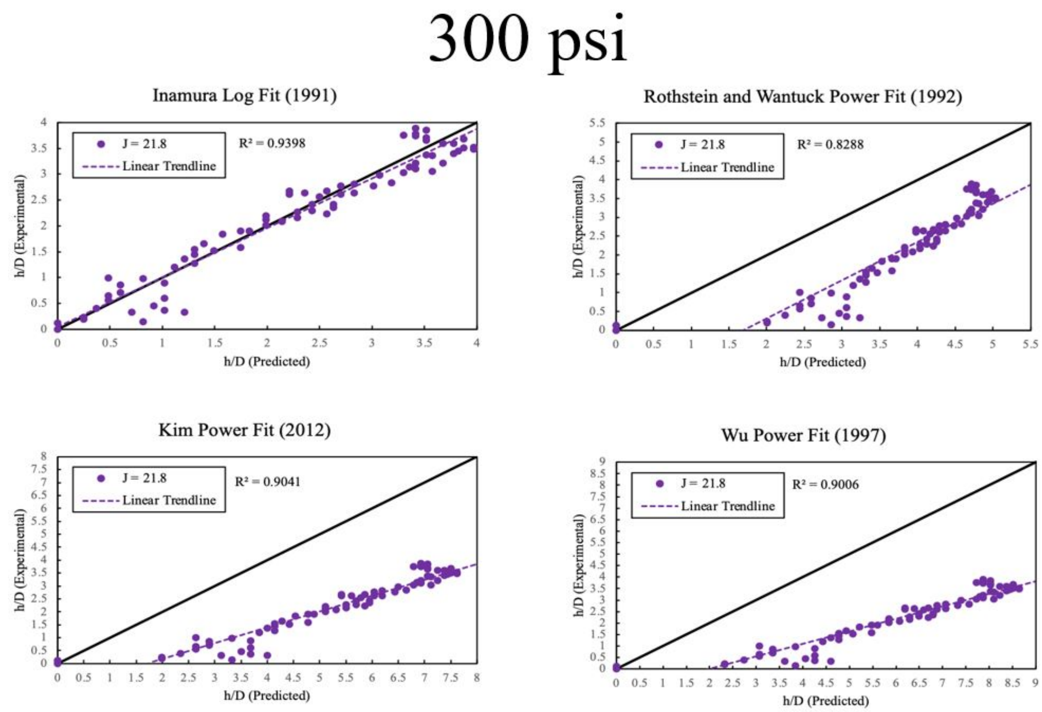

Figure 4.10: All four tested fits for the penetration depth of J = 21.8 (300 psi) are shown in this figure. The best fit for the experimental conditions is the Inamura fit for x/D < 9.

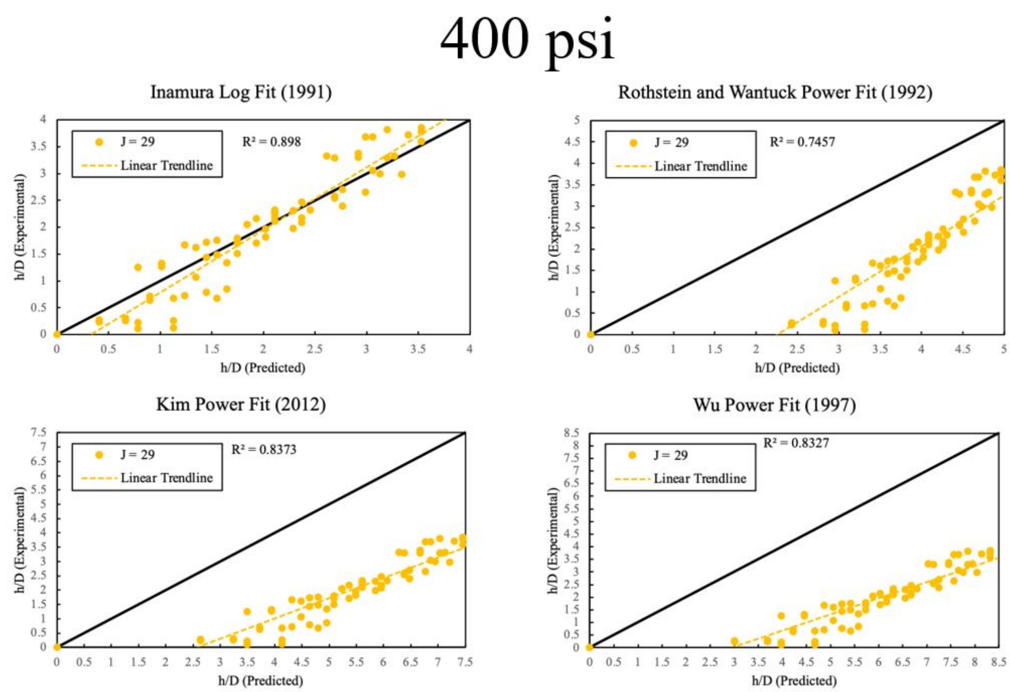

Figure 4.11: All four tested fits for the penetration depth of J = 29 (400 psi) are shown in this figure. The best fit for the experimental conditions is the Inamura fit for x/D < 9.

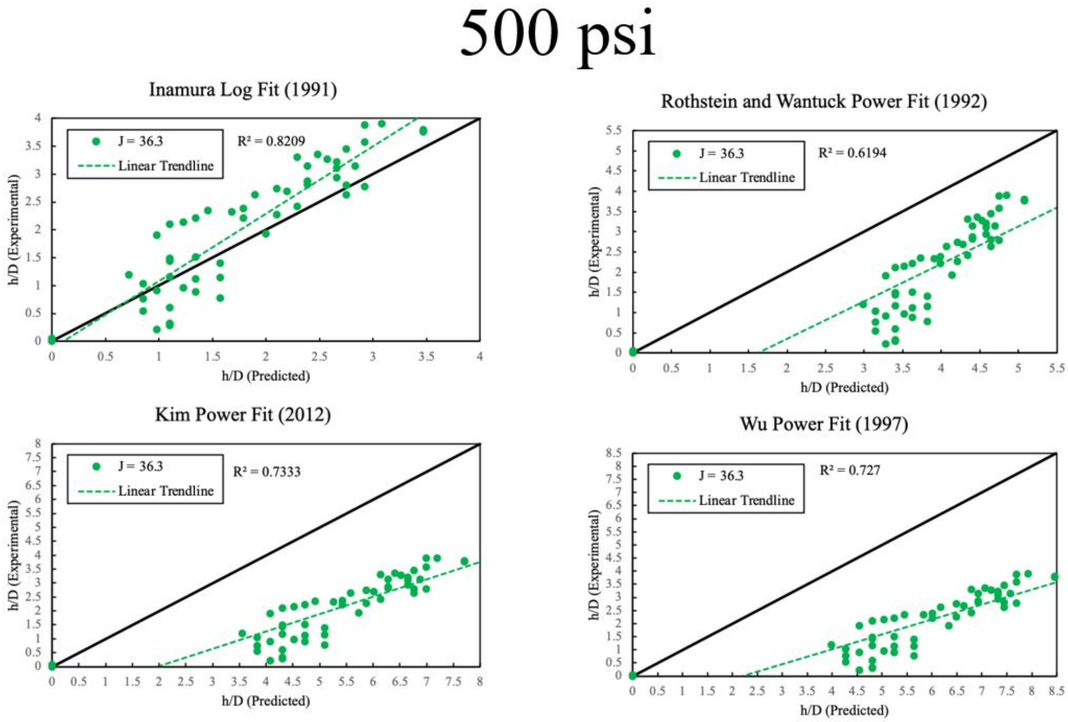

Figure 4.12: All four tested fits for the penetration depth of J = 36.3 (500 psi) are shown in this figure. The best fit for the experimental conditions is the Inamura fit for x/D < 9.

The results from comparing the experimental data with the Inamura fit all correspond to a difference of less than 0.6 mm. While this is not perfect, for these conditions over the tested x/D, it is not extremely divergent, like the rest of the fits. All the experimental penetration depths were plotted and compared to the Inamura fit in Figure 4.13. This figure shows that the error between the experimental and predicted is relatively small for each pressure. For a small x/D, each experimental mean curve matches well against the predicted curve fits from Inamura. Overall, the Inamura fit over-predicts the penetration depth slightly for small momentum flux ratios and under-predicts the penetration depth slightly for large momentum flux ratios.

Figure 4.14 places all the injection pressure data points together in one graph with the Inamura fit to show the deviation from the 45-degree angle. The next step here would be to fit a curve based on these mean penetration depths that further reduces the error.

These results have several applications for supersonic air-breathing vehicles. For a

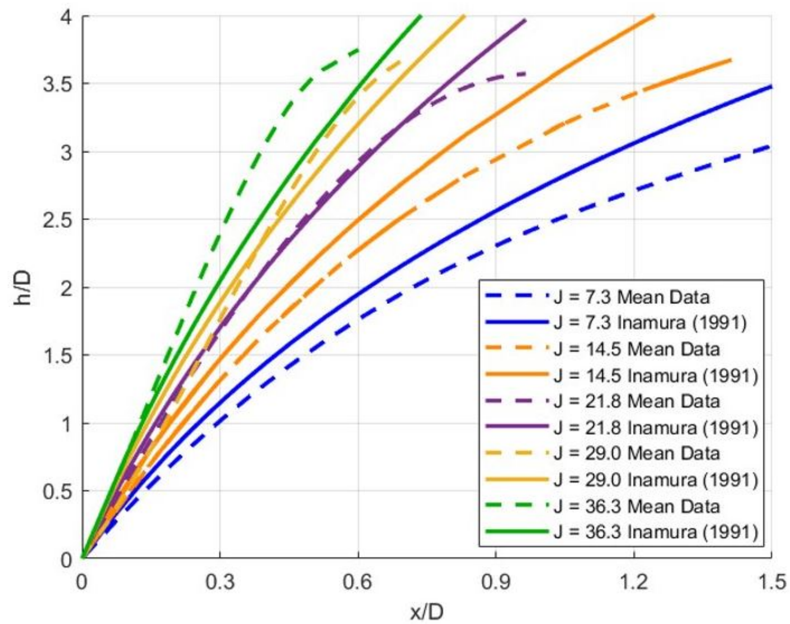

Figure 4.13: Experimental penetration depth curves as a function of x/D are compared to the predicted Inamura (1991) curve fits. All tested momentum flux ratios from J = 7.3 to J = 36.3 are displayed.

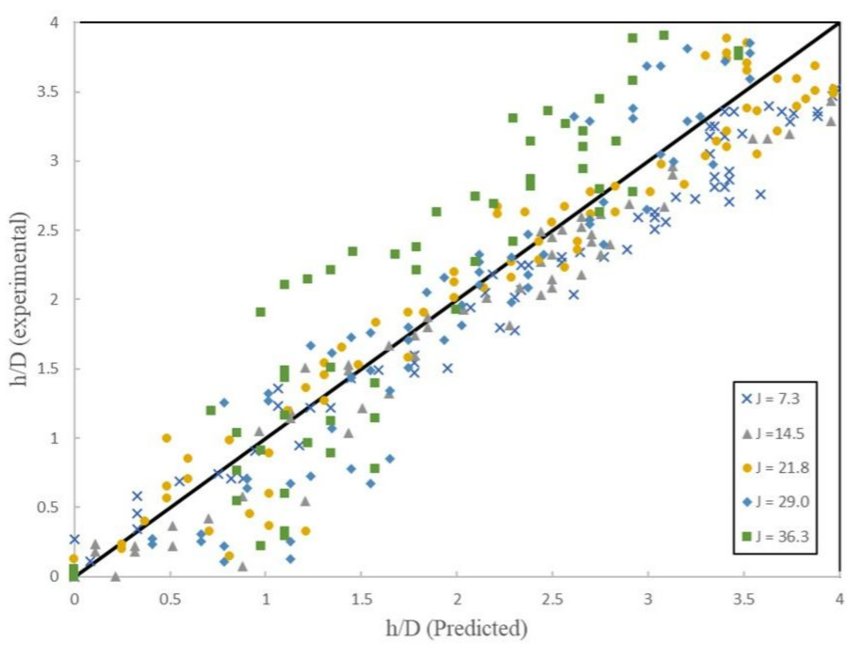

Figure 4.14: All experimental penetration depths are correlated to the expected depth from the Inamura (1991) fit. All tested momentum flux ratios from J = 7.3 to J = 36.3 are displayed.

controlled time period, a deeper penetration depth will expel more fuel than a shallower penetration depth, which is can be desirable for high fuel to air ratios. An example of this is when a scramjet is launching rather than cruising. Moreover, because the liquid column begins shedding droplets at a higher depth, there is more fuel per unit area higher in the plume, making the flow field much denser high in the plume but less dense lower in the plume. This study demonstrates that DIH paired with an edge tracing data processing tool is a viable and non-intrusive method to quantify the penetration depth. Many other techniques require complicated setups, the introduction of particles, and/or the introduction of dyes to capture this information. Thus, this work shows how penetration depth can be estimated using DIH methods.

4.2.2 Holography Numerical Refocusing Discussion

Numerical refocusing is an important component of the DIH technique that enables the focal point to be moved in post-processing. This technique will be used later for studying the front-edge and downstream droplets. However, it is also used to estimate the bow shock location. To demonstrate this, Figure 4.15 displays refocusing to two areas of interest: the front-edge and the bow shock using a CF-3 objective on the Shimadzu HPV-X2 camera. The stagnation temperature and pressure for this experiment are 543 K and 28 psi, respectively. The injected water temperature is a constant 293 K. After the images are taken, the focal depth (z) is increased. This results in the focal point moving closer to the centerline of the liquid jet, allowing the structures to come into focus. In this case, the horizontal and vertical pixel resolutions are 1.81×10^{-5} m/pixel, which is used to calibrate the numerical refocusing code. The horizontal field-of-view is 7.5 mm and the vertical field-of-view is 4.5 mm. These results show that DIH can be used to refocus to both the bow shock and the liquid jet edge, which occur in different focal planes. Note that because the bow shock is a phase object, its focal plane tends to be different from its physical location, but only typically offset by a few millimeters [62]. However, it should also be noted that the bow

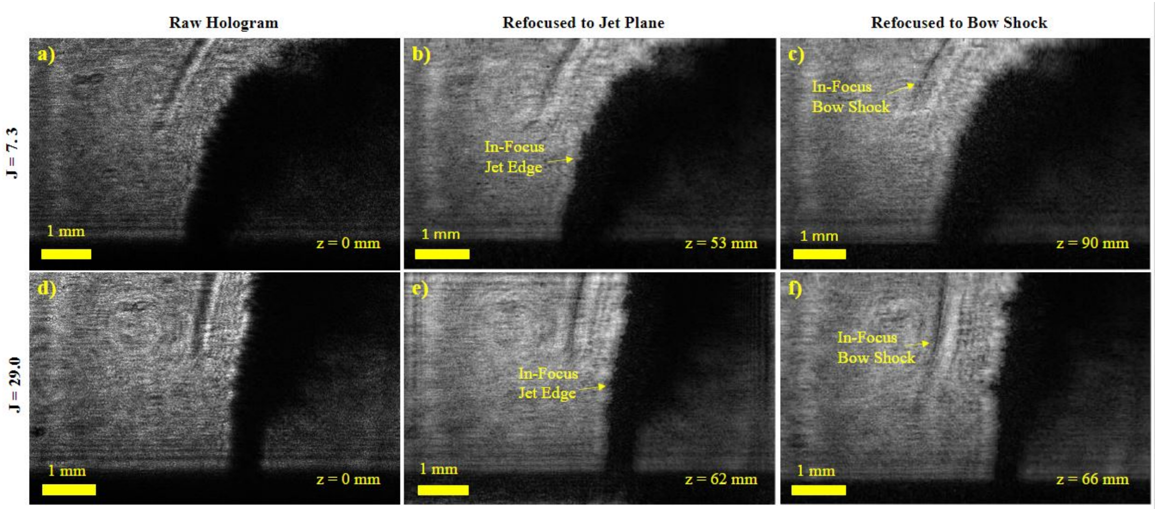

Figure 4.15: DIH images of the jet and bow shock for the J = 7.3 (100 psi) case show (a) the raw data, (b) refocused hologram to the jet focal plane, and (c) refocused hologram to the bow shock focal plane. DIH images of the jet and bow shock for J = 29 (400 psi) case show (a) the raw data, (b) refocused hologram to the jet focal plane, (c) and refocused hologram to the bow shock focal plane.

shock tends to move over time and the sharpest transition point for the bow shock may occur at a plane different from the liquid jet. This can be clearly noted by the difference between the focal planes for the jet in the two example cases outlined in Figure 4.15.

4.2.3 Instability Spacing and Trends

R-T instabilities and K-H instabilities are present in both liquid-gas and gas-gas supersonic JICF. In gas-gas experiments, the density ratio is low, so R-T instabilities are not as dominant as in liquid-gas cases. Because the density ratio of the water to air at the test conditions is 2152, more R-T-driven instabilities are expected within this regime. Additionally, the K-H instabilities occur at a shear interface where one fluid has a much higher velocity than the other. For these experiments, the free-stream velocity ranges from approximately 640 to 668 m/s at 550 K to 600 K while the water jet velocity ranges from about 37 to 83 m/s at 100 to 500 psi. Ignoring the difference in direction, the maximum velocity ratio between the incoming gas and injected liquid is $\sim$18 and the lowest is $\sim$8. This considerable velocity difference should lead to the intense formation of K-H instabilities. Thus, it is expected that both instabilities exist in this regime. It is also important to note, however, that some of the front-edge oscillations can be driven by the initial conditions in the jet. Thus capillary effects and turbulence inside the jet nozzle can also contribute to the initiation of instabilities inside the jet. Overall, the front edge instabilities are important to characterize because they control ligament and droplet breakup at the front of the jet, which can control droplet sizes further downstream.

To characterize the windward instabilities and relate them to droplet breakup parameters for scramjet combustion, a method to determine the wavelength of each successive instability peak is devised. Fundamentally, the instabilities can be modeled as a sum of sinusoidal functions with successive peaks and troughs. Figure 4.16 shows and example that has a dominant breakup wavelength.

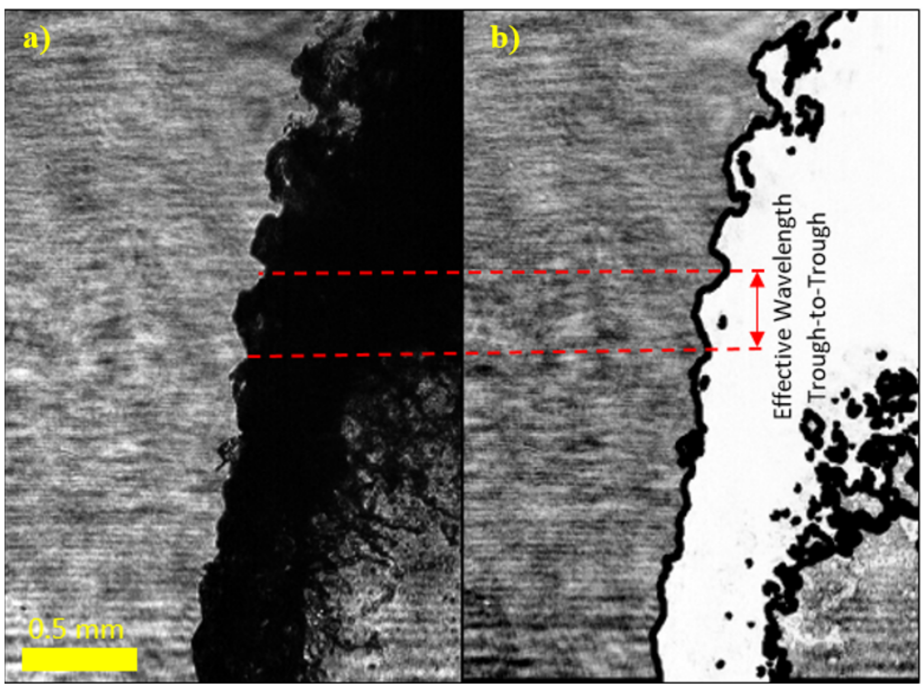

Figure 4.16: The method for estimating the windward instabilities is shown for a J = 7.3 jet. (a) The raw coherent image and (b) the edge-traced image are illustrated.

Here, the wavelength is defined as one trough-to-through distance. Using a set of 128 coherent imaging frames acquired at 5 MHz, the surface wavelengths of the instabilities were measured by examining the peak-to-peak or trough-to-trough spacing in a custom

MATLAB code. This is plotted as a probability distribution (PDF) for each injected pressure, as shown in Figure 4.17. For each PDF, 80 to 100 individual waves were identified. A kernel distribution was assumed and fit to the distributions for comparison. The kernel distribution used here is a smoothing function used to fit a PDF to the actual data without assuming the shape of the graph. Thus, using this function avoids pre-emptive assumptions regarding the underlying distribution shape.

Looking at this data, it is clear that the wavelength spacing of the instabilities on the windward side consistently decreases as the penetration pressure increases. The spacing for the peak wavelength of each pressure for J = 7.3, 14.5, 21.8, 29, and 36.3 (100, 200, 300, 400, and 500 psi) are 104.5, 102.5, 88.4, 74.4, and 68.3 mum, respectively. The greatest difference is between 200 and 300 psi, at 14.1 $\mu\mathrm{m}$, while the other points are more tightly grouped. There are several factors that could lead to the decrement of the spacing as the pressure increases. One important factor is surface tension forces, which can lead to grouping within the R-T and K-H wavefront. The liquid entry conditions, governed by the L/D ratio and roughness factor, can also affect the propagation of the instabilities. More investigation is needed to understand the driving forces behind this effect but these findings can help improve mixing forecasting in models, since the smaller the spacing, the more fluid mixing occurs. Better fluid mixing and entrainment can lead to a more steady power output of the engine, which is beneficial for vehicle operation.

Another interesting feature in these graphs is the secondary peak on the 100 psi case at around 275 $\mu\mathrm{m}$. This feature is likely due to the jet bend and breakup from ligament shearing for this low water jet pressure condition. The height of the image is restricted for the cases between J = 14.5 and 36.3 (200 and 500 psi), likely obscuring the second peak in those other cases. Additional investigation is needed to characterize this effect higher in the flow for the higher water injection pressures. Another important note to mention is that there are wavelengths present in the flow outside of the dominant trough-to-trough spacing. In order to analyze these wavelengths, additional work is needed in the future to look at the

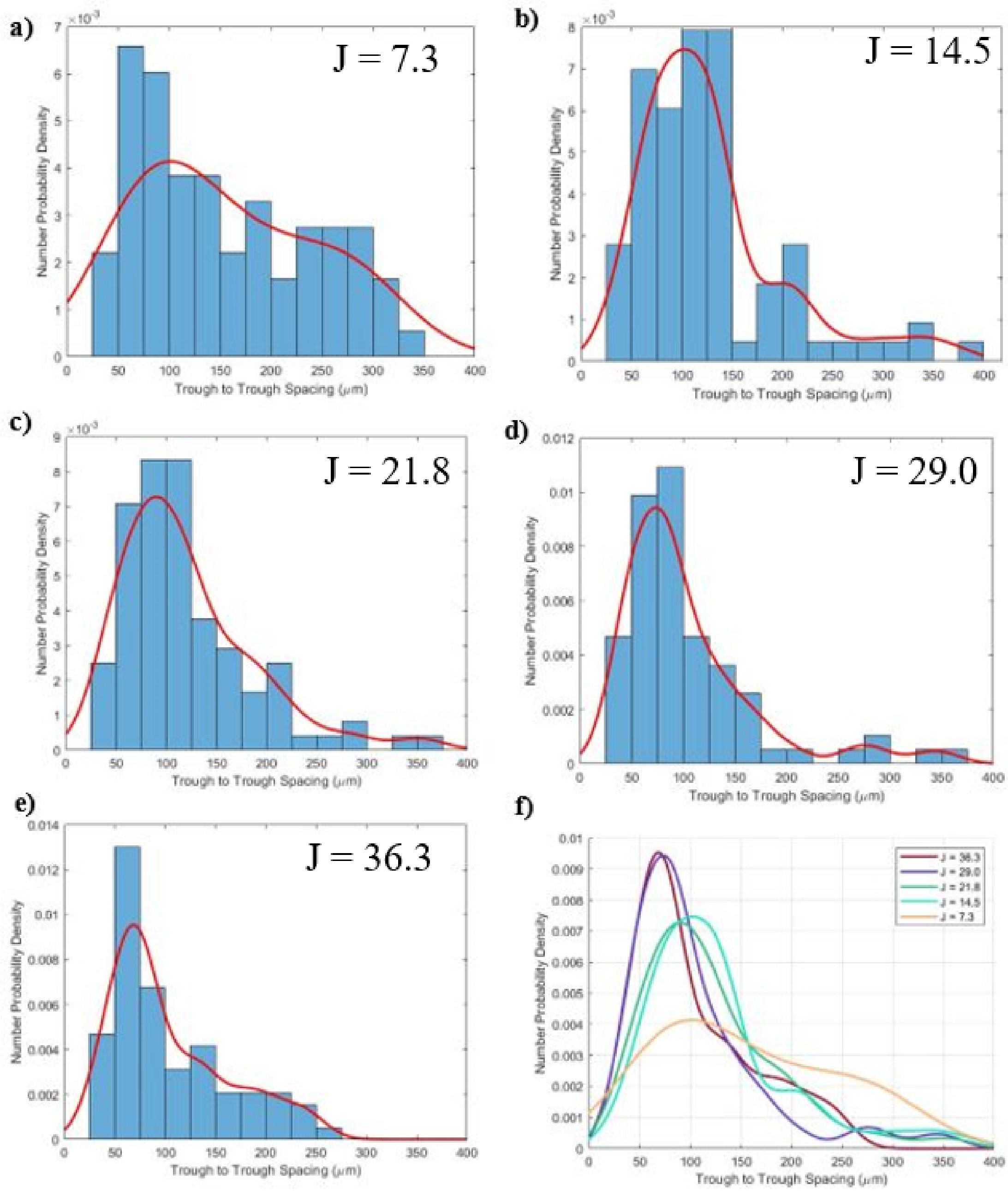

Figure 4.17: Instability spacing probability distributions show the frequency of appearance for different trough to trough spacings. The distributions for (a) J = 7.3 (100 psi), (b) J = 14.5 (200 psi), (c) J = 21.8 (300 psi), (d) J = 29 (400 psi), and (e) J = 36.3 (500 psi) are shown. (f) The overlayed normalization of all cases is also illustrated. The results show that the instability spacing decreases as the water injection pressure increase, creating an inverse relationship.

Fourier transform of the front-edge data.

4.2.4 Front-Edge Droplet Breakup

One interesting and novel finding from these supersonic JICF experiments is droplet breakup at the front-edge of the jet near the bottom of the test section for the 2.0 mm diameter jet. The holography setup used to capture this data includes the Photonics Industries CW 532 nm laser, Shimadzu HPV-X2 camera, K2 distamax microscope, and CF-4 objective lens. The original objective of the experiment was to measure the front-edge instabilities with both coherent imaging and out-of-focus DIH imaging. However, when injecting with the 2.0 mm jet, a new front-edge phenomenon was found. Interestingly, droplets in this environment were found spewing off the edge heading towards the bottom of the test section. A potential reason for this is interaction with the recirculation zone that forms ahead of the jet. The oscillatory motion of the bow shock and accompanying boundary layer interaction may also affect the behavior of the front-edge breakup. Additionally, when more liquid mass per unit area is contained in the column, liquid breakup near the front of the jet could also be enhanced. As this effect has not been discussed in literature, it is currently unknown what mechanisms contribute to this effect and why exactly the phenomenon only occurs at higher-diameter jets.

For these experiments, the 0.5 mm diameter injector was replaced by the 2 mm diameter injector. The magnification of the CF-4 in this setup was $6.1\times$ to $4.57\times$. Using a higher magnification lens is paramount for visualizing the individual droplets as they breakup right at the injection point. Figure 4.18 shows that, for the jet diameter of 2 mm injected at J = 14.5 (200 psi), front-edge breakup indeed occurs and droplets plunge toward the bottom of the test section.

Next, the velocity of the droplets are measured by examining both the u and v components, correspondig to the x and y direction velocities. Here, images were captured with the Shimadzu HPV-X2 camera with a CF-4 objective at 5 MHz and then processed with a fast Fourier transformation (FFT) window deformation algorithm within a selected region of interest (ROI). The code correlates two consecutive frames and draws a velocity vector

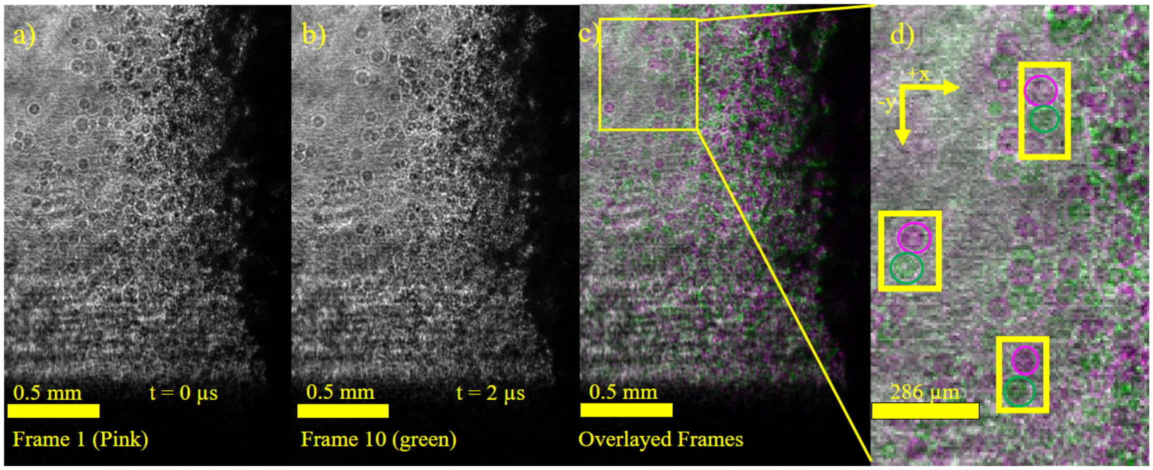

Figure 4.18: Front-edge droplet correlations are shown for a 2 mm diameter jet at J = 14.5 (200 psi). (a) The first frame corresponds to 0 μs and is shown in pink circles. (b) The 10th frame at 2 μs is shown in green circles. (c) A MATLAB comparison code is used to overlay (a) and (b) images. (d) An exploded view of (c) with boxes shows the downward movement of the droplets from frame 1 to frame 10.

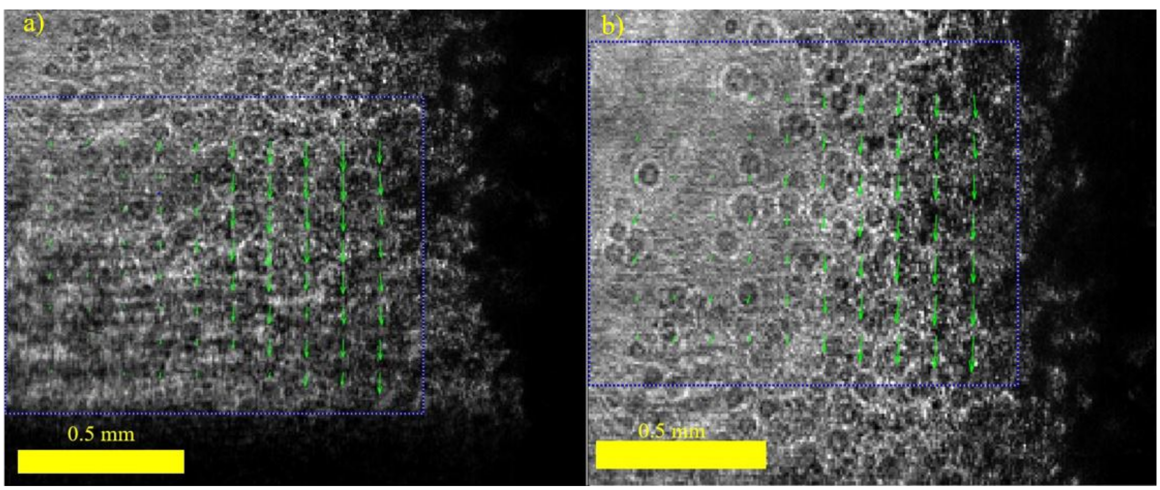

Figure 4.19: The front-edge velocity components for the 2.0 mm diameter jet at J = 14.5 are computed with a FFT window deformation code. The green arrows point in the direction of the water particle displacement from two correlated frames. A blue dotted bounding box encapsulates the analysis area. The two images here are the same frame but analyzed at (a) y/d = 2.875 for the left image and (b) y/d = 5.2 for the right image.

where a particle has translated. The resulting velocity vectors are shown in Figure 4.19 for two y/D (2.875 and 5.2) areas at the front-edge, near x/D = -2.5 to 0.

The droplets at the front-edge in these experiments are subject to vastly different conditions than those of the downstream droplets. As previously found for this facility, the

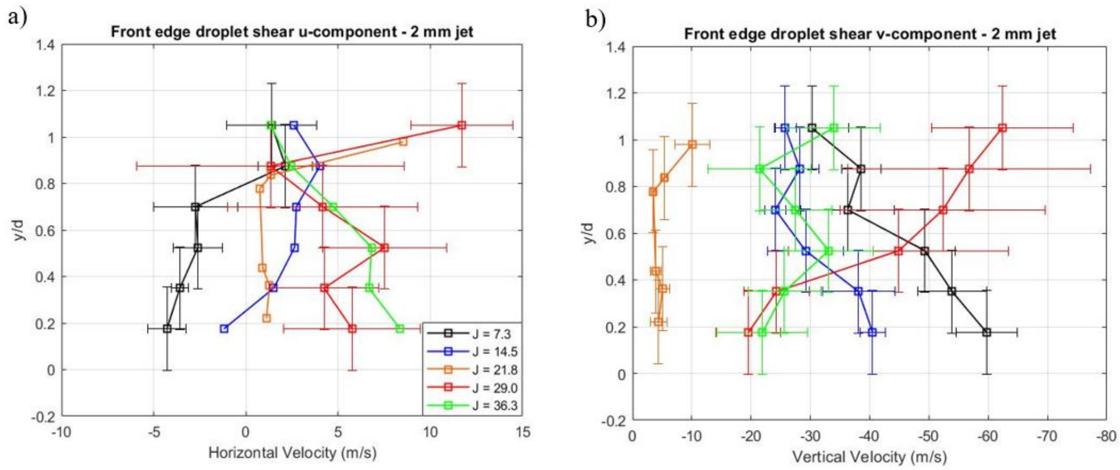

Figure 4.20: The front-edge droplet (a) u and (b) v velocity components for the 2.0 mm diameter jet is shown. There seems to be no definable trend for either the horizontal or vertical directions. The standard deviation calculated from up to approximately 10,000 velocity vectors in all 128 frames defines the uncertainty along the x-axis. The uncertainty along the y-axis is the normalized height of the regions of interest used to estimate the average.

boundary layer thickness is $\Delta_{95\%} = 5.3$ mm [37], although this value can vary slightly depending on the state of the upstream air. A thicker boundary layer has been found to augment the mixing between the vortex coupling and the instabilities on the front-edge of the jet [66], which could contribute to this effect. Another feature is that the bottom of the bow shock can intersect the layer, causing more unsteadiness and breakup.

Figure 4.20 displays the u and v components of velocities found at the windward side of the jet for the 2.0 mm diameter injector. In these experiments, the ROI was chosen to be as close to the jet as possible to eliminate any uncertainty from location estimation. Overall, droplets farther away from the front-edge (going against the streamwise velocity) tend to have a significantly higher velocity than those at the edge. However, from these graphs, there appears to be no correlation between the momentum flux ratio and the horizontal velocity. Some particles tend to move with the freestream fluid while others tend to move against the freestream, but this may be caused due to the initial particle acceleration from the breakup of the ligaments or the presence of the recirculation zone. In the y direction, it

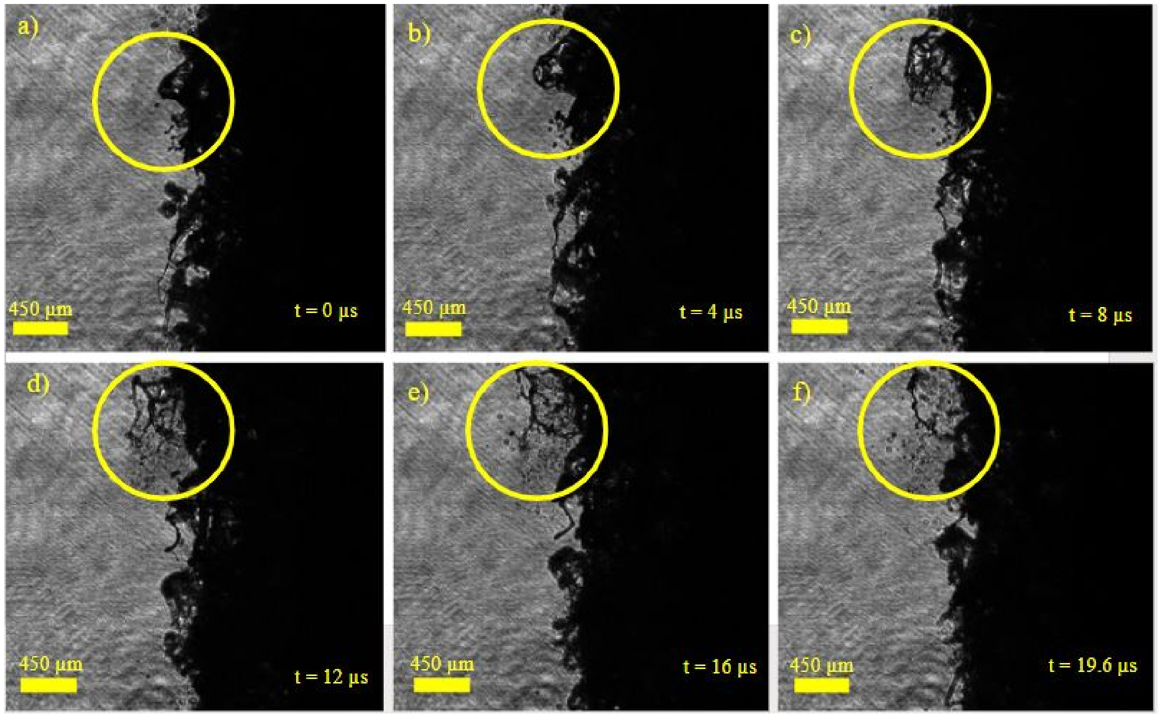

Figure 4.21: Ligament breakup for a 2.0 mm jet at J = 21.8 (300 psi) is shown. Progressing from (a) to (f), the instability is first shown, which later produces a ligament. This ligament then breaks up into a large number of small droplets.

was expected that the particles would accelerate as they fall to the ground. This occurred for some pressures and diameter jets, but for others, it did the exact opposite. It is unknown if the boundary layer plays a part in this for different diameter jets.

For the u-velocity components, the magnitudes are much lower than the free-stream velocity. For example, the free-stream velocity for the 2 mm case in the u-direction is approximately 650 m/s at 550 K, but the droplets are, on average, traveling at about 40 m/s. The droplets are about 16× slower than that of the free-stream in this case. High droplet velocity magnitudes are likely skewed by initial ligament breakup, which generates the high-velocity droplets. As this seems to be a very unstable and unpredictable phenomenon, it may be difficult to model or correlate with other effects. More work is needed to understand the dynamics behind this phenomenon and if the statistics can be correlated to other meaningful jet parameters.

Figure 4.21 illustrates a time series of images of the ligament breakup at J = 21.8

(300 psi) for a 2 mm jet. Ligament formation can occur in both the 0.5 mm and 2.0 mm diameter injectors, but the most defined images are those from the 2.0 mm jet where droplets can be sent downwards toward the test section floor. As these droplets move further downstream, they continue to atomize, potentially enhancing breakup. For engine applications, initial ligament breakup near the jet could help promote the start of combustion or improve flame stability. Thus, future work in this area could help improve combustion for ramjets or scramjets.

CHAPTER 5

LEEWARD SIDE OF JET - RESULTS AND DISCUSSION

The previous chapter outlined the jet penetration depth and the innate unsteadiness of the jet, which leads to oscillations along the front of the liquid jet. These characteristics affect the droplet atomization, leading to variations in the velocities and diameters of the droplets on the leeward side of the jet. Studying the downstream atomization will also improve our understanding of front-edge mixing and momentum flux ratio effects on atomization in the supersonic regime. This chapter shows how DIH can be used to image the droplet field to determine particle sizes and how DIH can be combined with FFT window deformation code to extract droplet velocities at several x/D and y/D locations.

As discussed in chapter 3, rig thermal expansion makes it nearly impossible to image a fixed location in the flow, especially at high magnifications near the tunnel floor. Without a reference, there is no way to replicate the sampling location. Therefore, a 2×3 wire grid was constructed and affixed to the test section to serve as a point of reference when the rig expands. Here, $\sim$0.5 mm diameter wire was used to form each line in the grid. Figure 5.1 shows a schematic of the circular window overlaid with the wires, corresponding to x locations of 2.5 mm, 12.7 mm, and 20.3 mm from the liquid injection point and y locations of 2.5 mm, 6 mm and 9 mm above the tunnel floor. These points were chosen because they sit within the breakup plume for most momentum flux ratios and droplet velocities are expected to vary across these regions. The origin of these locations was estimated by placing a long wire into the injector hole and illuminating it with the CW laser. From there, the measurements for each location were accurately made with a micrometer (accuracy of $\pm$ 0.001 mm). Based on the literature, translating up the y-axis at any of these locations should result in entering the droplet plume and the shear interface, causing a “C” shape pattern in the droplet velocity, as observed by Medipati et al. [27]. Translating

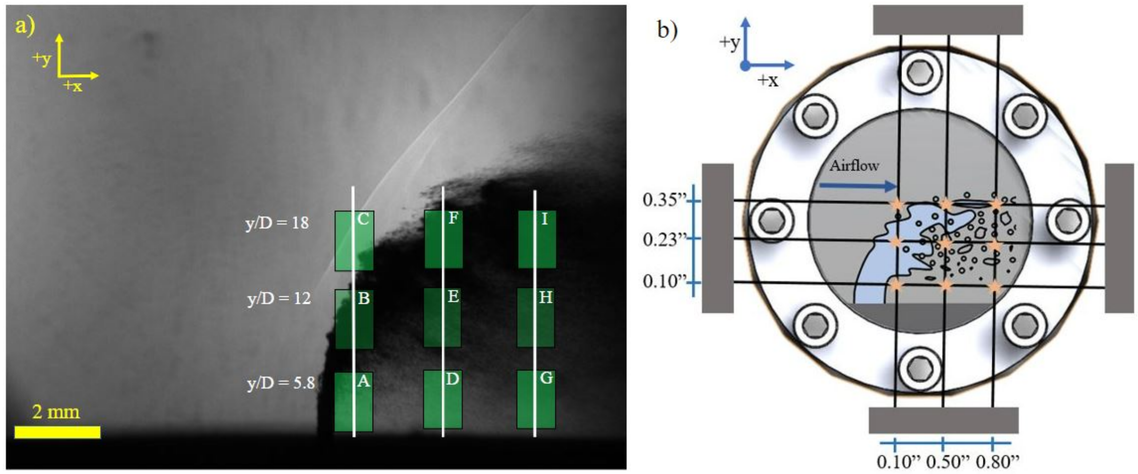

Figure 5.1: (a) A schlieren image shows the approximate locations where the data was collected for studying downstream droplets. The green boxes correspond to the field of views for the Shimadzu camera and CF-4 objective. (b) The wire grid schematic affixed to the wind tunnel side window is also illustrated. The x locations are displayed along the bottom of the wires while the y locations are shown on the side of the wires.

along the x-axis along the crossflow direction should result in an increased velocity, as the crossflow gas accelerates individual droplets.

5.1 Leeward Side of Jet - Phase Doppler Particle Analyzer

PDPA provides a method of simultaneously quantifying both droplet velocities and diameters in a particle field. These parameters directly influence the residence time of the atomized fuel in the combustion chamber and can change how well the fuel mixture burns. In off-the-shelf devices, the control system receives the Doppler information and correlates the parameters in real time. For this work, a TSI Instruments representative brought a PDPA Itasca 2D control system to demonstrate the optical technique on the supersonic JICF rig. The combustion lab provided the transmitting and receiving lenses, but it was later deduced that there were ring defects in the transmitted beam, which is indicative of contamination on the fiber end of the probe. Unfortunately, both components were affected, reducing the confidence in the gathered results. On top of this, the slit in the receiver had been tampered with and was held in place with masking tape. The slit limits the size of the measurement

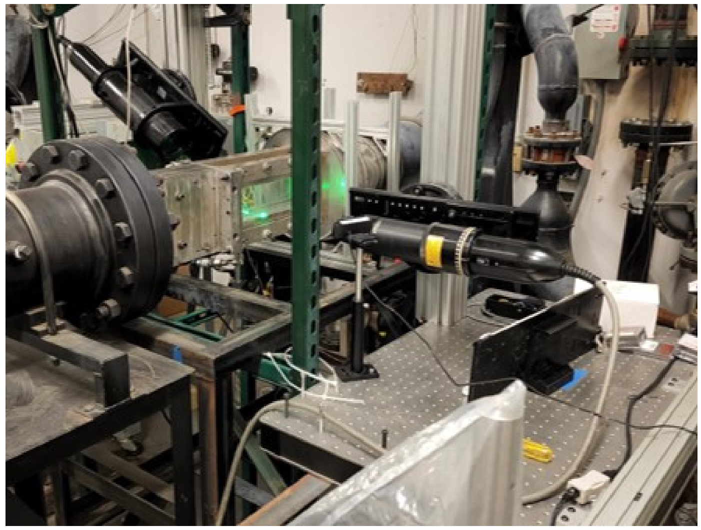

Figure 5.2: PDPA experimental setup from the receiving probe side.

volume and the standard size is about 125 μm. However, the slit on this receiver seemed to be approximately 500 μm, which would decrease the reliability of the diameter measurements. A final source of error is the upstream PIV seeds that were obstructing flow in the homogenizer section. These seeds have a fixed diameter and are picked up as false readings, affecting both the diameter and velocity measurements. After this effect was noted, the facility was cleaned so that DIH measurements would not be affected. All of the DIH data in this work was collected after the facility cleaning.

PDPA configurations are typically built on angular stages so that the transmitter is at an angle in relation to the receiver. The PDPA setup at an approximate location of one inch downstream of the injector is shown in Figure 5.2. The PDPA tests include two downstream locations: one immediately after the injector and one about one inch (25.4 mm) downstream. Both points are right above the ground of the test section. The diameter of the injector is 0.5 mm for these tests. For calibration, a line was run to an oil droplet generator and placed in the exhaust section of the wind tunnel, spewing droplets toward the injector. This calibration method was used to verify that the control unit is correctly retrieving velocity and data from the probes. Next, the oil generator line is removed and the crossflow air was preheated to the 550 K. Because thermal expansion could not be counteracted, the setup was translated once the conditions reached steady state. It is important to note that near the end of the test slot, the air ran low, which caused fluctuations in the crossflow air pressure. Eventually, the stagnation pressure decreased, which stopped the experiment. Figure 5.3, Figure 5.4, Figure 5.5, and Figure 5.6 show some preliminary velocities and diameters from a J = 5.4 (75 psi) and J =36.3 (500 psi) jet at a location immediately after the jet injection.

Both pressures were captured at the same location right after the jet injection point near the tunnel floor. Because of the aforementioned issues with the equipment, a few cautious conclusions can be drawn from these results. First, the mean droplet velocity for the 75 psi and 500 psi cases are 16.8 m/s and 15.0 m/s, respectively. Their corresponding average diameters are 2.92 and 2.21 $\mu\mathrm{m}$. The velocity histograms differ slightly in the fact that the J = 5.4 (75 psi) graph is slightly negatively skewed, which raises the mean velocity compared to that of the J = 36.3 (500 psi) data. Unexpectedly, the mean particle diameter is greater

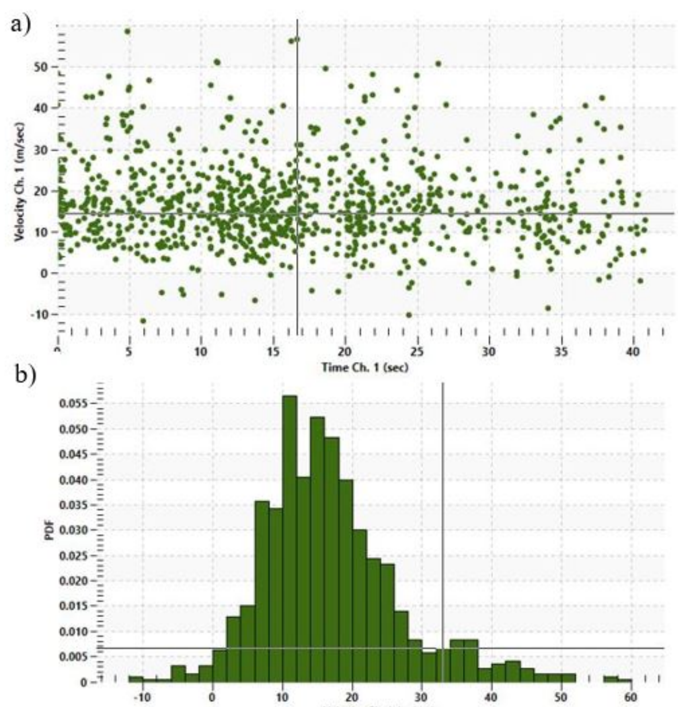

Figure 5.3: (a) The droplet velocity spread over a 45-second collection time for J = 5.4 (75 psi). (b) A probability distribution (PDF) of velocities is also shown. The location of the measurement is right after the jet injection near the tunnel floor.

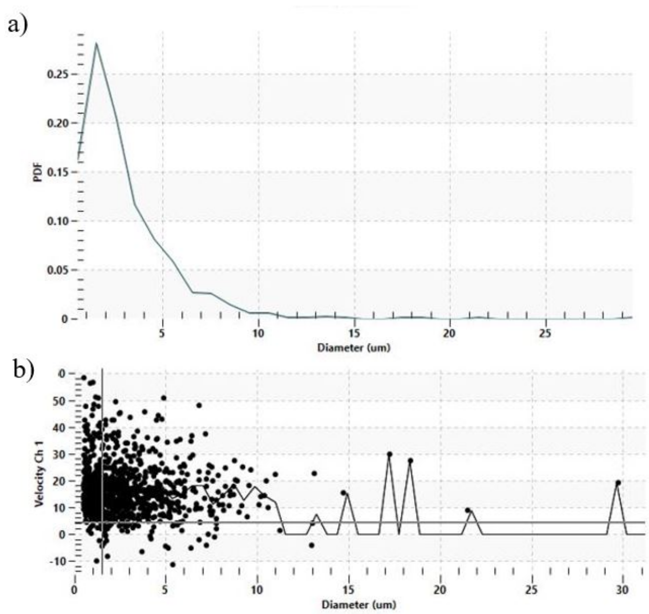

Figure 5.4: (a) PDF of the droplet diameters with the intersecting lines denoting the mean for J = 5.4 (75 psi). (b) The droplet diameter-to-velocity relationship is also shown. The location of the measurement is right after the jet injection near the tunnel floor.

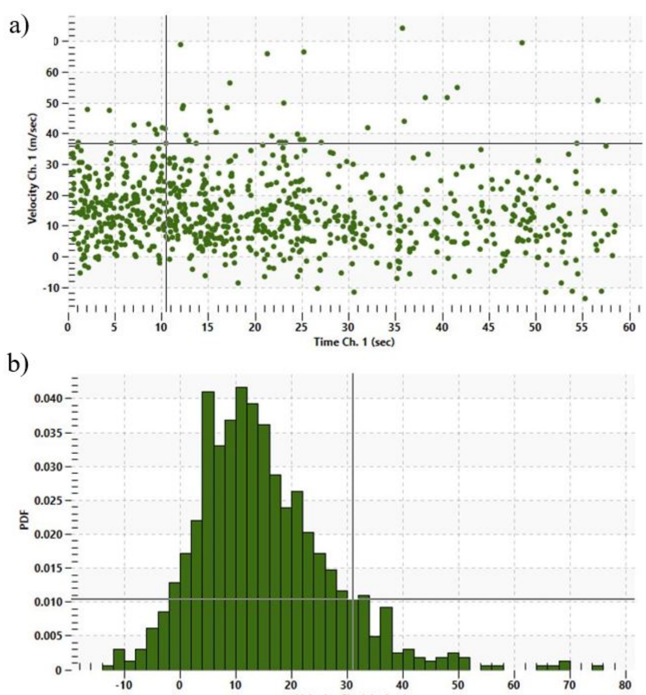

Figure 5.5: (a) The droplet velocity spread over 61 seconds of collection time at J = 36.3 (500 psi). (b) A PDF of velocities is also shown. The location of the measurement is right after the jet injection near the tunnel floor.

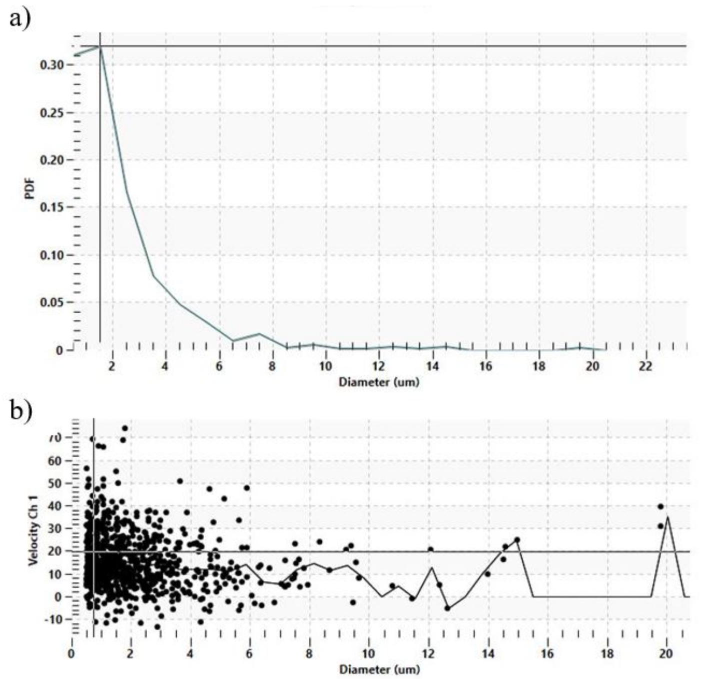

Figure 5.6: (a) The PDF of the droplet diameters with the intersecting lines denoting the mean for J = 36.3 (500 psi). (b) The droplet diameter-to-velocity relationship is also shown. The location of the measurement is right after the jet injection near the tunnel floor.

in the J = 5.4 (75 psi) case yet the velocities are slower. Both pressures show the expected correlation between the particle size and the velocity, as larger particles tend to translate slower than their counterparts.

Overall, however, the measured velocities appear to be low for the point right after injection, especially compared to the findings that will be discussed later in this chapter. This preliminary PDPA study shows that there exist some inaccuracies in the measurements, particularly for the droplet diameters. In the future, PDPA should be retested in the supersonic JICF facility with equipment that is in good working condition. Since this data only represents one data collection series, the results may not be accurate or repeatable. Repeated instances of the tests in the future would also increase the reliability of the results. Because PDPA data cannot be visually confirmed, there are many uncertainties in the results. Unlike PDPA, more accurate velocity and diameter data can be obtained and visually/manually checked with DIH, since DIH is inherently an imaging technique.

5.2 High-Speed Digital Inline Holography

High-resolution DIH can also be used to gather information on droplet velocity and diameter distributions. For estimating droplet velocities, time-resolved data and cross-correlation codes are used. The cross-correlation technique uses all the droplets in the line of sight and relies on multiple frames to compute an average displacement inside the flow. Because individual droplets are not tracked in this method, particle velocities can be obtained in the denser regions of the flow field. Note, however, that if a plume is too dense, then the laser cannot penetrate through the flow field and velocity data cannot be accurately measured. While this velocity measurement method has advantages over single-droplet tracking methods, additional work is needed to determine if the method has any biases towards different locations in the flow.

5.2.1 Droplet Velocity Trends

Here, the downstream droplet velocities were analyzed the same way as before where a series of time-resolved frames are obtained, cross-correlation using the FFT method is implemented, and velocity magnitude vectors are estimated for different regions in the flow. The same DIH experimental setup with the Shimadzu HPV-X2 camera, CF-4 lens, and CW laser was also implemented here. The only difference, in this case, is that the camera moves to three downstream positions at an x of 2.5 mm, 12.7 mm, and 20.3 mm. This corresponds to an x/D of approximately 5, 25, and 41, respectively. The y distances were dependent on the maximum frame height after the Shimadzu was rotated on its side. This allowed 400 pixels in the vertical direction and 250 pixels in the horizontal direction so more information could be captured along the vertical axis for each position. Thus, the total y/D in the vertical direction was about 5.8, or a y of approximately 2.9 mm. Experiments were also carried out at three vertical points at y/D of 5.8, 9.3, and 10.6.

The goal of this downstream study was to track the droplet velocity at different down-

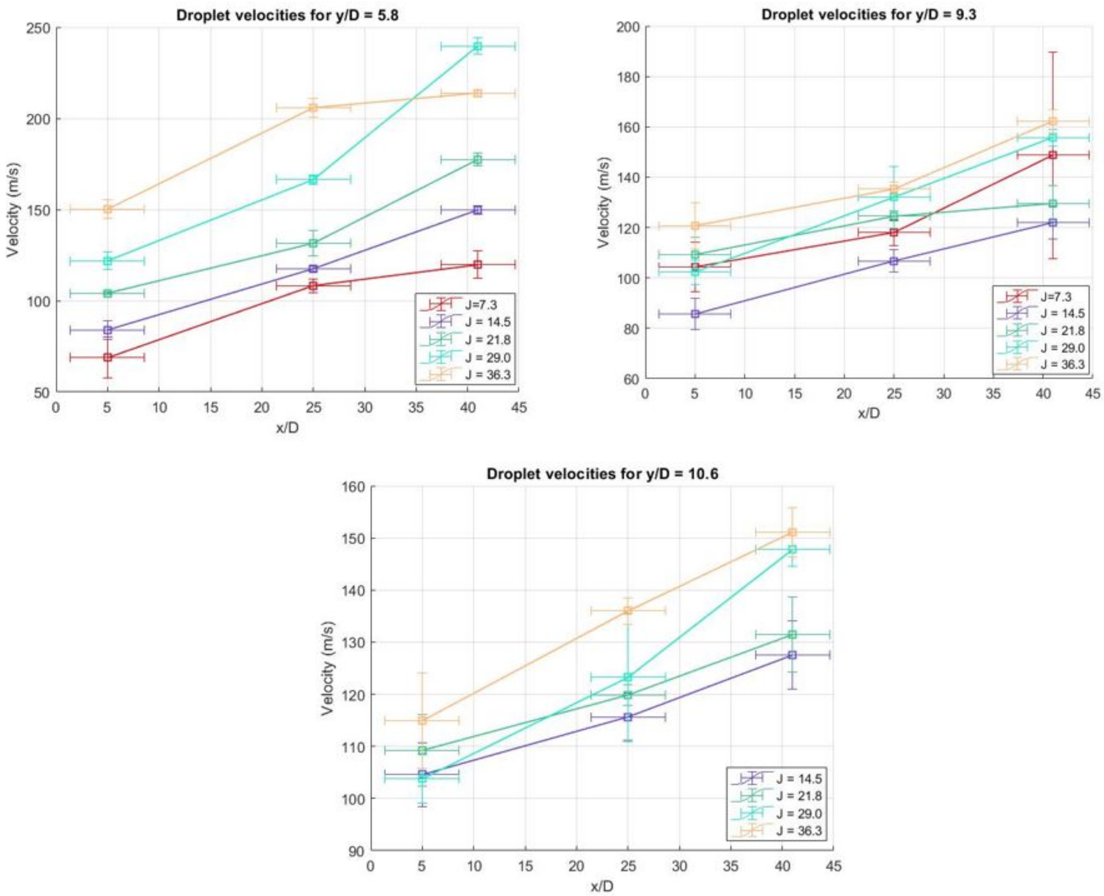

Figure 5.7: Droplet velocity curves in the x-direction for several y/D and pressure cases with a 0.5 mm diameter injector are shown. The x-direction velocity decreases from y/D = 5.8 to 9.3 as the droplets are in the dense region of the flow. The particle velocities increase in the y/D = 10.6 region because the droplets are outside the thick plume.

stream positions. For this test, it is hypothesized that the droplets would be accelerated by the flow as they reach full atomization, with velocities at each subsequent location being higher than that of the previous location. The curve should, in theory, eventually reach an asymptote were droplet velocities no longer increase. The graphs in Figure 5.7 display the results of this study. Here, the 0.5 mm diameter jet is used and the reported mean horizontal velocities are shown. The standard deviation of the measurements from thousands of data points within the flow is also included.

From this data, a clear trend is noted from y/D = 5.8 to y/D = 9.3, where the velocities decrease for all cases but the J = 7.3 (100 psi). The reason for this is that these locations

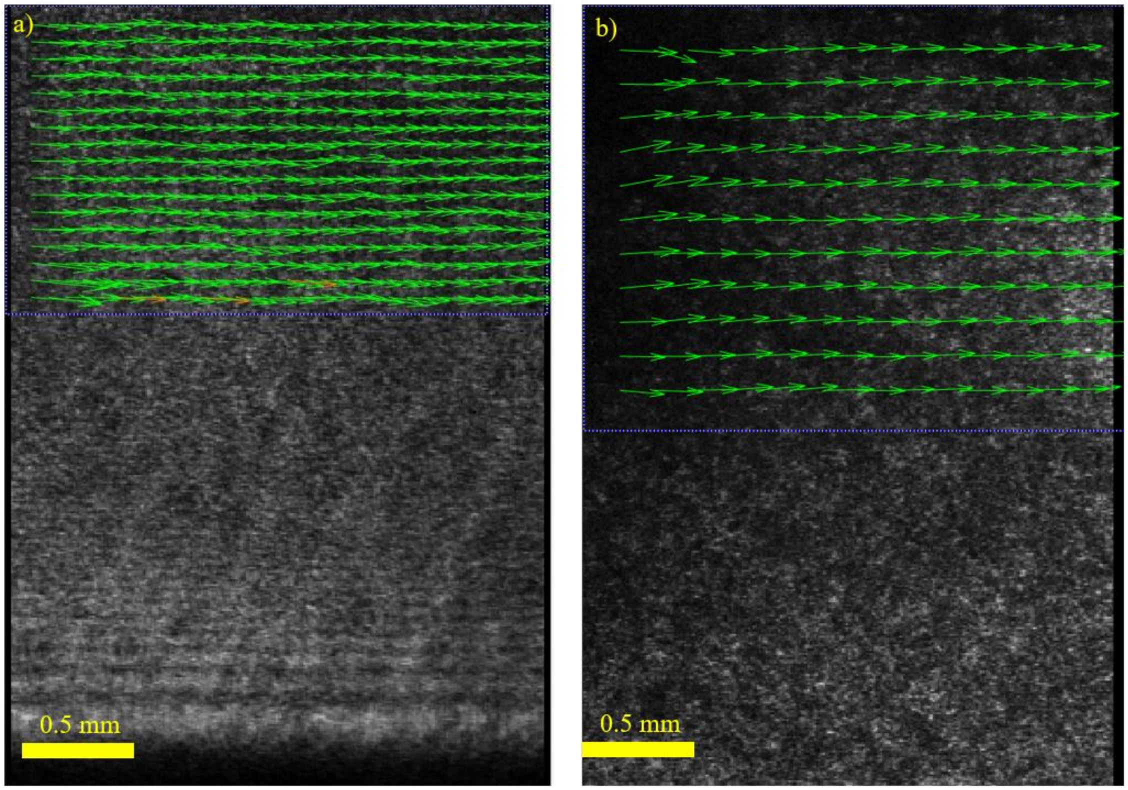

Figure 5.8: (a) The velocity vectors for x/D = 5 and y/D = 5.8 and (b) for x/D = 5 and y/D = 12.0 are illustrated for a J = 21.8 (300 psi) water jet. The droplet velocity magnitudes slightly increase moving from y/D = 5.8 to 12.0 as the droplets are closer to the shear interface edge. The diameter of the jet is 0.5 mm.

are inside the droplet plume, which is known to have a lower droplet velocity due to the increased droplet diameter. However, the J = 7.3 case has a lower penetration depth, which means that the y/D is closer to the shear interface region than for other cases. Droplets are of a smaller diameter and faster velocity here. Therefore, the velocity at y/D = 9.3 is higher than at y/D = 5.8. The y/D = 10.6 region is slightly outside of the highest-density droplet plume, so the particle velocities are greater than at y/D = 9.3. The J = 7.3 case could not be captured for this set of locations because the laser beam is far above the shear interface layer and no droplets are present.

Next, velocity curves as a function of y/D were developed using the cross-correlation method from the front-edge droplets. Figure 5.8 shows the result of applying the method to a J = 21.8 (300 psi) water jet at two different locations: y = 2.9 mm and y = 6.0 mm at the same x location. The blue bounding box of the region of interest defines the analysis area. The magnitude of the velocity vectors clearly changes as the camera moves into the droplet plume area and near the shear interface edge.

Because a specific ROI can be chosen, a single image can be partitioned into multiple different areas to observe and extract velocity information. Figure 5.9 is the compilation of all the velocity curves for the 0.5 mm diameter jet at different positions in the flow. Here, the x-direction velocity curves for every case resemble that of the letter "C" because the droplets decrease in velocity as the plume thickens and increase in velocity when approaching the shear interface. This finding agrees with the findings by Medipati et al. [27] and can have repercussions on where flame holding begins in the flow. For droplets in the center of the "C" shape, the velocity is reduced, which increases the residence time the mixture has to combust. However, if the droplets have a higher diameter in this region, then the chance of complete combustion decreases. Experiments with reactive fuels are needed to explore this effect in more detail. Overall, it is expected that the droplet diameters increase with plume density and decrease with droplet velocity (due to drag). To help determine the relationship between size and velocity, droplet velocities are explored in the next section.

While the FFT method is used to obtain velocity vectors, it is also possible to check the droplet velocities manually by tracking individual droplet diffraction rings. Here, fifty droplet velocities were tracked manually to determine if there is deviation between the manually tracked data and the automated FFT code. The average standard deviation of all points is 0.52 pixels in the x/D direction between the two methods. This error falls within the acceptable range, which would be a deviation of 1 pixel or less. Thus, the error between the automated code and the manual process is most likely due to pixel-level quantization in the manual tracking process, since the FFT process can track motions that are sub-pixel. Thus, the velocities measured using the FFT method are likely to be a fairly accurate representation of the droplet velocities in the flow.

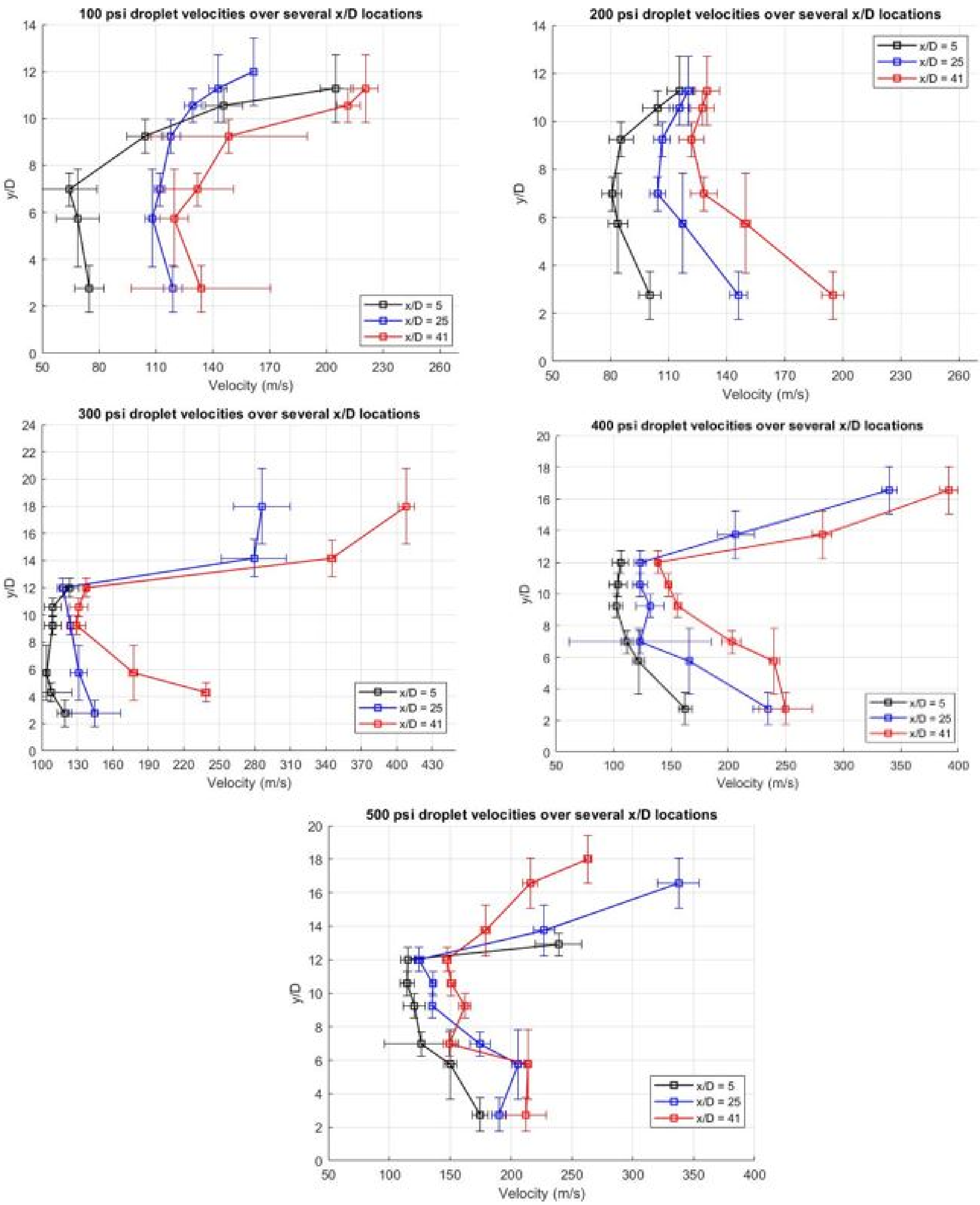

Figure 5.9: The droplet velocities in the x-direction as a function of vertical height in the jet for all 5 jet injection pressures is displayed here. Each pressure is tested at 3 different horizontal locations, denoted by x/D. The diameter of the injector is 0.5 mm. The measured velocities form a "C" curve where higher velocities are measured at the top and bottom of the flow.

5.3 Pulsed Instantaneous Digital Inline Holography

In order to analyze the droplet diameters and determine trends that are found at different injection parameters, a high-resolution DIH system is implemented to study the leeward side of the jet. The pulsed instantaneous DIH setup included a pulsed Litron laser at a timing box-driven frequency of 10 Hz. A Blackfly camera was synchronized to the Q-switch of the laser to ensure that the camera would capture the images at the correct time.

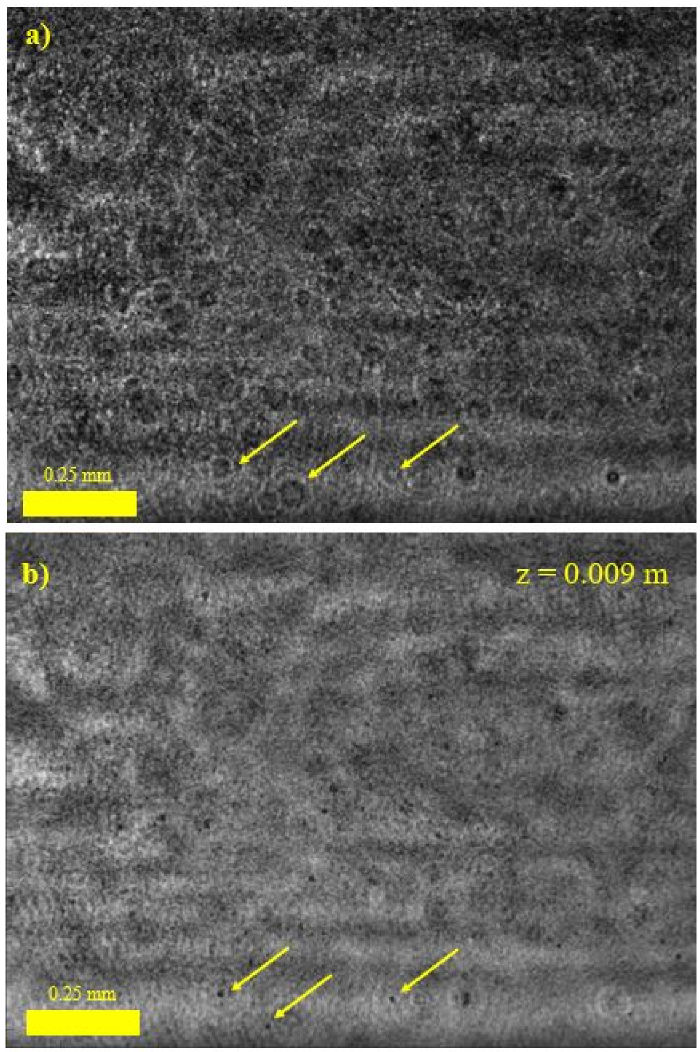

Figure 5.10: Droplet sizing holograms are shown for J = 29 (400 psi at x/D = 5 and y/D = 2. The arrows in both images show droplets in the (a) raw hologram and (b) the refocused hologram. The focal depth of the image is denoted in (b). More particles will come into focus as this depth is adjusted.

The laser power was set to a high level to keep the laser output intensity steady between the frames. To avoid overexposure, the beam was attenuated with a half waveplate and a polarizing beam splitter, which allows the light intensity to be varied based on the waveplate angle. In order to analyze droplet sizes accurately, images are taken slightly behind the jet in a low-density region of the flow so that clear Fresnel diffraction patterns can be visualized. Here, the DIH codes are used to refocus the diffraction rings. As the droplets come into focus, the fringes move in tighter to the droplet edge before they come into sharp focus at the focal depth of the droplet. Figure 5.10 shows a pair of downstream images of the water jet at J = 29 (400 psi) at a downstream position of 2.5 mm. One of the images shows a raw hologram and the other shows an image refocused to the droplet focal plane. For all experiments, the 0.5 mm diameter jet was used to maintain low droplet densities in the flow.

5.3.1 Droplet Diameter Trends

Another important parameter in liquid supersonic JICF is the droplet diameters on the leeward side of the jet. In far downstream locations, these droplet sizes are expected to follow a backward "S" shaped curve along the cross-streamwise direction because the droplet plume and shear layer have direct effects on particle atomization [27, 67]. In this work, however, it was determined that for the maximum x/D attainable within the first window (x/D $\sim$ 41), the particle field was too dense for accurate measurements. Furthermore, for the downstream location of x/D $\sim$ 250, the completely atomized particles are so small that a higher magnification setup than the one currently available is needed for accurate measurements. For this facility, further magnification is difficult because of the fixed minimum standoff distance between the window and the centerline of the facility.

After scanning several locations in both the x/D and y/D directions, the location x/D $\sim$ 5 and y/D $\sim$ 2, located only 2.5 mm downstream of the jet injection, was found to have a droplet breakup field with the lowest density. Thus, droplet diameters for all of the

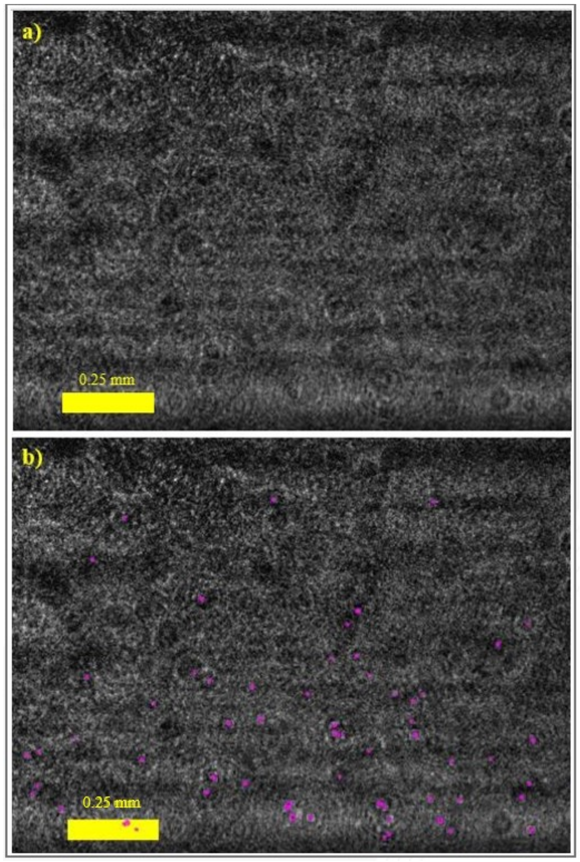

Figure 5.11: An droplet tracking example for J = 36.3 (500 psi) is shown at x/D $\sim$ 5 and y/D $\sim$ 2. (a) The raw hologram and (b) refocused hologram with pink circles indicating tracked droplets are shown. The image has been refocused from z = 0 to z = 13 mm and 67 droplets have been recorded from this image.

momentum flux ratios were tested at this location and an in-house diameter tracking code (provided by Ph.D. candidate Andrew Marsh of the Sensing Technologies Laboratory [59, 63]), was used to refocus and find the particle sizes. Figure 5.11 shows the raw hologram next to the numerically refocused and tracked image with overlaid pink circles indicating the location of tracked particles. Because the image is processed automatically and can find droplets from multiple focal depths, it provides a relatively unbiased estimate of particle sizes inside the flow.

These experiments were magnified to give a spatial resolution of $\sim$0.7 μ m/pixel, allowing the diameters to be transformed into a physical size measurement. For each data set, five frames out of a set of 100 with the clearest droplet diffraction patterns were chosen and

Table 5.1: Mean droplet diameters for various injection pressures.

Jet Pressure [psi]	Jet Momentum Flux Ratio	Mean Droplet Diameter [μm]	Diameter Standard Deviation
200	14.5	6.06	2.13
300	21.8	6.73	3.19
400	29.0	7.07	4.07
500	36.3	6.40	2.75

were numerically refocused in multiple focal depths. Droplet diameters were automatically found using a minimum amplitude and maximum Tenengrad method [68, 59]. The set of five frames yielded 200 to 300 individual particles, with the mean diameter and population standard deviations shown in Table 5.1.

The droplet diameter PDFs are visualized in Figure 5.12. Again, the kernel smoothing function was used here to fit the PDFs. These PDFs show that there seems to be a bimodal right-skewed diameter distribution at each of the tested momentum flux ratios. All pressures appear to have very close dominant peak diameters, at 4.90, 4.65, 4.65, and 4.77 μm, corresponding to injection pressures of 200, 300, 400, and 500 psi, respectively. Particle diameters for this location are in the range of 3.65 to 30.58 microns. In this data set, the 100 psi jet was not plotted as the particle field for this case was too dense for accurate measurements. More work needs to be done to understand if there are unaccounted droplets at each of these locations that would change or skew the graphs.

Because there are two peaks in each of the PDFs, there is a possibility that diameters are correlated with height in the flow. Thus, the diameters were plotted against y/D location in Figure 5.13 to determine if there are any height-related statistics. These graphs consistently show that the larger diameter droplets are closer to the floor of the test section and that the diameters decrease as a function of height. Lin et al. [67] found that the droplet diameters follow a backward "S-curve" in the flow, where droplets tend to be larger near the combustor floor and decrease as the height increases. Lin et al. also estimates that the average droplet diameters increase and decrease several times depending on the location within the plume. In this study, the data shows that the droplets follow the initial part of the curve, where the diameter tends to decrease as the y/D position increases. However, be-

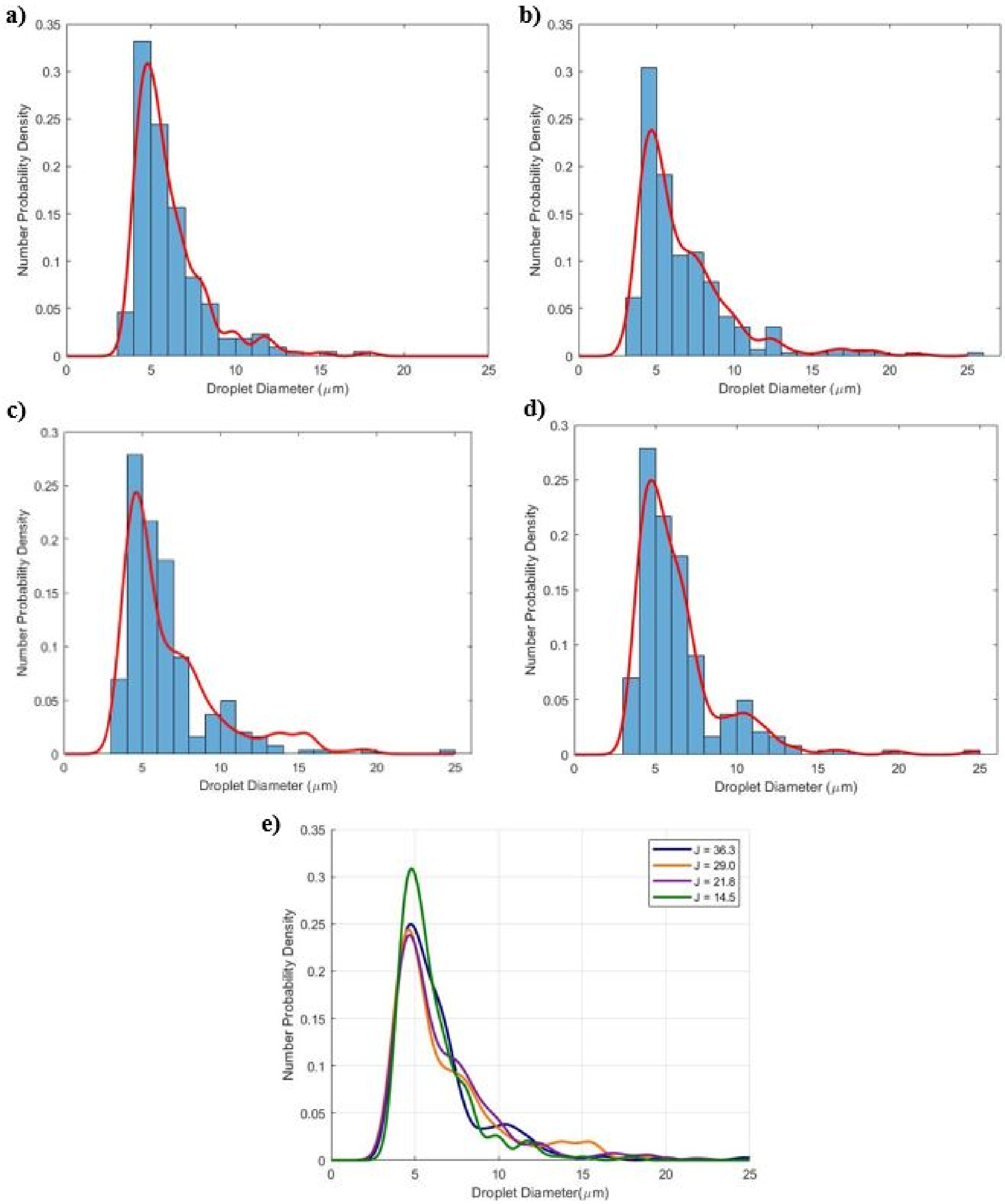

Figure 5.12: Several probability number density curves for J = 14.5 to 36.3 (200 to 500 psi) jets at x/D = 5 are shown with a 1 μm bin width. (a) PDFs for J = 14.5 (200 psi), (b) J = 21.8 (300 psi), (c) J = 29.0 (400 psi), and (d) J = 36.3 (500 psi) are illustrated. (e) A combination of all of the curves overlaid on each other is also shown. All curves resemble a bimodal right-skewed distribution.

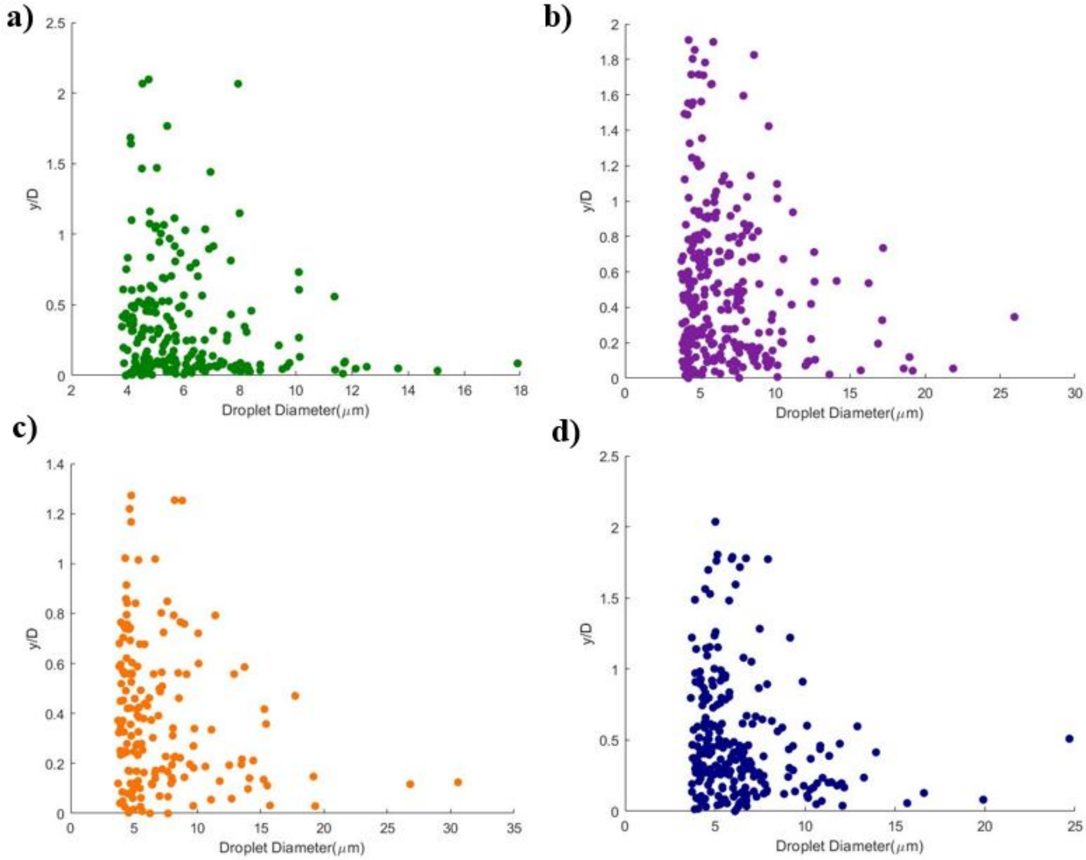

Figure 5.13: The droplet diameter spread in the y/D direction at a fixed x/D = 5 is displayed. (a) Curves for J = 14.5 (200 psi), (b) J = 21.8 (300 psi), (c) J = 29.0 (400 psi), and (d) J = 36.3 (500 psi) are illustrated. Larger droplets are seen near the bottom of the test section, agreeing with previous studies [67].

cause the number of droplets identified decreases with height, it is uncertain if the observed trend is biased due to density. Furthermore, because of the high droplet density further up in the plume, more cross-streamwise locations cannot be currently tested for the 0.5 mm jet. Thus, it is not possible to observe if the predicted curve holds for the entire column and more data is needed.

Overall, this chapter showed how the interactions between the liquid jet and the cross-flow air result in droplet velocity and diameter variations. Definitive velocity trends have been quantified in this work, which agree with other measurements in the literature. In the case of droplet diameters, initial analysis also indicates some agreement with literature values. However, additional work is needed to verify these results. In general, this chapter has shown how DIH can be used to measure both droplet velocity and droplet diameter. DIH techniques and automated codes can greatly enhance the number of particles observed per test because numerical refocusing can be used to accurately measure particles at multiple focal depth. This further improves our understanding of droplet statistics, which will can be used to improve supersonic JICF models and enhance our understanding of combustion processes in an air-breathing vehicles.

CHAPTER 6
CONCLUSIONS AND FUTURE WORK

6.1 Conclusions

In this work, liquid jets in supersonic crossflow are tested at several injection velocities and diameters in order to quantify flow features, windward instabilities, and droplet breakup. Several optical techniques are employed to gather information about the jet. Schlieren imaging is first utilized to characterize the flow features and examine the motion of the bow shock in front of the liquid jet. This technique assists in forming the primary framework for penetration depth and provided a first look into the droplet density within the plume. Digital Inline Holography (DIH) was then utilized and a spatially collimated beam of laser light was passed through the flow field, refracting off the liquid droplets. A three-dimensional hologram is captured and reconstructed through the use of numerical refocusing and back propagation algorithms developed using in-house codes. This is used to capture flow dynamics and droplet breakup behaviors at the front-edge of the jet as well as droplet velocities at the leeward side of the jet with a high-speed Shimadzu HPV-X camera. A Blackfly high-resolution camera and a nanosecond pulsed laser are then used to take instantaneous images of the downstream droplet field to extract droplet diameters. This work forms a foundation for the use of DIH in supersonic JICF as a diagnostic tool that can be used to measure bow shock locations, density gradients, flow features, droplet velocities, and droplet diameters.

This work makes several novel contributions to the fields of liquid supersonic JICF and optical diagnostics. Some of the major contributions and takeaways include:

1. The design, construction, and characterization of a liquid jet in a supersonic cross flow rig enable the collection of unique liquid jet breakup data.

2. The measurement of jet penetration depth trends for various injection pressures and comparison with existing curve fits show that some modifications are needed to existing logarithmic correlations in order to explain the experimental data.

3. Initial analysis of the jet instability shows an inverse relationship between the dominant instability wavelength and the momentum ratio. Additional analysis is needed to confirm this result.

4. This work is the first to use DIH to characterize liquid jet breakup in a supersonic JICF. Data collected in this work shows that the bow shock, windward instabilities, droplet velocities, and droplet sizes can be captured using this single technique. Numerically refocusing enables the analysis of droplet diameters in multiple focal depths, which enables more droplets to be characterized per experiment than other techniques.

5. Droplet breakup is found to occur for the first time in the literature at the front of the jet for large-diameter orifices. The 2.0 mm diameter jet, for example, had repeatable instances of droplets shearing off the front edge and falling toward the test section ground following the vectors of the recirculation zone. Although it is unknown how this will affect combustion, these results can be added to improve mathematical models of supersonic JICF.

6. Velocity trends for downstream droplet breakup are described for a variety of y/D locations in the flow. In literature, a droplet velocity C-curve has been found showing that droplets decrease in velocity as the particle density increases. Then, the droplet velocities drastically increase near the shear interface [27]. This phenomenon is confirmed in these experiments using only DIH cross-correlation velocity estimates in the 0.5 mm diameter jet.

7. For x/D $\leq$ 41, droplet velocities increase as the horizontal distance increases. This

suggests that the droplets are accelerating due to the freestream air.

8. Droplet diameter data collected at a fixed downstream position (x/D $\sim$ 5 and y/D $\sim$ 2.5) currently do not show any trends with the momentum ratio. Preliminary data appears to show some of the trends outlined by Lin et al. [67]. Future work is needed to confirm these results.

6.2 Future Work

Future work into liquid jets in supersonic crossflows can greatly improve the design of scramjet combustors. This includes experiments that study different types of liquids with differing viscosities and surface tensions. Because liquid fuels, like Jet-A, are commonly used for scramjets, it would also be beneficial to study the instability and droplet breakup effects in real fuels.

Because liquid jets have three-dimensional features, it would also be extremely useful to reconstruct the jet and extract information at multiple planes or cross-sections. Peering into different planes can help shed some light on the role of the recirculation zones and the direct effect of shocks on mixing. As these factors have a direct impact on the flame-holding steadiness, these factors are also worth exploring using holography or tomography techniques.

The incoming crossflow boundary layer thickness can also have a profound influence and could control how the instabilities propagate, especially within the boundary layer. PIV, for example, is one technique that can be used to estimate the boundary layer thickness for each test case [37]. This data can then be used to examine if there is a direct correlation between the boundary layer flow and front-edge breakup phenomenon.

The bow shock can also contribute to front-edge breakup phenomena. Bow shocks are known to fluctuate slightly and interact with the boundary layer. Additionally, measurements from the experiments conducted in this work have shown how they can move with oscillations in the liquid jet. Thus, their variation over time in the streamwise direction should be explored in the future. The closer the shock is to the jet, or the more downstream it is, the lower the penetration depth will be, which has effects on entrainment. Even if the bow shock cannot be directly controlled, information on its position is valuable to quantify in order to better understand the steadiness of the jet. One way to capture this information is to move the optical diagnostic to regions where the bow shock, boundary layer, and liquid jet can be viewed simultaneously. Then, in-house edge tracing codes could be used to binarize the image and extract the instantaneous bow shock locations. Using this data, the mean shock path and standard deviation from oscillation can be quantified to help improve our understanding of the role of the bow shock in instability growth and breakup dynamics.

Furthermore, an updated wind tunnel design with more windows would allow the rig operator to target more downstream locations. Currently, the ranges for x/D are x/D $\leq$ 50 and 250 $\leq$ x/D $\leq$ 350. Another set of windows in the middle would elongate that range to cover more intermediate positions. Because full droplet atomization is predicted to occur at an x/D of $<$ 100, new windows could be placed right after the first set to get a full droplet size variation from start to finish. The current wind tunnel could most likely be modified to accommodate this. By adding new optical access points, the specific location where full atomization occurs could also be quantified.

To help integrate DIH into droplet breakup in supersonic JICF, an even smaller diameter jet than 0.5 mm can be tested in the future. Smaller jet diameters help reduce fluid droplet densities in the leeward portion of the flow. By using a smaller injector diameter, it is also potentially possible to observe and quantify droplet breakup in more detail.

Lastly, while these experiments only use a single orifice injector, it would be interesting to see the effects of using two orifices at the same time. Double orifice injectors typically have a higher diameter so the droplet plume field would be very dense. However, the interaction between the two jets could enhance the mixing process, thereby improving flameholding stability. To decrease the plume density for measurement, injector diameters that are less than 0.5 mm could be used so that droplet diameters can be characterized at more downstream locations.

In this work, we successfully characterized many flow parameters in a liquid jet in supersonic crossflow with a small 0.5 mm orifice diameter. DIH is used for the first time to study several different features in this flow. Jet penetration data from this work shows good agreement with previous literature with some slight modifications needed to improve fitting parameters. For higher diameter orifices, a unique breakup phenomenon was noticed at the front of the jet with droplets moving downwards toward the test section floor. This work is the first to note this phenomenon and additional work is needed to elucidate the mechanisms that drive this flow feature. This work is also the first to use DIH to measure droplet velocities and diameters, showing good initial agreement with other experiments in the literature. Because the eventual goal of this work is to increase the fidelity of mathematical models, produce more efficient combustor designs for scramjets, and increase engine power output, testing with fuels would be an interesting next step. The optical measurement techniques developed in this work can not only be used in reacting supersonic JICF systems but can also be improved in the future to study density gradients generated by vaporization and flame propagation effects.

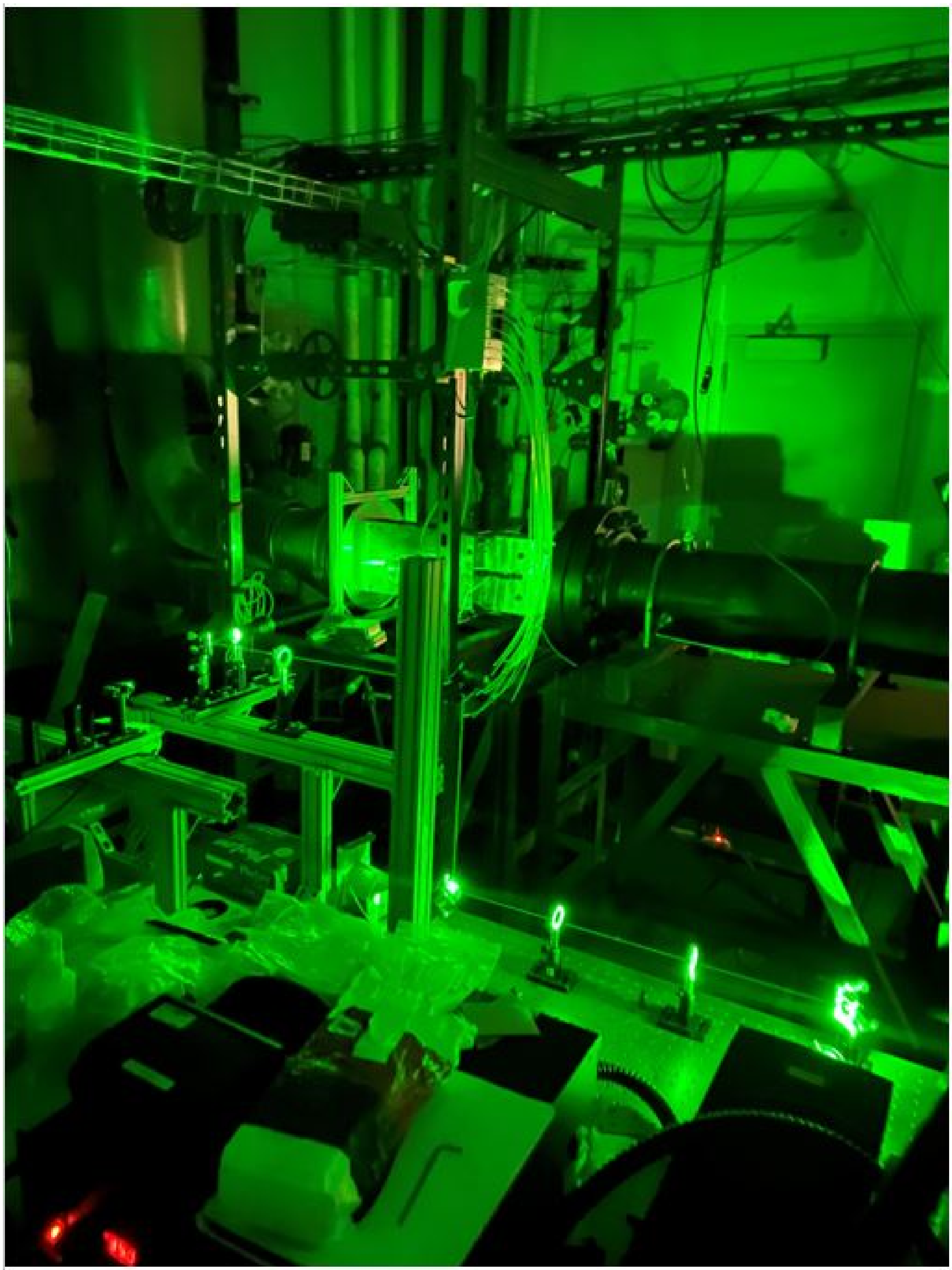

Figure 6.1: The 532 nm CW laser beam is shown as it passes through the setup.

Appendices

APPENDIX A

DATA PROCESSING EDGE TRACING CODE

Many MATLAB codes were produced to analyze video data, but the developed edge tracing code is especially important for this research. This code provides a robust way to trace any edge in an image and creates arrays to tabulate the penetration depth of the jet. It is easy to implement into a loop to produce edges and depths for all frames in a video. The only user input required is contrast limits (0 to 1 for both lower and upper limits), which allows the cross-correlation algorithm to extract the data more consistently. Optional data truncation is included to delete boundaries that are not of interest to the analysis, such as the droplets or physical limits of the test section.

Contents


```
%%%%%%%%%%%%%%%%%%%%%%%%%%%%%%%%%%%%%%%%%%%%%%%%%%%%%%%
%%%%            Joshua Johnson 2022 - 2023         %%%%
%%%%  Liquid Jet in Supersonic Crossflow Project   %%%%
%%%%              Edge Tracing Code                %%%%
%%%%%%%%%%%%%%%%%%%%%%%%%%%%%%%%%%%%%%%%%%%%%%%%%%%%%%%

close all;
clear all;
clc;
fontSize = 10;

warning off;
```

Tracing with Inverse Pixel Binary (imcomplement)

```
folder = pwd;
baseFileName = '04-15-2022 - 200PSI Air 300PSI Jet-04152022122111-19.tiff';
fullFileName = fullfile(folder,baseFileName);

if ~exist(fullFileName, 'file')
    fullFileNameonPath = baseFileName;
    if ~exist(fullFileNameonPath, 'file')
        error = sprintf('Error: %s does not exist in this folder.',fullFileName);
        uiwait(warndlg(error));
        return;
    end
end
```

Calculating a colormap

```
[grayImage,storedColorMap] = imread(fullFileName);
if ~isempty(storedColorMap)
    grayImage = ind2rgb(grayImage, storedColorMap);
end
```

Dimensionalizing the image

```
%#ofcolorchannels = 1 for gray scale , 3 for colored/rgb.

[rows, columns, numberofColorChannels] = size(grayImage);
if numberofColorChannels > 1
    % This means it's a rgb image - so let's turn it into grayscale.
    grayImage = rgb2gray(grayImage);
end
```

Display the new grayscale rotated image (if rotation is needed)

```
hFig = figure;
subplot(2,3,1);
RotatedOriginal = imrotate(grayImage,90); % Set to 0 if no rotation needed
imshow(RotatedOriginal, []);
title('Original Grayscale Image','FontSize',fontSize, 'Interpreter','None');
hFig.WindowState = 'maximized';
drawnow;
```

Original image histogram to check for intensity values and their frequencies.

```
subplot(2,3,2);
imhist(grayImage);
title('Original Image Histogram - Pixel Intensity vs Frequency','FontSize',fontSize,'Interpreter','None');
grid on;
```

Binarize the image and fill with holes.

```
binaryImage = imfill(RotatedOriginal, 'holes');
binaryImageAdjusted = imadjust(binaryImage,[0.1 0.7],[]); % user input: adjust contrast limits until desired edges are traced.
subplot(2,3,4);
imshow(binaryImageAdjusted,[]);
title('Filled Binary Image using Custom Contrast Limits', 'FontSize',fontSize, 'Interpreter','None');
axis('on','image');
hp = impixelinfo();
set(hp,"Position",[300 30 200 20]);
```

Plot the binarized image histogram for pixel intensity vs frequency.

```
subplot(2,3,5);
imhist(binaryImageAdjusted);
title('Binary Image Histogram - Pixel Intensity vs Frequency','FontSize',fontSize,'Interpreter','None');
grid on;

% The purpose of this is to more uniformally divide the binary pixels.
% Now we look for boundaries between the dark and light scales.
```

Calculate intensity differences between pixels and threshold.

```
A = abs(diff(binaryImageAdjusted,1,2)); %Calculates the intensity difference between pixels next to each other
roi = A < 0.3;
EdgeBoundaries = bwboundaries(roi); % Looking for black/white boundaries

subplot(2,3,6);
imshow(255-RotatedOriginal,[]);
numBoundaries = length(EdgeBoundaries);
caption = sprintf('Inverted Grayscale Image with %d boundaries', numBoundaries);
title(caption, 'FontSize',fontSize, 'Interpreter','None');
hold on;
```

Draw a boundary everywhere the intensity values calculated an edge

```
for k = 1:length(EdgeBoundaries)
    thisBoundary = EdgeBoundaries{k};
    x = thisBoundary(:,2);
    y = thisBoundary(:,1);
    plot1 = [x,y];
    appendarray1 = [];
    NewMatrix(k) = [appendarray1,{plot1}];
    Transpose = transpose(NewMatrix);
        for l = 1:length(Transpose)
            newpair = Transpose{l}(1,:);
            plot2 = [newpair];
            appenedarray2 = [];
```

```
            NewMatrix2(l) = [appenedarray2,{plot2}];
            Transpose2 = transpose(NewMatrix2);
            newx = Transpose2{l}(:,1);
            newy = Transpose2{l}(:,2);
            plot3 = [newx(:), newy(:)];
            appendedarray3 = [];
            NewMatrix3(l) = [appendedarray3,{plot3}];
            Transpose3 = transpose(NewMatrix3);
            A = cell2mat(Transpose3);

                % Delete extraneous data from droplet traced edges
                %For example - A(A(:,1) > 140 & A(:,2) > 275,:) = [];
                % A(A(:,1) > 180 & A(:,2) > 200,:) = [];
                % A(A(:,2) < 10,:) = [];

        end

    plot(x,y,'k-','LineWidth',2);
end
xtraced = A(:,1);
ytraced = A(:,2);

%Saving the data
filename = '100psi penetration depth.xlsx';
sheet = 1; % I save each frame to a different sheet. You may append onto one sheet.
xlswrite(filename,A,sheet);
```

Create the scatterplot of the traced edges

```
figure()
scatter(xtraced,ytraced);
set ( gca, 'ydir', 'reverse' )
```

Published with MATLAB® R2021b

APPENDIX B

PARAMETER ENGINEERING EQUATION SOLVER CODES

The following code calculates several injector, water, and nozzle exit parameters. A parametric chart is presented, which utilizes an independent variable that is iterated to determine how dependent variables are affected. Note that the nozzle exit parameters is approximated to be the same as the freestream air at the point where the water jet is injected.

```
"Look at this equations for p_exitnozzle and v_exitnozzle on pages 12 and 13: http://imartinez.etsiae.upm.es/~isidoro/bk3/c17
/Nozzles.pdf "
"Using Ma = 1.71"

"P_water = 100*convert(PSI,kpa) convert to kpa"
T_water = 20 "C"
density_water =density(Water,T=T_water,P=P_water)
V_Water = sqrt(2*1000*P_water/density_Water) "Bernoulli's equation m/s, convert kpa to pa"


"For air velocity calculations"
T_entry = 550 "deg K, stag temp"
P_entry = 34*convert(PSI,kpa) "converted to kpa, stag press"
R_air = 287 "J/kgK"
Gamma_air = 1.381

v_exitnozzle = sqrt((2*Gamma_air*R_air*T_entry/(Gamma_air-1))*(1-(1/(1+(Gamma_air-1)/2*1.71^2)))) "m/s"
p_exitnozzle = P_entry/((1+1.71^(2)*(Gamma_air-1)/2)^(Gamma_air/(Gamma_air-1))) "kPa"
p_exitnozzlePSI = p_exitnozzle*convert(kpa,PSI) "PSI"
T_exitnozzle = T_entry*(p_exitnozzle/P_entry)^((Gamma_air-1)/Gamma_air) "deg K"
T_exitnozzleCel = T_exitnozzle - 273.15 "degC"

Density_air_at_injection = density(Air_ha, T=T_exitnozzleCel,P=P_exitnozzle)

r_injector = 0.0098425 [in]
d_injector = 2*r_injector "in"
h_injector = 0.375 [in]
V_injector = (pi*r_injector^(2)*h_injector)
A_surface_injector = (2*pi*r_injector*h_injector)
Lc_injector = V_injector/A_surface_injector
mu_water = viscosity(Water,T=T_water,P=P_water)
 Re_water = (density_water*V_water*Lc_injector)/mu_water

J_xwaterpsi = (density_water*(V_water)^2)/(density_air_at_injection*(v_exitnozzle)^2)

"Using Parametric Table with P = 100,200,300,400,500 respectfully."
```

Look at this equations for p_exitnozzle and v_exitnozzle on pages 12 and 13: http://imartinez.etsiae.upm.es/~isidoro/bk3/c17/Nozzles.pdf

Using Ma = 1.71

P_{water} *= 100*convert(PSI,kpa) convert to kpa*

$T_{water} = 20$ *C*

$density_{water} = \rho\left(water, T = T_{water}, P = P_{water}\right)$

$$V_{Water} = \sqrt{2 \cdot 1000 \cdot \frac{P_{water}}{density_{water}}}$$

Bernoulli's equation m/s, convert kpa to pa

For air velocity calculations

$T_{entry} = 550$ *deg K, stag temp*

$$P_{entry} = 34 \cdot \left| 6.895 \cdot \frac{kPa}{psi} \right|$$ *converted to kpa, stag press*

$$R_{air} = 287$$ *J/kgK*

$$\gamma_{air} = 1.381$$

$$v_{exitnozzle} = \sqrt{2 \cdot \gamma_{air} \cdot R_{air} \cdot \left[\frac{T_{entry}}{\gamma_{air} - 1} \right] \cdot \left[1 - \left[\frac{1}{1 + \left[\frac{\gamma_{air} - 1}{2} \right] \cdot 1.71^2} \right] \right]}$$ *m/s*

$$p_{exitnozzle} = \frac{P_{entry}}{\left[1 + 1.71^2 \cdot \left[\frac{\gamma_{air} - 1}{2} \right] \right]^{\left[\frac{\gamma_{air}}{\gamma_{air} - 1} \right]}}$$ *kPa*

$$p_{exitnozzlePSI} = p_{exitnozzle} \cdot \left| 0.145 \cdot \frac{psi}{kPa} \right|$$ *PSI*

$$T_{exitnozzle} = T_{entry} \cdot \left[\frac{p_{exitnozzle}}{P_{entry}} \right]^{\left[\frac{\gamma_{air} - 1}{\gamma_{air}} \right]}$$ *deg K*

$$T_{exitnozzleCel} = T_{exitnozzle} - 273.15$$ *degC*

$$Density_{air,at,injection} = \rho \left(Air_{ha} , T = T_{exitnozzleCel} , P = p_{exitnozzle} \right)$$

$$r_{injector} = 0.0098425$$ [in]

$$d_{injector} = 2 \cdot r_{injector}$$ *in*

$$h_{injector} = 0.375$$ [in]

$$V_{injector} = \pi \cdot r_{injector}^2 \cdot h_{injector}$$

$$A_{surface,injector} = 2 \cdot \pi \cdot r_{injector} \cdot h_{injector}$$

$$Lc_{injector} = \frac{V_{injector}}{A_{surface,injector}}$$

$$\mu_{water} = \mathbf{Visc} \left(water , T = T_{water} , P = P_{water} \right)$$

$$Re_{water} = \frac{density_{water} \cdot V_{Water} \cdot Lc_{injector}}{\mu_{water}}$$

$$J_{xwaterpsi} = \frac{density_{water} \cdot V_{Water}^2}{Density_{air,at,injection} \cdot v_{exitnozzle}^2}$$

Using Parametric Table with P = 100,200,300,400,500 respectfully.

Parametric Table: Table 1

	$J_{xwaterpsi}$	P_{water} [kPa]	Re_{water}	V_{Water}	$p_{exitnozzlePSI}$	$T_{exitnozzle}$	$v_{exitnozzle}$
Run 1	7.252	689.5	182349	37.16	6.831	353.2	639.8
Run 2	14.5	1379	257976	52.55	6.831	353.2	639.8
Run 3	21.76	2068	316070	64.35	6.831	353.2	639.8
Run 4	29.01	2758	365098	74.29	6.831	353.2	639.8
Run 5	36.26	3447	408339	83.05	6.831	353.2	639.8

APPENDIX C

STANDARD OPERATING PROCEDURES (SOP)

The following pages show the standard operating procedure for the supersonic rig when operating with a data acquisition system (DAQ). The steps used to successfully start the compressor, turn the burner on, and run the rig are outlined. Safety precautions and emergency protocols are discussed. The document is also hung on the lab door for ease of reference.

Ben T. Zinn Combustion Lab 130: Standard Operating Procedures (SOP)

PURPOSE: This document outlines the several safety and operational procedures needed to utilize LabView 2019 with a cRIO, temperature and pressure sensors, and the supersonic rig.

SCOPE: Graduate Student Joshua Johnson and Georgia Tech Research Personnel seek to characterize the breakup characteristics of a water jet in a supersonic crossflow (JISCF), placed in an air tunnel. Optical techniques will measure the parameters of the water jet while the rig is running.

PERSONNEL RESPONSIBLE: Research Engineers and Graduate Student Joshua Johnson. The rig can be run alongside these personnel if and only if they have completed their safety review.

NORMAL PROCEDURES:

LabView Procedures

1. There is one NI-DAQ CompactRIO that needs to be connected to the computer to control the supersonic rig instruments. Locate the ethernet cable for the NI-DAQ CompactRIO and plug it into the computer. The cable is run through the firewall of the control room.
2. Flip the switch on the DAQ mounting box to turn it on.
3. Verify using the program "NI MAX" that the DAQ is seen on the local network under "Remote Systems"
   a. *SS-Mix-NI-cRIO9024-01717387* is the **Supersonic Mixing/JICF Rig**.
   b. In the windows command prompt, we can ping them to make sure communication is coming through 192.168.0.11 (mixing).
4. Open the respective folders to run the projects' FPGA as a check - "LabView JICF Rig".
5. Close the FPGA after running and open the main VI to display all parameters. Run these.

Preliminary Lab Check Procedures

1. Make sure to put on safety goggles and earplugs & headphones for the entirety of the experiment.
2. Check that the compressor is running. If not, press "START" on the control panel and "LOAD" after both low and high stages of the lubricant system are >0 PSI on the gauges.
   a. Make sure the oil level in the cylindrical tube by the lubricant pump is above the first two partition rings. If not, switch the oil fill control knob to "AUTO" and allow it to fill back up.
   b. Allow the compressor to reach 2,500 PSI.
   c. If you'd like to calculate how long it will take for the compressor to reach this pressure, contact jjohnson475@gatech.edu for the excel file for it.

3. Check all surrounding lab rooms to make sure the natural gas and air lines are in the closed position. (labs 133, 126, 127, 128, and the black hand valve outside 132).
4. Turn the physical switch in lab 127 to “remote”. In lab 132, use the tablet to switch to “local”.
5. Using the key above the sign-in sheet, unlock the air valve inside lab 130.
6. Make sure all items are secured in lab 130 and turn on the exhaust on the control panel near lab 119.
7. Put tape up on the two doors leading to lab 130 and alert other research personnel that the rig will be run.
8. Test the regulator downstream of the water filters by turning it on and off in the LabView environment & listening for activation noise.
9. Ensure all valves are open on the piping, allowing the water and nitrogen to flow.
10. Open the domestic water valve open and fill the water tank. Open the vent valve. Once the water drips out of the vent, the tank is full. Close the domestic water valve and use a wrench to disconnect the water pipe on the pre-filter. Run this water line all the way to the drain in the room and switch the hand valve to the “CLOSE” position. This is to depressurize the tank after running the rig. Switch the valve from vent to the nitrogen tanks. Open the valve at the bottom of the tank going to the filters and pressurize the tank using the nitrogen supply. Open both nitrogen tanks all the way up and use the pressure regulator to set the downstream low-pressure side to a desired PSI (max is 500PSI). Note, the burst plate is set at 700 PSI in case the regulator fails.
    a. Initially, you can test which direction the valve needs to be turned to vent by running a small nitrogen supply and observing the vent line.
    b. Ensure all valves are open in the water line! The pressurized water will stop at the solenoid valve until we manually turn it on and set a pressure to it within LabVIEW.
11. Open the instrument air line (125 PSI) that is used to power the pressure regulator’s actuator.

Running the Rig Procedures

1. Select AFOSR Supersonic Mixing project on one laptop and the Supersonic Mixing project on the other laptop at myRIO menu interface.
2. Right click on each RIO and connect.
3. Test FPGAs under the dropdowns to make sure raw data is being transmitted by sensors.
4. Ensure the tablet control panel is operational and displaying an accurate tank pressure.
    a. If this cannot be seen, log into the tablet by pressing “Login” -> [username] operator -> [password] (Talk to building manager for the password).
5. Press “ON” and “START” to open the valve to flow air into lab 130.
6. Set SP (air pressure control) to 10-20 PSI starting out.

7. Start air temperature blower by “POWER ON” -> “START” -> BURNER START” and ensuring the burner control panel successfully runs through all checks. If on “AUTO”, preheat the air and try to stay under 1300F. Use the hot gas indicator if using “AUTO”.
8. If using “SOAKING”, use the process air temp controller to modify the temperature.
9. Increment the air heat and pressure until the target stagnation conditions are met.
10. Target stagnation temperature and pressure is approximately 600K/620F and 54 PSI, so SP should be around 200 PSI on the tablet near steady state target conditions.
11. Inject the pressurized water stream into the test section by turning on the solenoid valve and setting a desired pressure within the LabView environment. Make sure to turn on the “MAIN” power switch within the environment as well. Switch them both off when you’re done injecting.
12. Decrement the air flow down to 10-20 PSI once again and decrease the temperature to zero on the burner.
13. Hit “AUTO SHUTDOWN” to allow the burner to completely shut down and “STOP” then “OFF” on the air control pressure system. Switch the tablet communication back to “Remote”.
14. Stop the LabVIEW VI and close the program to avoid corruption.
15. Close nitrogen tank valves and all water line valves. If desired, ensure the tank pressure is >175 PSI then open the hand valve connected to the water pipe at the bottom of the tank to depressurize and release the tank of all water. Go to the drain and control the flow of the pressurized water.
16. Depressurize the system by venting the tank nitrogen to atmosphere and ensure all visual gauges go to 0 PSI.
17. Turn off the exhaust and proceed with locking valves and returning the key.
18. Turn off both cRIOs by flipping the switch on the two mounting boxes.
19. If needing to flush entire pipeline of water (for example, if leaving for weeks), uncap the drain underneath the injection plate and cap the connector to the injection plate. Run <100 PSI of nitrogen into the entire system, making sure the water fill valve is closed. Allow all water from pipes to drain out into a bucket.

LIST OF MAXIMUM PRESSURES:

General

1) All tubing – 3500 PSI.
2) All connectors – 4500 PSI.

Nitrogen-pressurization system

3) Pressure regulator – 500 PSI.
4) Burst disk – 700 PSI.
5) Tank – 3000 PSI.

Water System

6) Pre-Filter – 90 PSI.
7) Green fill/drain hose – 175 PSI.
8) Black connecting tank rubber hose – 1500 PSI.
9) Post filters (3) – 3000 PSI.
10) Visual gauge 1 – 3000 PSI.
11) Air actuated pressure regulator – 600 PSI.
12) Visual gauge 2 – 1000 PSI.

EMERGENCY PROCEDURES:

During Preliminary Lab Check

- Wear proper PPE. You must be wearing long pants, closed toe shoes, ear plugs, and safety goggles in lab 130. All of these must be worn when the rig is running in the control room, 132, as well. Remember to place goggles and earplugs on when walking into the compressor room.
    - If compressor fails, press "EMERGENCY STOP" on its control panel.
- Make sure all objects are off the rig's frame. It will heat up and vibrate at high temperatures/pressures.
- Make sure exhaust is turned on!
- Nitrogen cannot be detected with the overhead tree lights. If you detect a large leak or start feeling lightheaded, leave the lab to outside and allow the tanks to completely drain.
- If a **yellow** overhead tree light, shut the burner off and leave lab 130. Find a lab manager for next steps. Allow the air tank to run down. If the **red** overhead light is detected, proceed in the same steps but leave the entire combustion lab.
- There are 3 gas detectors outside of lab 130, mounted on the wall. They report gas inside 130 in PPM. If a certain threshold is met, the tree inside will light yellow or red, so check the detector periodically to make sure they're at 0.

During Startup and Running the Rig

- Do NOT walk into the room when air pressure is of excess of 20PSI.
- If there is any problem within the combustion lab, hit "AUTO SHUTDOWN" on the combustion air blower control panel and leave the lab.
- Shut the water/air injection control off and solenoid off before switching the air off.
- If LabView is lost, turn the air pressure down below 20 PSI and reduce the burner. Go into the lab and restart the cRIOs. If this doesn't work, shut the experiment down and figure out the issue.

- If building power is lost, shut down the STAHL combustion air blower to 0F if it's still operating.
- If there is excessive noise from the rig, turn the air pressure down to 10-20 PSI. If noise still exists, DO NOT enter the room, and shut everything down. If it's a nitrogen bottle, let it deplete and vent to exhaust.

During Shutdown

- Do not allow the combustion burner to be at an elevated temperature when the air pressure is low without "SOAKING" button enabled.

Special Cases

- If an object flies off the rig/tank due to a pressure failure and hits a water source (sprinkler head/water line), evaluate the issue and salvage expensive equipment, like a camera, if possible. If there is standing water, do not enter as there is a shock potential.

CLOSING REMARKS:

If you have any questions about this guide, please contact Graduate Student Joshua Johnson at: jjohnson475@gatech.edu.

Revision Block

Revision	**Revision Personnel**	**Date**	**Modifications Made**
0	Joshua Johnson	12/22/2021	INITIAL REVISION
1	Joshua Johnson	1/25/2022	1) Created maximum pressure list. 2) Revised "Running the Rig Procedures" to include soaking and auto procedures. 3) Fixed some emergency procedures following safety review. 4) Changed target stagnation temperature from 620K to 600K/620F. 5) Added instrument air instructions.
2	Joshua Johnson	4/29/2023	1) Revised DAQ systems after moving all instruments to a single DAQ.

Effective Date:	Revision Date:	Laboratory Location:
12/22/2021	4/29/2023	BTZ Lab 130

REFERENCES

[1] Y. Kamotani and I. Greber, "Experiments on a turbulent jet in a cross flow," in *10th Aerospace Sciences Meeting*, vol. 10, 1972, pp. 1425–1429.

[2] F. Génin and S. Menon, "Dynamics of sonic jet injection into supersonic crossflow," *Journal of Turbulence*, vol. 11, 2010.

[3] Y. A. Cengel and M. A. Boles, "Thermodynamics: An engineering approach," in 9th ed. New York: McGraw-Hill Education, 2018, ch. 9.

[4] G. Choubey, D. Yuvarajan, W. Huang, A. Shafee, and K. Pandey, "Recent research progress on transverse injection technique for scramjet applications-a brief review," *International Journal of Hydrogen Energy*, vol. 45, no. 51, pp. 27 806–27 827, 2020.

[5] C. Liu, Z. Wang, M. Sun, H. Wang, P. Li, and J. Yu, "Characteristics of the hydrogen jet combustion through multiport injector arrays in a scramjet combustor," *International Journal of Hydrogen Energy*, vol. 43, no. 52, pp. 23 511–23 522, 2018.

[6] P. Manna, R. Behera, and D. Chakraborty, "Liquid-fueled strut-based scramjet combustor design: A computational fluid dynamics approach," *Journal of Propulsion and Power*, vol. 24, no. 2, pp. 274–281, 2008.

[7] D. Cecere, A. Ingenito, E. Giacomazzi, L. Romagnosi, and C. Bruno, "Hydrogen/air supersonic combustion for future hypersonic vehicles," *International Journal of Hydrogen Energy*, vol. 36, no. 18, pp. 11 969–11 984, 2011.

[8] M. Gruber, J. Donbar, T. Jackson, T. Mathur, D. Eklund, and F. Billig, "Performance of an aerodynamic ramp fuel injector in a scramjet combustor," in *36th AIAA/ASME/SAE/ASEE Joint Propulsion Conference and Exhibit*. 2012.

[9] T. Ukai, H. Zare-Behtash, E. Erdem, K. H. Lo, K. Kontis, and S. Obayashi, "Effectiveness of jet location on mixing characteristics inside a cavity in supersonic flow," *Experimental Thermal and Fluid Science*, vol. 52, pp. 59–67, 2014.

[10] D. E. Nestler, A. R. Sayday, and W. L. Auxer, "Heat transfer to steps and cavities in hypersonic turbulent flow," *AIAA Journal*, vol. 7, no. 7, pp. 1368–1370, 1969.

[11] T. Roos, A. Pudsey, M. Bricalli, and H. Ogawa, "Cavity enhanced jet interactions in a scramjet combustor," *Acta Astronautica*, vol. 157, pp. 162–179, 2019.

[12] A. Ben-Yakar and R. Hanson, "Experimental investigation of flame-holding capability of hydrogen transverse jet in supersonic cross-flow," *Symposium (International) on Combustion*, vol. 27, no. 2, pp. 2173–2180, 1998.

[13] M. Zhao, Y. Bian, Q. Li, and T. Ye, “Large eddy simulation of transverse single/double jet in supersonic crossflow,” *Aerospace Science and Technology*, vol. 89, pp. 31–45, 2019.

[14] D. E. Enriquez, “Numerical investigation of variable momentum flux and density ratios on confined jets in crossflow,” M.S. thesis, 2016.

[15] C. O. Iyogun, M. Birouk, and N. Popplewell, “Trajectory of water jet exposed to low subsonic cross-flow,” *Atomization and Sprays*, vol. 16, no. 8, pp. 963–980, 2006.

[16] B. J. Masuda and V. G. McDonell, “Penetration of a recessed distillate liquid jet into a crossflow at elevated pressure and temperature,” in *International Conferences on Liquid Atomization and Spray Systems*, 2016.

[17] S. No, “A review on empirical correlations for jet/spray trajectory of liquid jet in uniform cross flow,” *International Journal of Spray and Combustion Dynamics*, vol. 7, pp. 283–314, Dec. 2015.

[18] R. Ragucci, A. Bellofiore, and A. Cavaliere, “Trajectory and momentum coherence breakdown of a liquid jet in high-density air cross-flow,” *Atomization and Sprays*, vol. 17, no. 1, pp. 47–70, 2007.

[19] J. N. Stenzler, J. G. Lee, D. A. Santavicca, and W. Lee, “Penetration of liquid jets in a cross-flow,” *Atomization and Sprays*, vol. 16, no. 8, pp. 887–906, 2006.

[20] J. H. Kim, K. W. Ku, H. J. Youn, J. G. Hong, C. W. Lee, and K. Y. Chung, “Effect of orifice configuration on the penetration height in crossflow,” in *International Conference on Liquid Atomization and Spray Systems*, 2012.

[21] S.-Y. No, “A review on empirical correlations for jet/spray trajectory of liquid jet in uniform cross flow,” *International Journal of Spray and Combustion Dynamics*, vol. 7, no. 4, pp. 283–313, 2015.

[22] T. T. Lim, T. H. New, and S. C. Luo, “On the development of large-scale structures of a jet normal to a cross flow,” *Physics of Fluids*, vol. 13, no. 3, pp. 770–775, 2001.

[23] X. Li and M. C. Soteriou, “High fidelity simulation and analysis of liquid jet atomization in a gaseous crossflow at intermediate Weber numbers,” *Physics of Fluids*, vol. 28, 2016.

[24] J. C. Beale and R. D. Reitz, “Modeling spray atomization with the Kelvin-Helmholtz/Rayleigh-Taylor hybrid model,” *Atomization and Sprays*, vol. 9, no. 6, pp. 623–650, 1999.

[25] M. Broumand, M. Birouk, and S. V. Mahoodi J., "Liquid jet primary breakup in a turbulent cross-airflow at low Weber number," *Journal of Fluid Mechanics*, vol. 879, pp. 775–792, 2019.

[26] S. Ghods, "Detailed numerical simulation of liquid jet in crossflow atomization with high density ratios," Ph.D. dissertation, 2013.

[27] C. Medipati, S. Deivandren, and R. Govardhan, "Liquid jet injection in supersonic crossflow: Self-induced jet oscillations and its effects," *International Journal of Multiphase Flow*, vol. 158, p. 104 265, 2022.

[28] M. Pai, I. Bermejo-Moreno, O. Desjardins, and H. Pitsch, "Parametric study of primary breakup of turbulent liquid jets in crossflow: Role of Weber number," in *48th AIAA Aerospace Sciences Meeting Including the New Horizons Forum and Aerospace Exposition*, 2010.

[29] Y. Chen, E. DeMauro, J. L. Wagner, M. Arienti, D. R. Guildenbecher, P. Farias, T. W. Grasser, P. Sanderson, S. Albert, A. Turpin, W. Sealy, and R. S. Ketchum, "Aerodynamic breakup and secondary drop formation for a liquid metal column in a shock-induced cross-flow," in *55th AIAA Aerospace Sciences Meeting*, 2017.

[30] Y. Chen, J. L. Wagner, P. A. Farias, E. P. DeMauro, and D. R. Guildenbecher, "Galinstan liquid metal breakup and droplet formation in a shock-induced cross-flow," *International Journal of Multiphase Flow*, vol. 106, pp. 147–163, 2018.

[31] J. A. Johnson, S. Menon, and Y. C. Mazumdar, "Digital holography for investigating front-edge instabilities of liquid jets in supersonic crossflows," in *AIAA Aerospace Sciences Meeting, AIAA SciTech*, 2023.

[32] K. A. Sallam, C. Aalburg, G. M. Faeth, K.-C. Lin, C. D. Carter, and T. A. Jackson, "Primary breakup of round aerated-liquid jets in supersonic crossflows," *Atomization and Sprays*, vol. 16, pp. 657–672, 2006.

[33] J. Lee, K. A. Sallam, K. C. Lin, and C. D. Carter, "Spray structure in near-injector region of aerated jet in subsonic crossflow," *Journal of Propulsion and Power*, vol. 25, no. 2, pp. 258–266, 2009.

[34] D. S. Olinger, K. A. Sallam, K.-C. Lin, and C. D. Carter, "Digital holographic analysis of the near field of aerated-liquid jets in crossflow," *Journal of Propulsion and Power*, vol. 30, no. 6, pp. 1636–1645, 2014.

[35] K. A. Sallam, K. C. Lin, S. D. Hammack, and C. D. Carter, "Digital holographic analysis of the breakup of aerated liquid jets in supersonic crossflow," in *55th AIAA Aerospace Sciences Meeting*, 2017.

[36] M. B. Kuhn and O. Desjardins, "Experimentally validated high-fidelity simulations of a liquid jet in supersonic crossflow," *International Journal of Multiphase Flow*, vol. 156, p. 104 195, 2022.

[37] D. Fries, "Entrainment, mixing, and ignition in single and multiple jets in a supersonic crossflow," Ph.D. dissertation, 2020.

[38] Y. Yang and B. Kang, "Digital particle holographic system for measurements of spray field characteristics," *AIAA Journal*, vol. 49, no. 11, pp. 1254–1263, 2011.

[39] J. Mazallon, Z. Dai, and G. Faeth, "Aerodynamic primary breakup at the surface of nonturbulent round liquid jets in crossflow," in *36th AIAA Aerospace Sciences Meeting*, 1998.

[40] R. S. Prakash, A. Sinha, G. Tomar, and R. Ravikrishna, "Liquid jet in crossflow - effect of liquid entry conditions," *Experimental Thermal and Fluid Science*, vol. 93, pp. 45–56, 2015.

[41] G. S. Settles and M. J. Hargather, "A review of recent developments in schlieren and shadowgraph techniques," *Measurement Science and Technology*, vol. 28, 2017.

[42] M. J. Hargather and G. S. Settles, "A comparison of three quantitative schlieren techniques," *Optics and Lasers in Engineering*, vol. 50, no. 1, pp. 8–17, 2012.

[43] G. Speak and D. Walters, "Optical considerations and limitations of the schlieren method," *Aeronautical Research Council Reports and Memoranda*, 1950.

[44] Y. Huang, H. Du, W. Wang, D. Shi, Y. Wu, B. Li, and L. Zhou, "OH-planar laser-induced fluorescence measurements in laminar diffusion flames of n-heptane with coflow air diluted by N2 and CO2," *ACS Omega*, vol. 6, pp. 24 515–24 525, 2021.

[45] M. Gamba, V. A. Miller, and G. Mungal, "The reacting transverse jet in supersonic crossflow: Physics and properties," in *19th AIAA International Space Planes and Hypersonic Systems and Technologies Conference*, 2014.

[46] R. Fearn and R. P. Weston, "Vorticity associated with a jet in a cross flow," *AIAA Journal*, vol. 12, pp. 1666–1671, 1974.

[47] J. Zhao, Y. Tong, Y. Ren, Y. Zhu, Z. Chen, W. Lin, and W. Nie, "Structures of liquid jets in supersonic crossflows in a rectangular channel with an expansion section," *Physics of Fluids*, vol. 32, pp. 111704-1–111704-6, 2020.

[48] R. Portz and C. Segal, "Penetration of gaseous jets in supersonic flows," *AIAA Journal*, vol. 44, pp. 2426–2429, 2006.

[49] Z. Li, X. Yu, G. Lequien, T. Lind, M. Jansons, O. Andersson, and M. Richter, "Comparison of the lift-off lengths obtained by simultaneous OH-LIF and OH* chemiluminescence imaging in an optical heavy-duty diesel engine," in *SAE Technical Paper Series*, 2015, pp. 2015-24–2418.

[50] E. Luthman, N. Cymbalist, D. Lang, G. Candler, and P. Dimotakis, "Simulating schlieren and shadowgraph images from LES data," *Experiments in Fluids*, vol. 60, no. 134, pp. 1–16, 2019.

[51] M. Tanahashi, S. Murakami, G. Choi, Y. Fukuchi, and T. Miyauchi, "Simultaneous CH–OH PLIF and stereoscopic PIV measurements of turbulent premixed flames," *Proceedings of the Combustion Institute*, vol. 30, no. 1, pp. 1665–1672, 2005.

[52] A. W. Marsh, A. Zheng, J. Heyborne, D. R. Guildenbecher, and Y. C. Mazumdar, "Solid propellant scaling analysis using simultaneous holography and imaging pyrometry," in *AIAA Scitech 2021 Forum*, 2021.

[53] J. Katz and J. Sheng, "Applications of holography in fluid mechanics and particle dynamics," *Annual Review of Fluid Mechanics*, vol. 42, pp. 531–555, 2010.

[54] J. Sheng, E. Malkiel, and J. Katz, "Digital holographic microscope for measuring three-dimensional particle distributions and motions," *Applied Optics*, vol. 45, pp. 3893–3901, 2006.

[55] D. R. Guildenbecher, M. A. Cooper, and P. E. Sojka, "High-speed (20 kHz) digital in-line holography for transient particle tracking and sizing in multiphase flows," *Applied Optics*, vol. 55, no. 11, pp. 2892–2903, 2016.

[56] Y. Chen, D. R. Guildenbecher, K. N. G. Hoffmeister, M. A. Cooper, H. L. Stauffacher, M. S. Oliver, and E. B. Washburn, "Study of aluminum particle combustion in solid propellant plumes using digital in-line holography and imaging pyrometry," *Combustion and Flame*, vol. 182C, pp. 225–237, 2017.

[57] Y. Chen and D. R. Guildenbecher, "Quantitative, bias-corrected measurements of droplet position, size and velocity with digital in-line holography," in *ILASS Americas 29th Annual Conference on Liquid Atomization and Spray Systems*, 2017.

[58] A. W. Marsh, G. T. Wang, J. D. Heyborne, D. R. Guildenbecher, and Y. C. Mazumdar, "Time-resolved size, velocity, and temperature statistics of aluminum combustion in solid rocket propellants," *Proceedings of the Combustion Institute*, vol. 38, no. 3, pp. 4417–4424, 2021.

[59] A. W. Marsh, T. M. Evans, B. Musci, J. Uzodima, S. P. Kearney, D. R. Guildenbecher, and Y. C. Mazumdar, "Phase distortion cancellation using recalculated in-

tensity propagation phase holography," *Optics and Lasers in Engineering*, vol. 146, p. 106 706, 2021.

[60] U. Schnars, C. Falldorf, J. Watson, and W. Jüptner, "Digital holography," in *Digital Holography and Wavefront Sensing: Principles, Techniques and Applications*. Berlin, Heidelberg: Springer Berlin Heidelberg, 2015, pp. 39–68.

[61] D. R. Guildenbecher, K. N. G. Hoffmeister, W. M. Kunzler, D. R. Richardson, and S. P. Kearney, "Phase conjugate digital inline holography (PCDIH)," *Optics Letters*, vol. 43, no. 4, pp. 803–806, 2018.

[62] Y. C. Mazumdar, M. E. Smyser, J. D. Heyborne, M. N. Slipchenko, and D. R. Guildenbecher, "Megahertz-rate shock-wave distortion cancellation via phase conjugate digital in-line holography," *Nature Communications*, vol. 11, p. 1129, 2020.

[63] A. W. Marsh, Z. D'Ambra, A. Mcmaster, D. R. Guildenbecher, and Y. C. Mazumdar, "Analysis of holography techniques for phase distortion removal in extreme environments," in *61st AIAA Aerospace Sciences Meeting*, 2023.

[64] W. D. Bachalo and M. J. Houser, "Spray drop size and velocity measurements using the phase/doppler particle analyzer," *International Journal of Turbo and Jet Engines*, vol. 4, no. 3-4, pp. 207–216, 1987.

[65] S. V. Sankar and W. Bachalo, "Response characteristics of the phase doppler particle analyzer for sizing spherical particles larger than the light wavelength.," *Applied optics*, vol. 30 12, pp. 1487–96, 1991.

[66] A. Pizzaia and T. Rossmann, "Effect of boundary layer thickness on transverse sonic jet mixing in a supersonic turbulent crossflow," *Physics of Fluids*, vol. 30, no. 11, p. 115 104, 2018.

[67] K.-C. Lin, P. Kennedy, and T. Jackson, "Structures of water jets in a Mach 1.94 supersonic crossflow," in *42nd AIAA Aerospace Sciences Meeting and Exhibit*. 2012.

[68] D. R. Guildenbecher, J. Gao, P. L. Reu, and J. Chen, "Digital holography simulations and experiments to quantify the accuracy of 3D particle location and 2D sizing using a proposed hybrid method," *Applied Optics*, vol. 52, no. 16, pp. 3790–3801, 2013.

VITA

Joshua Johnson was born on July 15, 1999, in Atlanta, Georgia. Growing up, he has always had the desire to learn more about how natural phenomenon occurs around him. How does an engine work? What are the processes behind converting mechanical work to usable energy? How does this gear fit here? His dedication to the pursuit of knowledge has allowed him to collaborate with brilliant minds around the world while contributing to research in the niche field - liquid jets in supersonic crossflows. Joshua is looking forward to making further advances within the realm of combustion engines, especially as decarbonization efforts are underway.

”Good job buddy!” - My Father.